

The Effectiveness of Mitigation Methods in Reducing Structure-Borne Underwater Radiated Machinery Noise from Ships

T.R. Speelman

The Effectiveness of Mitigation Methods in Reducing Structure-Borne Underwater Radiated Machinery Noise from Ships

by

T.R. Speelman

A thesis presented to obtain the degree of
Master of Science
in Civil Engineering at the Delft University of Technology

This thesis is confidential and cannot be made public until June 1, 2024.

Student number:	4448332
Project duration:	September, 2021 – June, 2022
Thesis committee:	Dr. ir. A. Tsouvalas, TU Delft, chair
	Dr. ir. H.O. Sertlek, TU Delft, supervisor
	Dr. ir. K.N. van Dalen, TU Delft, supervisor
	ir. A. Tsetas, TU Delft, supervisor
	ir. P.T. Nobel, Nevesbu, company supervisor

Cover picture by Jim Beaudoin, 2018

Nomenclature

dB re $1 \mu\text{Pa}^2\text{m}^2$	Decibel relative to 1 micropascal at 1 meter from the source
BEM	Boundary Element Method
DAF	Dynamic Amplification Factor
DOF	Degree of Freedom
EB	Equivalent Beam
EOM	Equation of Motion
EPW	Elements Per Wavelength
FEA	Finite Element Analysis
FEM	Finite Element Method
FSI	Fluid Structure Interaction
mck	mass-spring-damper
Noise	Undesired pressure fluctuations around the mean pressure of the medium
PML	Perfectly Matched Layers
SDOF	Single Degree of Freedom
Sound	Pressure fluctuations around the mean pressure of the medium
TMD	Tuned Mass Damper
URN	Underwater Radiated Noise

Preface

Before you lies my master thesis which is the product of nine months of hard work and seven years of studying. The past seven years were excellent in all areas. I absorbed a tremendous amount of knowledge and developed a valuable way of thinking. But besides studying, I had a lot of great experiences that are the foundation for my development as a person to someone I am proud of today and the rest of my life.

The past nine months have naturally gone hand-in-hand with ups and downs. As an inexperienced person, wandering alone down the path of uncertainty makes you question from time to time whether or not you are doing the right thing. Luckily, there were people involved with my thesis either because they had to, wanted to or because I made them to.

I would like to thank Pieter for all his time, effort and the valuable conversations we had during my thesis. Every time when I was in doubt or stuck in tunnel vision, he would make sure to provide different insights. Furthermore, Pieter and Nevesbu provided me with the opportunity and resources to graduate on this most interesting topic, for which I am grateful.

Moreover, I would like to express my gratitude towards my TU Delft supervisors Apostolos, Thanasis and Özkan for their great guidance and feedback during all the meetings.

Lastly, I would like to thank my family, friends and girlfriend for their constant support and understanding throughout the past year. Even though not everybody had a clue of what I was talking about, they still offered a listening ear and sometimes even interesting insights.

I wholeheartedly hope that this thesis will be of interest to the reader and contributes to the advancement of technology and the improvement of living conditions on this earth for all beings.

*T.R. Speelman
Delft, June 2022*

Summary

In the underwater environment, it is all but silent. In most parts of the oceans, sunlight is barely available and thus marine animals have evolved to rely on sound for navigation, foraging and communication. Marine animals are not the only sources of underwater sound. Other natural sources such as earthquakes, waves and rain cause ambient noise, but also loud impulses. Furthermore, human activities consisting of dredging, surveying, construction and shipping cause loud noise in a wide frequency range. Underwater radiated noise (URN) from shipping has severe negative consequences on marine animals. The negative effects include auditory masking, stress, and behavioural and acoustic responses, possibly leading to collision with ships. It is evident that the mitigation of the underwater radiated noise of a ship is advantageous and worth researching.

In the past, plenty of research has been done into the modelling of the acoustic characteristics of vessels. A research gap was identified in the modelling of mitigation methods of the underwater radiated noise from ships with a focus on marine mammals. Up until now, most research has focused on the attenuation of vibrations on board a ship or radiated noise due to the propellers. At all times, the focus was either on human comfort or the radiated noise in general, however, for marine mammals certain frequency bands are of greater importance. It is valuable to assess the URN of a ship in the design phase, such that adjustments can be made to decrease the URN without excessive costs. The research goal of this thesis is:

Predict and mitigate the structure-borne underwater radiated noise of a ship in the design phase caused by onboard machinery.

The research goal and corresponding research questions are answered by first setting up the framework for the models. This framework sets the frequency analysis range to 20 – 200 Hz, formulates a reference ship case for validation of the data and gives the inputs and boundary conditions for the models. The acoustic metric of interest is set to the source level (SL) in dB re $1 \mu\text{Pa}^2\text{m}^2$.

Secondly, a simplified model is setup in Ansys 2021R2. This model is a 3D solid element model shaped like a beam. The equivalent beam (EB) model has similar global properties as the reference ship case. Around the EB model an acoustic domain is located that is modelled to represent an infinite domain. No physical boundary effects are included as the source level is per definition not dependent on this.

Subsequently, mitigation methods for machinery URN are researched and the resilient mount was found to be the most promising. A resilient mount is applied to the EB model in Ansys 2021R2 and source level spectra for different mount parameters are investigated.

Lastly, a two degree of freedom (2-DOF) schematisation is made that incorporates the Ansys model using a dynamic stiffness. The 2-DOF schematisation allows for faster computations of the complete model and thus a more extensive parameter study of the resilient mount is possible.

Over the frequency analysis range of 20 – 200 Hz, the results show that machinery structure-borne URN can be reduced by 45 – 65 dB re $1 \mu\text{Pa}^2\text{m}^2$. The reduction oscillates over the frequencies at lower frequencies. A linear SL reduction was observed from 60 Hz and above, which gradually lessened for higher frequencies. The SL reduction increased from 45 dB re $1 \mu\text{Pa}^2\text{m}^2$ to 60 dB re $1 \mu\text{Pa}^2\text{m}^2$ when the resilient mount damping ratio was changed from 0.18 to 0.02. In addition, the normalised resilient mount parameter study showed the system's parameter sensitivities and responses. It became clear that the resilient mount does not respond to a change in resilient mount damping as expected. The accuracy of the absolute results is subject to assumptions and limitations, which introduce uncertainties.

The absolute decrease in URN with the resilient mount was computed using acceleration input rather than force input. The acceleration input was found to have overestimated the 'no-mount' case, which was used to compare cases with the resilient mount. The total URN reduction with the resilient mount could thus have been overestimated. Furthermore, an effect of the model boundaries and the model domain size on the results was present in the models. The magnitudes of the results were influenced by this effect, which could not be eliminated due to the computational limitations reached. Finally, there was a scarcity of model input

data and reference data. The magnitudes of the results were obtained and compared to limited data in order to determine the accuracy of the results.

Taking these limitations into consideration, the findings of this study should be interpreted with caution. The findings support literature claims that a resilient mount can reduce structure-borne machinery URN by 20 – 40 dB re $1 \mu\text{Pa}^2\text{m}^2$, with more reduction at higher frequencies.

The effect of the application of the resilient mount on marine mammals was hard to quantify. The structure-borne machinery URN is a part of the total URN of a ship. Due to the logarithmic relation of the noise, the reduction of one part could have very limited effects. Furthermore, the total soundscape in the ocean is formed by the combined noise of many ships. Moreover, the relation between the perceived nuisance of marine mammals and the URN levels is hard to indicate. The effect is undoubtedly positive but could be negligible in the bigger picture. At low speeds and close distances, the machinery URN is governing and the influence of URN from other ships is reduced. In those cases, the reduction of structure-borne machinery URN with resilient mounts could be expected to be the most positive for marine mammals.

Contents

1	Introduction	1
1.1	Problem Description	1
1.2	Current state of Research	2
1.3	Research Objective, Questions, Scope and Scale	4
1.4	Report Outline	5
2	Literature Study	6
2.1	Marine Life	6
2.2	Anthropogenic Sources of Sound and Ship Noise	7
2.2.1	The Ship as a Source of Underwater Noise	8
2.3	Noise Mitigation Methods.	9
2.3.1	Resilient Mount	11
2.3.2	Physics of the Resilient Mount	12
2.4	Modelling Techniques for Underwater Radiated Noise	13
2.4.1	Finite Element Analysis (FEA)	13
2.4.2	Boundary Element Method (BEM)	15
2.5	Structural Acoustics.	16
2.6	Fluid acoustics	18
2.7	Fluid-Structure Coupling	19
3	Methodology	20
3.1	Simplification Options	20
3.2	Framework for the Simplified Model	23
3.2.1	Reference Case and Validation Data	23
3.2.2	Analysis Frequency Range	26
3.2.3	Type of Machinery and Input Spectra	26
3.2.4	Operating Conditions	27
3.2.5	Boundary Conditions	28
3.2.6	Acoustic Metric	28
3.3	Equivalent Beam Model.	29
3.3.1	Model Shape and Dimensions	29
3.3.2	Materials and Properties	29
3.3.3	Equivalent Beam Dynamics Behaviour Check/Range of Applicability	31
3.3.4	Fluid Domain	32
3.3.5	Boundary Conditions and Model Inputs	34
3.3.6	Mesh and elements	35
3.4	Resilient Mount Application in EB Model	37
3.4.1	Schematisation of the Resilient Mount.	37
3.4.2	Mathematical Formulation and Parameter Influence	37
3.4.3	Parameter Tuning	38
3.4.4	FEM Modelling.	39
3.5	2-DOF Mount Schematisation	41
3.6	Solving and Data Processing	42
3.6.1	Solution Strategies	42
3.6.2	Capturing the Results and Spatial Averaging	42
3.7	Assumption Overview.	44
4	Results	45
4.1	Equivalent Beam	45
4.1.1	Far-Field Acoustic Pressure	45
4.1.2	Source Levels	48

4.2	Resilient Mount Application	49
4.2.1	Source Levels	49
4.2.2	2-DOF Schematisation	50
4.2.3	Parameter Study	51
5	Discussion	54
5.1	Model Input.	54
5.1.1	Spectrum Interpolation	54
5.1.2	Acceleration Versus Force Input	55
5.2	Sinusoidal Pattern in Frequency Domain	57
5.2.1	PML Layer Influence	57
5.2.2	Domain Size	58
5.3	Reference Data Comparison	58
5.4	Resilient Mount Modelling	60
5.5	Assumption Interpretation and Model Limitations	63
5.6	Computational Limits.	64
5.6.1	Mesh Size	65
5.6.2	Domain Size	65
5.6.3	Frequency Analysis Range and Frequency Resolution	65
5.7	Result Interpretation, Scientific Impact and Practical Applications	65
6	Conclusion and Recommendations	67
	References	70
A	Damping Formulation of Ansys	74
B	Resilient Mount Ansys Settings	75
C	Perfectly Matched Layers Discussion	76
D	Resilient Mount Parameter Study Additional Graphs	77
D.1	Normalised Source Level Graphs	77
D.2	Pressure Graphs.	78
D.3	2-DOF Surface and Contour Plots Alternative Colours	81
D.4	Surface and Contour Plots Normalised \tilde{U}_1	82
E	Transmissibility Intersection Point for a 2-DOF System	83

List of Figures

1.1	The Levels and Frequencies of Different Natural and Anthropogenic Underwater Noise Sources. (OSPAR, n.d.)	1
1.2	The Acoustic Absorption as a Function of the Frequency. (Hovem, 2013)	2
1.3	Flowchart of the Research and Report.	5
2.1	Examples of Marine Mammals.	6
2.2	Source Level Noise of the M/V Overseas Harriete and RANDI (Research Ambient Noise Directionality) Model Ships. (M. Ainslie, de Jong, Dol, Blacqui�re, & Marasini, 2009)	10
2.3	Most Common Sources of Noise on a Ship. (Abrahamsen, 2012)	10
2.4	A Schematic Example of a Resilient Mounting System Applied to the Machinery of a Ship.	11
2.5	The Dynamic Response of a Mass-Spring-Damper System.	12
2.6	Flowchart Visualising the Process for a FEA.	14
2.7	Different Element Types Used in FEM. (A�ıkg�z, 2019)	15
2.8	A Typical Example of a Sparse Matrix for a FEA. (Alexandrov, 2007)	15
2.9	The Domain and Discretization for an External 2D-Problem.	16
2.10	The Process of Acoustics in a Structure. (Cremer, Heckl, & Petersson, 2005)	16
2.11	Different Types of Waves in Structures. Displacements are Exaggerated. (Hambric, 2006)	17
2.12	Characteristics of Waves. (Hansen, 2001)	17
3.1	The First Four Mode Shapes of a Simply Supported Beam.	21
3.2	The Spectra for Source Levels for 3 RANDI Classes and the OH for Different Speeds. (M. Ainslie et al., 2009)	23
3.3	The Spectra for Source Levels for the 5 RANDI Classes and the Wales & Heitmeyer model. (M. Ainslie et al., 2009)	23
3.4	The Spectra of the W&H Model and Measurements of Ship Classes Close to the Port of Rotterdam. (Jansen & de Jong, 2017)	24
3.5	Decomposed Source Level Noise Spectrum for a Generic Merchant Ship at 15 knots. (Audoly et al., 2017)	24
3.6	Simulated URN of the Merchant/Tanker Class Ship Analysed by Zhang, Xiang, He, and Zhang (2019).	24
3.7	Mean Residual Errors of the Randi and W&H Models Compared to Recent Data From 2017. (MacGillivray & de Jong, 2021)	25
3.8	Comparison of the Mean Source Level Spectra of the ECHO Data Set, RANDI and W&H Models, and the New Model Created by MacGillivray and de Jong (2021).	25
3.10	The Giant 5 Barge Owned by Boskalis.	29
3.11	FEM Model of the Giant 5 Barge from Boskalis provided by Nevesbu Modelled as a Simply Supported Beam (TOP). Results of the Simply Supported Beam Static Analysis (BOTTOM).	30
3.12	Deflection of a Simply Supported Beam Subjected to a Point Load.	30
3.13	Half-Space Model Used for the FEM Simulations. Grey: EB, Blue: Acoustic Domain, Green: Buffer Layer, Red: PML region.	32
3.14	Dimensions of the Fluid Domain.	33
3.15	Boundary Conditions Imposed on the EB Model.	35
3.16	Acoustic Fluid and Structural Element Size Requirement Versus Frequency.	36
3.17	Mesh of the EB Model.	36
3.18	Schematisation of Resilient Mount System Applied to the Machinery of the EB Model.	37
3.19	Close Up of the Machinery Block and Mount Geometry.	40
3.20	Modelling of the Machinery Block, the Mount and the Input.	40
3.21	Unit Acceleration Amplitude and Corresponding Absolute Displacement Amplitude as a Function of Frequency.	40

3.22 2-DOF Schematisation	41
3.23 Schematic Showing the Generation of Interfering Waves	42
3.24 Model Dimension and Directions Within the Acoustic Domain [Not to Scale].	43
4.1 Acoustic Waves in the Equivalent Beam Model at 192 Hz.	45
4.2 Displacements of the Equivalent Beam Model at 192 Hz.	46
4.3 Directional Far-Field Acoustic Pressure Pattern Due to Unity Load.	46
4.4 Directional Far-Field Acoustic Pressure Pattern Due to Machinery Force Spectrum.	46
4.5 Far-Field Acoustic Pressure Spectrum for the Equivalent Beam Model With a Unity Load at 1000 m.	47
4.6 Far-Field Acoustic Pressure Spectrum for the Equivalent Beam Model With the Machinery Load at 1000 m.	47
4.7 Source Level Spectrum for the Equivalent Beam Model With a Unity Load.	48
4.8 Source Level Spectrum for the Equivalent Beam Model With the Machinery Load.	48
4.9 Directional Source Level Pattern Due to Unity Load	49
4.10 Directional Source Level Pattern Due to Machinery Force Spectrum	49
4.11 Source Level Spectrum for Different Damping Ratios.	50
4.12 Source Level Reduction for Different Damping Ratios.	50
4.13 Source Level Spectrum for Different Stiffness Values.	50
4.14 Source Level Reduction for Different Stiffness Values.	50
4.15 Directional Source Level Pattern at 192 Hz for Different Damping Ratios.	51
4.16 Directional Source Level Pattern at 192 Hz for Different Stiffness Values.	51
4.17 Displacement \tilde{U}_2 (a and b) and Source Level (c and d) Normalised to the Response with the Resilient Mount Base Settings.	52
4.18 Surface Plots of Displacement \tilde{U}_2 at 192 Hz for Combinations of stiffness Values and Damping Ratios Normalised to the Response with the Resilient Mount Base Settings.	52
4.19 Contour Plots of Displacement \tilde{U}_2 at 192 Hz for Combinations of stiffness Values and Damping Ratios Normalised to the Response with the Resilient Mount Base Settings.	53
5.1 Original Input Spectrum Versus the Interpolated Input Spectrum for the EB Model.	55
5.2 Original Input Spectrum Versus the Interpolated Input Spectrum for the Resilient Mount Application.	55
5.3 Source Level Spectra for Acceleration Input and Force Input.	56
5.4 Source Level Spectra for Acceleration Input and Force Input Normalised to the Spectrum for Force Input.	56
5.5 Energy Flux on the First PML layer for Different Frequencies.	57
5.6 Raw Model Output to Unit Input Force for a Small Model (40 m) and a Large Model (80 m) at 180 Degrees.	58
5.7 EB model Source Level Results and Results From Zhang et al. (2019) Comparison.	59
5.8 Speed Dependence of Source Level Versus Ship Type. Comparison Between RANDI and W&H Models and Echo Data Set. (MacGillivray & de Jong, 2021)	59
5.9 The Averaged Source Level Spectrum of the EB Model Plotted with the Expected Magnitude Range.	60
5.10 The ratio between \tilde{U}_1 and \tilde{U}_2 of the 2-DOF Schematisation over the Frequency Analysis Range.	61
5.11 Transmissibility Curve of an SDOF System.	62
5.12 Transmissibility of the 2-DOF Schematisation for Different Mount Stiffness Values.	62
5.13 Displacement \tilde{U}_2 for Different Damping Values and a Resilient Mount Stiffness of $k_1 = 80 \cdot 10^7$ N/m Normalised to the Response with the Resilient Mount Base Damping Ratio.	63
B.1 Modelling Settings of the Resilient Mount Connection Element Within Ansys Mechanical.	75
C.1 Far-Field Acoustic Pressures for an Increased Amount of PML Layers.	76
D.1 Directional Source Level Pattern at 192 Hz for Different Damping Ratios Normalised to the Response with the Resilient Mount Base Settings.	77
D.2 Directional Source Level Pattern at 192 Hz for Different Stiffness Values Normalised to the Response with the Resilient Mount Base Settings.	77

D.3	Pressure Spectrum for Different Damping Ratios.	78
D.4	Pressure Spectrum for Different Stiffness Values.	78
D.5	Pressure Spectrum for Different Damping Ratios Normalised to the Response with the Resilient Mount Base Settings.	79
D.6	Pressure Spectrum for Different Stiffness Values Normalised to the Response with the Resilient Mount Base Settings.	79
D.7	Directional Pressure Pattern at 192 Hz for Different Damping Ratios.	80
D.8	Directional Pressure Pattern at 192 Hz for Different Stiffness Values.	80
D.9	Directional Pressure Pattern at 192 Hz for Different Damping Ratios Normalised to the Response with the Resilient Mount Base Settings.	80
D.10	Directional Pressure Pattern at 192 Hz for Different Stiffness Values Normalised to the Response with the Resilient Mount Base Settings.	80
D.11	Surface Plots of Displacement \tilde{U}_2 at 192 Hz for Combinations of stiffness Values and Damping Ratios Normalised to the Response with the Resilient Mount Base Settings.	81
D.12	Contour Plots of Displacement \tilde{U}_2 at 192 Hz for Combinations of stiffness Values and Damping Ratios Normalised to the Response with the Resilient Mount Base Settings.	81
D.13	Surface Plots of Displacement \tilde{U}_1 at 192 Hz for Combinations of stiffness Values and Damping Ratios Normalised to the Response with the Resilient Mount Base Settings.	82
D.14	Contour Plots of Displacement \tilde{U}_1 at 192 Hz for Combinations of stiffness Values and Damping Ratios Normalised to the Response with the Resilient Mount Base Settings.	82
E.1	Intersection Point for the Transmissibility of a 2-DOF System for Different Values of μ and β . . .	83

List of Tables

1.1	Different Sources, Paths and Receivers in the Acoustics of a Ship	4
2.1	Frequencies Used in Communication and Echolocation by a Selection of Marine Mammals. (National Research Council, 2000)	8
2.2	Estimation of the Total Acoustic Energy for the Largest Anthropogenic Sources. (M. Ainslie et al., 2009)	9
3.1	Weighted Trade-Off Table for Method of Simplification.	22
3.2	The Combination of Two Sound Signals of Different Decibel Levels, Including the Reduction of One Signal.	26
3.3	Machinery Specifications. (Daihatsu Diesel, 2021; Zhang et al., 2019)	27
3.4	Dimension of the Giant 5 Barge.	29
3.5	Comparison of Modes and Eigenfrequencies of the Giant 5 Barge and the Equivalent Beam.	31
3.6	Requirements for the Different Layers Within the Infinite Acoustic Fluid Domain. (Howard & Cazzolato, 2015)	34
3.7	Resilient Mount Run Parameters.	39
4.1	Ansys Results and 2-DOF schematisation Results Comparison at 192 Hz.	51

Introduction

1.1. Problem Description

In the underwater environment, it is all but silent. Sound travels over large distances in seawater and with a speed of up to five times greater when compared to sound travelling in air. In most parts of the oceans, sunlight is barely available and thus marine animals have evolved to rely on sound for navigation, foraging and communication. (Heenehan et al., 2019)

Marine animals are not the only sources of underwater sound. Other natural sources such as earthquakes, waves and rain cause ambient noise, but also loud impulses. Furthermore, human activities consisting of dredging, surveying, construction and shipping cause loud noise in a wide frequency range. Figure 1.1 gives an overview of the most important underwater noise sources, including their frequency band and noise level.

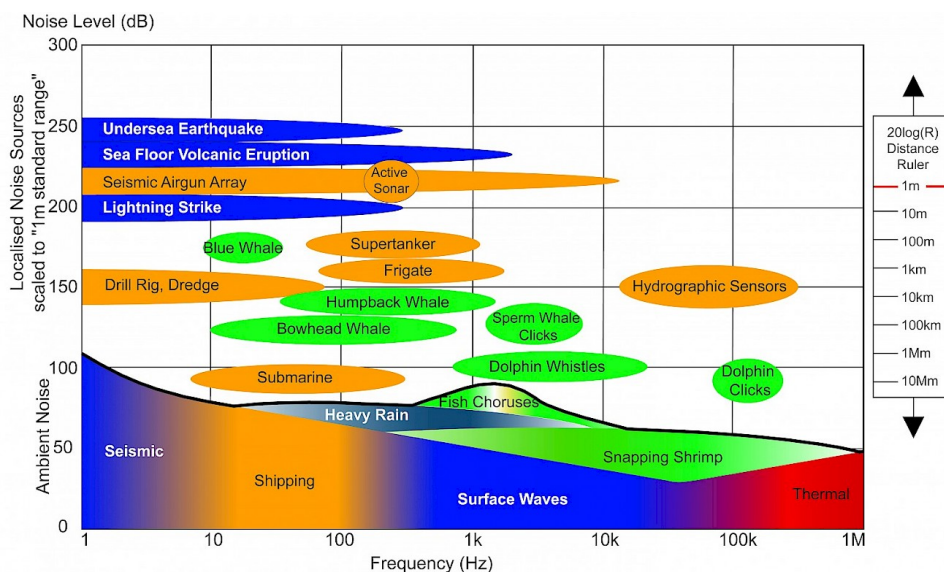


Figure 1.1: The Levels and Frequencies of Different Natural and Anthropogenic Underwater Noise Sources. (OSPAR, n.d.)

The shipping industry has the largest contribution to the anthropogenic underwater noise. Ship underwater noise is emitted due to cavitation at the propellers and due to machinery onboard the ships. Cavitation can account for up to 80-85% of the total noise emitted from a ship (ClearSeas, 2020). This is, however, dependent on the speed of the ship. At lower speeds, the noise caused by the engine starts to play a bigger role. Different types of boats produce different types of noise. The total noise volume from a large vessel can be up to 190 dB in the frequency range of 10 – 50 Hz, whilst the noise from a small boat has a maximum volume of 160 dB at the peak frequency of 5 kHz. Noise thus exists in many frequency bands and volume levels. (Hildebrand, 2009)

Low-frequency noise is attenuated slower than high-frequency noise as can be seen in Figure 1.2. Because of this, in the seas there is low-frequency ambient noise on the background present as is also seen in Figure 1.1.

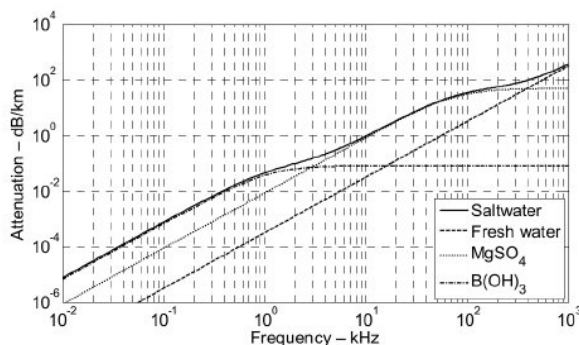


Figure 1.2: The Acoustic Absorption as a Function of the Frequency. (Hovem, 2013)

Underwater radiated noise (URN) from various human-made sources has severe long-term and short-term negative consequences for marine life, especially fish and marine mammals (The International Maritime Organisation, 2014). According to Erbe et al. (2019) the negative effects that have been observed include but are not limited to auditory masking, stress, and behavioural and acoustic responses. Large whale species adjust their volume and shift frequencies in response to excessive background noise from shipping and other sources (Pirotta, Grech, Jonsen, Laurance, & Harcourt, 2019). These behavioural changes could lead to an increase in collisions with ships, however, hard evidence for this is not yet available.

In 2017, the Port of Vancouver added a new criterion to their EcoAction program that offers discounts on port fees for quieter ships. In 2017 the Port of Vancouver's EcoAction program including the mitigation of underwater noise was the only one in the world. It is unclear whether at the time of writing more ports followed this development. (Strietman, Michels, & Leemans, 2018)

It is evident that the mitigation of the underwater radiated noise of a ship is advantageous and worth researching. The effects of certain mitigation methods on the underwater radiated noise should be quantifiable. It allows to adjust the design and evaluate the resulting acoustic footprint to achieve a ship design that meets specific acoustic requirements. In this manner, a design could be achieved that is more marine life friendly. The emphasis is on the design phase because it is generally the easiest and least expensive phase to make fundamental changes to the ship.

1.2. Current state of Research

In the past, plenty of research has been done into the modelling of the acoustic characteristics of vessels. Papers include both onboard and radiated noise, the propellers and machinery as noise sources, and structure-borne and air-borne propagation paths. It has been generally concluded that the statistical energy method (SEA) shows good results for modelling the acoustics in the high-frequency domain and the finite element method (FEM) shows good results for modelling in the low and medium frequency domain (Köykkä, 2016). In the following paragraphs, the latest research is shown to map the current status in the research field.

Köykkä (2016) did an elaborate literature study and concluded that FEM is an accurate way of modelling the acoustics in the low-frequency domain. For the high-frequency domain, the SEA showed good results. The modelling techniques were tested against a scale model experiment setup.

In a paper written by Herve, Wen, Wu, Amuaku, and Li (2018) a RORO-ship's onboard vibration due to the propellers was analysed using the SEA. Various mitigation methods such as cabin isolation and engine isolation were tested and showed a reduction of 3dB – 12dB. Model data was not verified with measurements.

Yanhe, Xuhong, Chengshun, and Zhigang (2019) did similar research, however, here a hospital ship was analysed and using the FEM. Attenuation of the acoustic vibrations induced by the propeller by means of insulating the ship around the propeller was analysed and good results were shown. The model results were

not validated against measurements.

Zhang et al. (2019) modelled the far-field underwater radiated noise due to onboard machinery. Three conventional modelling techniques are compared and the best modelling technique showed accurate results for its applicable frequency domain. FE-BEM was concluded to be the most accurate and the fastest for the low frequencies (20 – 200 Hz). The models were verified with measurements of a reference ship.

Auf (2020) performed a case study FE analysis of a fishing vessel's onboard vibrations due to excitation of the propellers and onboard machinery. The fluid-structure coupling is simplified by taking the fluid as an added mass. The analysis was validated with measurements of the vibrations of the fishing vessel.

It is clear that in previous research modelling of the acoustics has been done thoroughly in different manners and focusing on different wave propagation patterns within a ship. The next step in research would be to look into the mitigation of underwater radiated noise.

In the past, various documents have been written concerning the mitigation of ship noise caused by mechanical processes on-board. Most of these documents focus on the noise on-board of the ship in the different compartments. However, recently more attention is drawn to the negative effects of underwater radiated noise of ships on marine mammals and mitigation should not only be done for on-board purposes. Combined with more advanced modelling techniques that are available now, the amount of available advanced analyses of mitigation methods for the underwater radiated noise of ships is scarce.

Buiten and De Regt (1987) wrote an extensive design manual on how to reduce on-board noise due to the propellers and on-board machinery. This manual is old and outdated and design values are not based on the accurate numerical computations that are required for complex structures such as ships.

Gangemi (2015) presented methods to attenuate the underwater radiated noise of a submarine. Passive, active and hybrid methods are discussed.

Herve et al. (2018); Yanhe et al. (2019) both performed an assessment of the onboard noise of a case study ship. Herve et al. (2018) analysed the vibration on a RORO ship due to the propellers using the SEA and found that the vibrations can be well attenuated by insulating the deck and the cabins. Yanhe et al. (2019) analysed the vibrations onboard a hospital ship due to the propellers using the FEM and found that those vibrations can be adequately mitigated by attaching constrained damper plates above and around the propellers.

Strietman et al. (2018) proposes methods to reduce the underwater radiated sound of ships and also includes operational and economical measures. None of these measures and their effects are analysed extensively.

A research gap has been identified in the modelling of mitigation methods of the underwater radiated noise from ships with a focus on marine mammals. Up until now, most research has focused on the attenuation of vibrations on board a ship or radiated noise due to the propellers. At all times, the focus was either on human comfort or the radiated noise in general, however, for marine mammals certain frequency bands are of greater importance as can be seen in Figure 1.1.

1.3. Research Objective, Questions, Scope and Scale

The project goal is to be able to quantitatively predict and mitigate the underwater radiated noise of a ship in the design phase. There are multiple mechanisms and processes that produce contributing parts to the total underwater radiated noise. All parts follow the same structure, there is a source, a transfer path and a receiver. From Table 1.1 different paths can be identified by combining one from every column. It is clear that the entire acoustic footprint of a ship is a complex process that takes elaborate work to analyse. For time considerations this research will be specified to the following path: On-board machinery (e.g. engine) – foundation – ship structure – water. All other paths that convey acoustic vibration are omitted in this research and will be left for future studies.

Table 1.1: Different Sources, Paths and Receivers in the Acoustics of a Ship

Source	Transfer path	Receiver
Engine	Structure	On-board cabin
Propeller	Air	Water
Shaft	Fluid	
Generator		
Auxiliary machinery		

The chosen path needs to be clarified in terms of the scope. The scope of this research is mainly focused on the acoustics and dynamics of the source, in this case the ship. It will be investigated how the acoustic waves, imposed by the ship's machinery, propagate through the structure towards the water. Propagation patterns in the water and combined effects of multiple ships are not looked at. The scale is thus purely on the ship's level and no large scale underwater combined acoustics. The underwater radiated noise will be computed in the far-field, which means at a distance where the sound radiation directivity of the ship does not change with distance (Zhang et al., 2019). The far-field noise can be converted to the equivalent source level of the ship, which can be compared to reference ships and ship noise models (M. Ainslie et al., 2009). Furthermore, M. Ainslie et al. (2009) believes that the source level is a source property independent of environmental effects such as the water depth and bathymetry. This viewpoint is adopted, leading to the elimination of environmental effects.

Possible mitigation methods will be researched through means of a literature study. The most promising methods will be elaborated upon and their effect on the URN will be analysed. Certain parameters of the method influence the effectiveness and thus the influence of a change in method parameters will be discussed.

To summarise, the research goal can be formulated as follows:

Predict and mitigate the structure-borne underwater radiated noise of a ship in the design phase caused by onboard machinery.

To reach the aforementioned goal, the following research questions will be answered:

How can the underwater radiated noise (URN) of a ship be mitigated for marine mammals in terms of underwater radiated noise caused by onboard machinery?

In what frequency bands is most harm caused to marine mammals?

How can the ship and its machinery be modelled for the purpose of computing the URN in the right frequency bands?

What mitigation methods exist to attenuate the vibrations from onboard machinery?

How can the selected mitigation methods be modelled for the purpose of computing the effects on the URN?

What is the influence of changing parameters of the mitigation methods on the URN?

1.4. Report Outline

To obtain an answer to the aforementioned questions the report systematically structured. The outline of the report is explained here. Chapter 1, the introduction, sets the scene for this research by explaining the problem, the current state of research and the need for this research. Furthermore, the scope is set and the research objective and questions are posed.

After the introduction, Chapter 2 gives the background and the required theoretical knowledge for this research by means of a literature study. It is explained what types of marine mammals live in the oceans and what frequencies they used as well as the frequencies used by anthropogenic sound sources. Subsequently, attenuation methods for the underwater radiated noise are explored. Finally, modelling techniques for the underwater radiated noise and the physical processes involved are explained.

Chapter 3 explains the methodology used in this research in order to come to the answers to the research questions. It is explained how the models are constructed and why certain properties are as they are. Reference data is collected and the framework for the models is set up.

Chapters 4 and 5 describes the results found by the models and shows the necessary graphs and figures to explain the results. The results are interpreted, evaluated and placed into perspective taking into account the assumptions made during the setup of the models.

Finally, in Chapter 6 the research is concluded and recommendations for further research are proposed.

Figure 1.3 demonstrates the approach used in this study, along with the chapters in which it can be found.

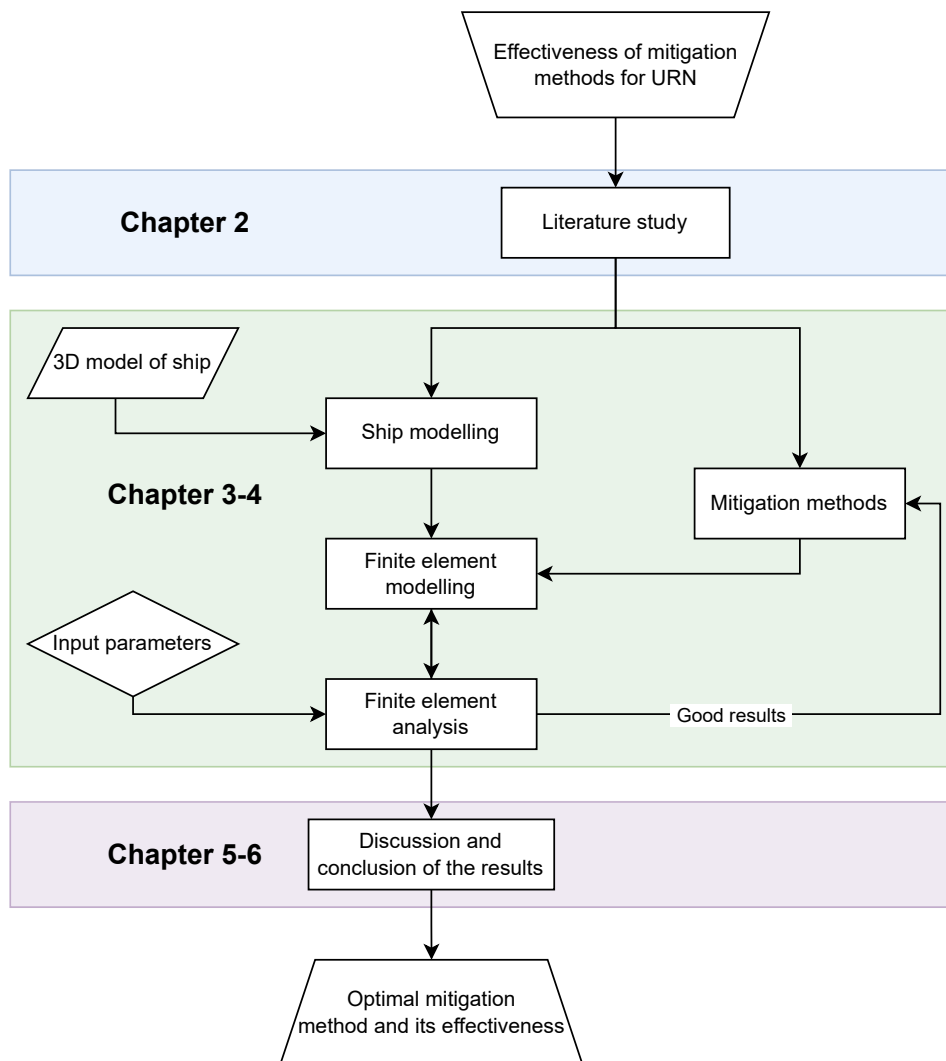


Figure 1.3: Flowchart of the Research and Report.

2

Literature Study

This chapter explains the background of this thesis and provides the necessary knowledge needed to understand all the steps taken. The chapter starts by explaining the underwater sources of sound and noise, such as marine mammals and ships, and how these sources can be compared using acoustic metrics. Subsequently, the modelling techniques for underwater radiated noise are explained. Following that, the physics of the problem is described and the modelling techniques are applied. Finally, attenuation methods suitable for the reduction of underwater radiated noise within the scope of this research are explored.

2.1. Marine Life

Marine life comes in all shapes and sizes. Ranging from small plankton to large whales, two examples can be seen in Figure 2.1. The oceans are relatively impermeable to light, and thus many species living in the oceans have evolved to utilise sound for multiple purposes. Underwater sounds are used by marine animals among other processes to locate prey, avoid danger, communicate and navigate. The type of sound that is used varies per purpose and per type of animal. Clicks are used for navigation and communication with others whilst low-frequency moans are suggested to be used for long-distance communication and topological imaging (ClearSeas, 2020). Interestingly, interannual differences in phrasing and spectra of the sounds used in baleen whales have been observed. 13 different species of odontocetes¹ have shown to be capable of echolocation using self-generated sounds in high frequencies. (National Research Council, 2003)



(a) Seal Sitting on a Rock in a Polar Environment. (Picture by The University of New Mexico, 2019)



(b) Humpback Whale Breaching in the Stellwagen Bank National Marine Sanctuary. (Picture by Whit Welles, 2007)

Figure 2.1: Examples of Marine Mammals.

Not only the type of sound and its frequency are important for marine animals when using acoustics. The source sound level plays an important role as it partially influences the propagation distance and the observability of receivers. Cetaceans' levels for echolocation clicks can be as high as 228 dB re 1 μ Pa at 1m² and the highest levels calculated are originating from male sperm whales clicks with a magnitude of 232 dB re 1 μ Pa at 1m (Mohl, Wahlberg, Madsen, Miller, & Surlykke, 2000). Understandably, the high-frequency

¹A family of marine mammals, toothed whales.

²An explanation on the sound level and its propagation underwater is given in Section 2.6.

clicks require large source levels, as those frequencies attenuate rather quickly with distance travelled. High-frequency clicks are used for echolocation and provide good resolution, the source level should be high to maintain a clear sound image when returning to the receiver. Lower frequency signals are found to have lower source levels since the attenuation is significantly lower compared to high-frequency signals. Blue whales and fin whales utilise low-frequency moans for long-distance communication. The level of the moans is spread around a mean value of 170 dB re 1 μ Pa at 1m. (National Research Council, 2003)

In this research, the focus is on marine mammals as opposed to all marine life utilising sound for multiple purposes. Current existing literature mainly discusses marine mammals and only shortly touches upon other marine animals. Although other marine animals do use sounds, the impact of anthropogenic sounds on their behaviour is not thoroughly researched. This category of marine animals includes the loud snapping shrimp which shows sounds of up to 189 dB re 1 μ Pa at 1m in high frequencies (National Research Council, 2003). High frequencies are out of the scope of this research and thus for these reasons the focus is more on marine mammals.

Different marine mammals communicate at different frequency bands. An overview of a selection of the marine mammals and their corresponding frequency range is given in Table 2.1. In the table, the frequency ranges give the lowest and highest frequency produced by the animal. Gaps in the ranges are not shown, but they do exist. The dominant frequencies are the band of frequencies with the highest energy. In addition to the marine mammals characterised in Table 2.1, other marine vertebrates use low-frequency acoustic waves. Examples are sharks that identify food from sound emitting sources and many fish species that communicate using low-frequency sounds. (National Research Council, 2000)

2.2. Anthropogenic Sources of Sound and Ship Noise

Besides marine life, the underwater soundscape has been troubled increasingly by anthropogenic sources since the start of the industrialisation. Anthropogenic sounds are beneficial to mankind, whilst anthropogenic noise is an undesired byproduct. an example of an anthropogenic sound is sonar. Sonar was initially used in 1914 to successfully detect an iceberg 4 km away, two years after the RMS Titanic sank in a tragic accident. More examples of anthropogenic underwater sources are seismic airguns, pile drivers and ships. The latter two of which are identified as sources of anthropogenic noise. The acoustic waves produced are an unintentional byproduct of the main function. (M. A. Ainslie & de Jong, 2016)

M. Ainslie et al. (2009) did extensive research for the estimation of the total acoustic energy for the most prominent anthropogenic sources in the North Sea. The research was based on available measurements of the M/V Overseas Harriette, other ships and source level prediction models. The results of the research can be found in Table 2.2. Columns one and four are important to demonstrate the importance of shipping noise in the total anthropogenic contribution to the soundscape. From Table 2.2 airgun arrays and shipping can be identified as the heaviest contributors. Column one states the annual acoustic power output of a certain source, not taking into account higher attenuation for higher frequencies. Column four shows the total acoustic energy in the water at one point in time originating from a type of source. It is specifically stated by the authors that "this energy estimation is only meant for a first assessment of relevance". This is said due to the fact that no temporal and spatial distributions are taken into account as well as the characteristics of the propagation in a specific sea or ocean. Nonetheless, this table allows us to conclude that shipping is a prominent contributor to the total anthropogenic influence on the soundscape.

An example of an acoustic footprint can be seen in Figure 2.2, where measurements of the M/V Overseas Harriette originally presented by Arveson and Vendittis (2000) are compared to the RANDI (Research Ambient Noise Directionality) noise model. Oftentimes the source level of a ship is determined using models and formulas that compute the source spectral density level. An example of this is the model from Wales and Heitmeyer (2002) where the source level is calculated as a function of the speed V and the length L of the ship:

$$SL_f = 190.5 + 50 \log_{10} \left(\frac{V}{10 \text{kn}} \right) + 20 \log_{10} \left(\frac{L}{150 \text{m}} \right) - 20 \log_{10} \left(\frac{f}{1 \text{Hz}} \right) \quad (2.1)$$

However, as can be seen from Figure 2.2, models come close to predicting reality but for some frequencies the errors are substantial. (M. Ainslie et al., 2009)

Table 2.1: Frequencies Used in Communication and Echolocation by a Selection of Marine Mammals. (National Research Council, 2000)

Species	Frequency Range (Hz)	Dominant Frequencies (Hz)
Selected Baleen Whales		
Gray Whale		
<i>adults</i>	20–2,000	20–1,200
<i>calf clicks</i>	100–20,000	3,400–4,000
Humpback Whale	30–8,000	120–4,000
Finback Whale	14–750	20–40
Minke Whale	40–2,000	60–140
Southern Right Whale	30–2,200	50–500
Bowhead Whale	20–3,500	100–400
Blue Whale		
<i>Atlantic</i>	—	10–20
<i>Pacific</i>	10–390	16–24
Selected Toothed Whales		
Sperm Whale (clicks)	100–30,000	2,000–16,000
White Whale		
<i>whistles</i>	260–20,000	2,000–5,900
<i>clicks</i>	40,000–120,000	—
Killer Whale		
<i>whistles</i>	1,500–18,000	6,000–12,000
<i>clicks</i>	1,200–25,000	—
Bottlenose Dolphin		
<i>whistle</i>	800–24,000	3,500–14,500
<i>clicks</i>	1,000–150,000	30,000–130,000
Selected Seals		
California Sea Lion (in air)	<1,000–<8,000	500–4,000
Harbor Seal (in air)	<100–150,000+	<100–40,000
Grey Seal	100–40,000	100–10,000

Understandably, the models are not exact. A ship is a complex floating structure with multitudes of processes running onboard simultaneously. With a small number of input parameters in a model, the complex underwater radiated noise cannot be modelled with great accuracy. More accurate results are possible, however, more extensive computer models are needed for this.

2.2.1. The Ship as a Source of Underwater Noise

The underwater radiated noise characterised by the acoustic footprint of a ship (see Figure 2.2) is the undesired byproduct of all the processes on-board needed to successfully navigate and operate the ship. The main sources of noise from a ship can be found in Figure 2.3 and are elaborated upon below. [Abrahamsen \(2012\)](#)

- **Propeller:** The propellers are one of the main contributors to ship noise, even more so at higher travel speeds. There are multiple mechanisms involving the propellers that radiate noise underwater. Firstly, vibrations due to displacements of the blades are transferred to the hull of the ship via the shaft or the water. The hull starts to vibrate and transfers the vibrations to the water. Secondly, cavitation around the propeller occurs due to a rapid pressure drop behind the blades which generates noise and lastly, the collapse of the cavitation bubbles that generate high frequencies. There are additional complex mechanisms at play, however, their effects are thought to be comparatively small. ([Wittekind & Schuster, 2016](#))
- **Electric motor:** Machinery on-board including electric motors are located within the ship structure. Most are connected to pipes, ducts, shafts or the ship structure itself accommodating the structure-borne transfer of vibrations caused by the machinery. Besides structure-borne vibrations of the hull,

Table 2.2: Estimation of the Total Acoustic Energy for the Largest Anthropogenic Sources. (M. Ainslie et al., 2009)

Type of source	Order of magnitude estimate of annual average of acoustic power output in the North Sea [GJ/year]	Order of magnitude estimate of frequency [kHz]	Order of magnitude estimate of absorption [dB/km]	Order of magnitude estimate of total (free space) energy $E = W/(2c)$ [kJ]
Airgun arrays	100	0.1	0.0012	8000
Shipping	270	0.3	0.01	3000
Wind farm construction (pile driving)	9	0.1	0.0012	700
Explosions	7	0.1	0.0012	500
Navigation echo sounders	60	30	8.2	0.7
Fisheries sonar	10	30	8.2	0.1
Military search sonar	0.2	10	1.2	0.02

air-borne vibrations occur around the machinery, adding to the structure-borne vibrations. The structure-borne vibrations are transferred to the water resulting in underwater radiated noise. The total resulting noise is for the bigger part dependent on the properties of the machinery, the place within the ship's hull and the type of mounting to the ship's hull. (Abrahamsen, 2012)

- **Diesel generator:** Similar mechanism as 'Electric motor', but different magnitudes dependent on the characteristics of the machinery.
- **Auxiliary machinery:** Similar mechanism as 'Electric motor', but different magnitudes dependent on the characteristics of the machinery.
- **Water flow:** Flow of the water around the hull of the ship generates turbulence and vortices generating noise specifically at higher speeds. Resonance of the vortex frequency and a ship's natural frequency could result in a strong tonal noise. (Abrahamsen, 2012)

It is difficult to say what mechanism onboard a ship is the main contributor to the underwater radiated noise. Ship specifications and operational variables influence the relative contributions. Kozaczka (2000) states that at low ship speeds the diesel generator is the main contributor to the underwater radiated noise and for moderate ship speeds, the electrical motor is the main source. However, Ross (1976) argues that cavitation can account for 80% – 85% of the noise from a ship. The speeds corresponding to these values are unclear. Numerous processes influence the total underwater radiated noise from a ship. Because of the complex nature and the relations between those processes, it is impossible to give values of the relative contributions of the different processes to the total underwater radiated noise.

2.3. Noise Mitigation Methods

Reduction of underwater radiated noise from ships can be done in numerous ways. Technical adjustments and solutions exist, however, extensive papers have additionally been written on operational or economical measures. Economic measures rely on higher fees for louder ships (Strietman et al., 2018) and thus stimulate shipbuilders and operators to realise quieter ships. Operational measures include a reduction in cruising speed (Leaper, 2019; Veirs, Veirs, Williams, Jasny, & Wood, 2018) and a change in trajectory (Audoly & Rousset, 2014). Within the scope of this research, only technical measures capable of reducing the low-frequency structure-borne noise from machinery vibrations are considered. In the consideration, it is assumed that all operational conditions of the ship remain constant, such as cruising speed, trajectory and draft such that the influence of these changing conditions on the URN is eliminated.

Promising technical mitigation methods exist for reducing the URN from machinery vibrations. Williams, Veirs, Veirs, Ashe, and Mastick (2019) state that for new ship types an approximated reduction of 10 dB is possible with an increase in construction and production costs of only 1%. On ships where machinery noise dominates, placing the diesel engines on a resilient foundation could achieve this reduction of 10 dB in URN. After conducting measurements, Nilsson (1978) confirms this by concluding properly designed resilient mounted decks could reduce structure-borne noise in the order of 10 dB. Tuned mass dampers (TMD) have also been

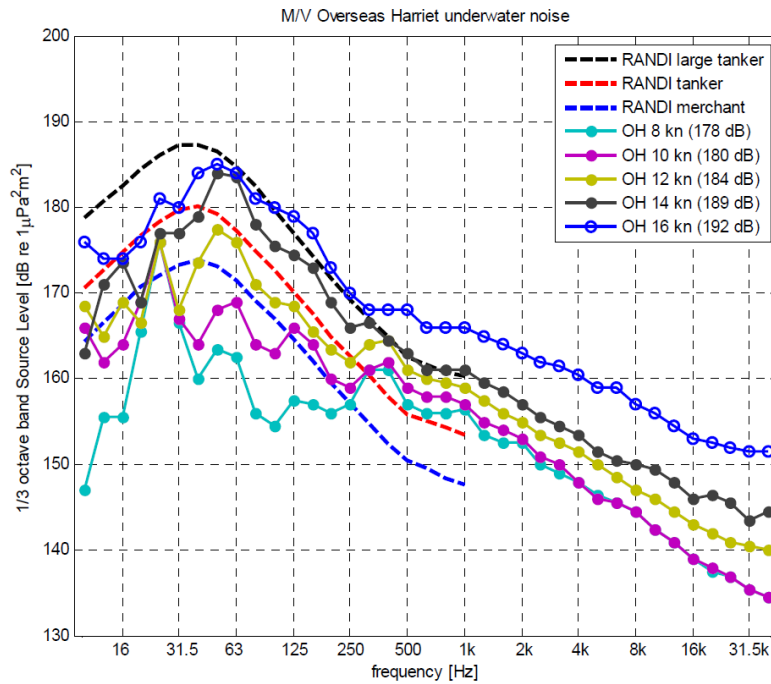


Figure 2.2: Source Level Noise of the M/V Overseas Harriete and RANDI (Research Ambient Noise Directionality) Model Ships. (M. Ainslie et al., 2009)

proposed and show promising results. Kakinouchi, Asano, Tanida, and Takahashi (1992) found a reduction of 80% of the structural accelerations when using an active TMD. Hsueh and Lee (1994, 1995) also reported significant decreases (up to 90%) of the acceleration of the highest resonance peaks of the ship. The effect of the reduced acceleration on the mitigation of underwater radiated noise is not documented, however, it is evidently positive. Other mitigation methods have been proposed such as increased structural damping, bubble curtains, structural adjustments and hull optimizations. The latter two of which should be implemented in the design phase of the ship. The other mitigation methods can be retrofitted on existing ships or implemented in newly designed ships. (Audoly et al., 2017)

An extensive amount of literature confirms the suitable application of resilient mounts for the attenuation of structure-borne URN caused by the machinery. Measurements of the effect of a resilient mount on a test bed have shown reductions in noise of 20 – 40 dB. However, for engines mounted on ships, the reductions are typically 10 dB for medium frequencies and 20 dB for high frequencies. This is much higher than the potential

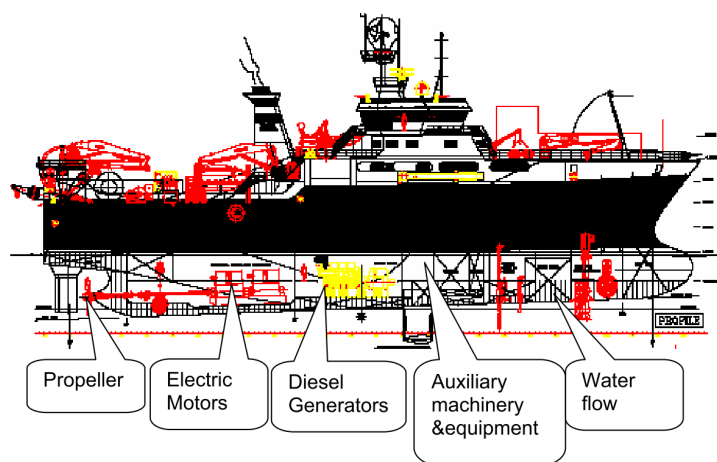


Figure 2.3: Most Common Sources of Noise on a Ship. (Abrahamsen, 2012)

of structural reinforcements and adjustments towards reducing the URN. (AQUO-SONIC, 2015)

Furthermore, Port of Vancouver (2017) confirmed the claims made by AQUO-SONIC (2015) and rated resilient mounts, structural reinforcements and propeller cleaning 'high' in the category 'Evidence of Noise Reduction Effectiveness'. All other URN reduction measures are rated low or medium.

These claims and references support the decision to look at resilient mounts in this research.

2.3.1. Resilient Mount

A resilient mount is a structure placed underneath the ship's machinery, capable of dissipating the vibration energy. The resilient mounts and the machinery combined form a mass-spring-damper system that mitigates the transmission of the vibrations from the machinery to the foundation of the ship. Less energy in the system and reduced vibrations eventually result in a decrease of the underwater radiated noise of the ship. A 2D schematic of an engine on a resilient mount can be seen in Figure 2.4.

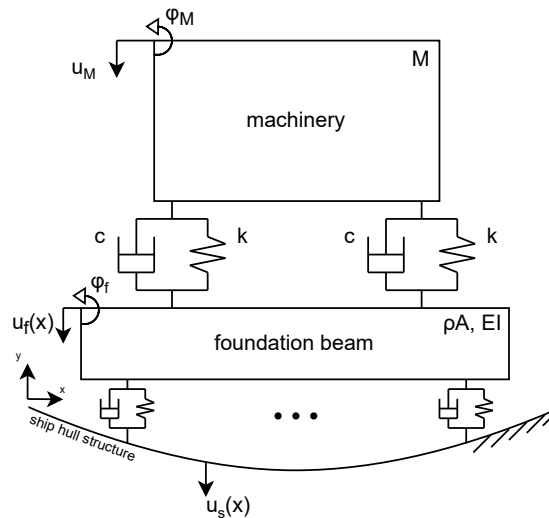


Figure 2.4: A Schematic Example of a Resilient Mounting System Applied to the Machinery of a Ship.

Figure 2.4 shows the dynamic free body diagram. The movements in the x-direction are left out for clarity of the diagram. In reality, the spring-damper units also constrain the machinery in x-direction. The machinery on top has 6 degrees of freedom (DOF) in the 3D case and 3 DOFs in the 2D case. Without movements in the x-directions 2 DOFs remain, y-translation u_M and rotation ϕ_M . The machinery is often supported by multiple resilient mounts schematised as a spring-damper unit. The resilient mounts rest on the foundation beams of the ship. The foundation beams have mass and stiffness and can bend. In the 2D case the DOFs for the beam are the translation (including deflection) of the beam $u_f(x)$ and the rotation ϕ_f . The foundation beams are then supported by the ship's hull structure consisting of stiffeners and girders schematised again as a spring-damper unit. The stiffness and damping come from the bending stiffness of the beam and the structural damping. The hull structure has a vertical displacement DOF $u_s(x)$. Connected to the hull structure is the ship's shell plating. All separate elements function as a complete system, meaning that movements of the beam influence the movements of the machinery and vice versa.

The vibrations are initiated by processes in the machinery. Oftentimes, rotating parts and their inertia result in oscillatory accelerations of the machinery. The accelerations combined with the mass M of the machinery result in an oscillating force acting on the resilient mount. The resilient mount transfers this vibration force to the foundation beam. The foundation beam then transfers the vibrations to the hull structure from where the energy is radiated into the water. However, being a coherent dynamical system, the pressure fluctuations in the water transfer forces to the hull structure, the foundation beam and the machinery. Influencing the vibrations in the system as well.

2.3.2. Physics of the Resilient Mount

In a resilient mount, the damping and stiffness can be tuned to achieve the desired dynamic effects on the system. The effectiveness of a resilient mount can best be explained using the simplified dynamic response of a basic SDOF mass-spring-damper (mck) system to a harmonic force with an amplitude of 1 N. This is overly simplified compared to Figure 2.4, however, the physical principles are similar.

The equation of motion (EOM) for the basic mck-system:

$$m\ddot{u}(t) + c\dot{u}(t) + ku(t) = Fe^{i\omega t} \quad (2.2)$$

Where m , c and k are respectively the mass, damping and stiffness of the system. F is the amplitude of the forcing, ω is the frequency of the forcing and $u(t)$ is the response of the system. This can be rewritten as:

$$\ddot{u}(t) + 2\zeta\omega_n\dot{u}(t) + \omega_n^2u(t) = fe^{i\omega t} \quad (2.3)$$

Where $\zeta = \frac{c}{2m\omega_n}$, $\omega_n = \sqrt{\frac{k}{m}}$ and $f = \frac{F}{m}$. We assume the solution $u(t) = \tilde{U}(\omega)e^{i\omega t}$ and substitute into Equation (2.2):

$$-\omega^2\tilde{U}(\omega)e^{i\omega t} + i\omega 2\zeta\omega_n\tilde{U}(\omega)e^{i\omega t} + \omega_n^2\tilde{U}(\omega)e^{i\omega t} = fe^{i\omega t} \quad (2.4)$$

Which can be rewritten:

$$\tilde{U}(\omega) = \frac{f}{-\omega^2 + i\omega 2\zeta\omega_n + \omega_n^2} \quad (2.5)$$

$$\tilde{U}(\omega) = \frac{f}{k} \frac{1}{\sqrt{\left(1 - \left(\frac{\omega}{\omega_n}\right)^2\right)^2 + \left(2\zeta\frac{\omega}{\omega_n}\right)^2}} \quad (2.6)$$

In which the second multiplier is the dynamic amplification factor (DAF) plotted in Figure 2.5 for different values of ζ . Changing the stiffness k will not result in visible changes in Figure 2.5 as it influences only the eigenfrequency of the system. If the x-axis is not normalised, a shift in the peaks to the left or right can be achieved by adjusting the stiffness k .

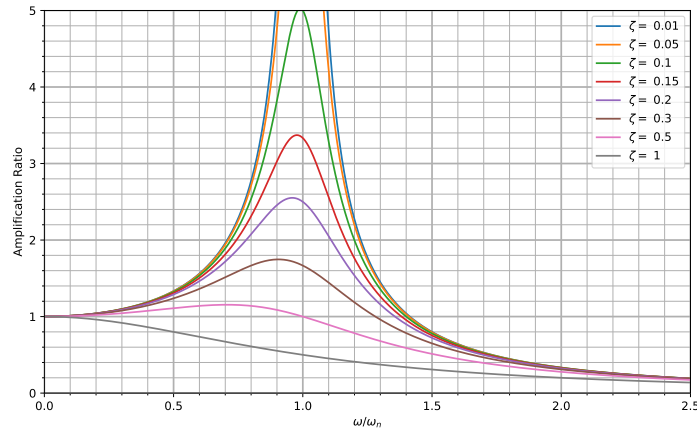


Figure 2.5: The Dynamic Response of a Mass-Spring-Damper System.

There are a number of interesting dynamic phenomena that can be seen in Figure 2.5. First of all, the damping in a system shifts the eigenfrequency down. The peaks of the DAF for a larger ζ is shifted to the left, up to the point where there is no distinguishable peak at $\zeta = 1$, also called critically damped.

Secondly, the damping strongly influences the peak response of the system around the eigenfrequency. It can be seen that the peaks are significantly reduced for an increase in ζ . For $\zeta = 0$ the response at the eigenfrequency is infinite and has no real physical meaning. In reality, this leads to resonance in the structure

that leads to larger and larger deflections and eventually failure. A real case example is the infamous Tacoma Narrows Bridge collapse in 1940.

Lastly, at low frequencies, the influence of the damping starts to decrease. The damping in a system is proportional to the velocity (see Equation (2.3)). Energy is taken out of the system during every oscillation of the system. This occurs at most when the velocity is the highest. At lower frequencies, the system oscillated with large periods of time between two full oscillations. The corresponding velocity at very low frequencies is low and thus the influence of the damping on the system is low. At high frequencies, inertial effects take over and the total response of the system goes towards zero.

2.4. Modelling Techniques for Underwater Radiated Noise

Due to the complex nature of the problem of underwater radiated noise from ships, advanced computational models can be useful for understanding the effects of certain changes in design to new and existing ships. The models allow users to analyse the design of a ship including proposed adjustments, vibration mitigation methods and expected operational conditions. The types of computational models that could be applied are: (International Maritime Organisation, 2014)

- Computational Fluid Dynamics (CFD): used for the prediction of the flow around the hull and through the propellers;
- Statistical Energy Analysis (SEA): used to estimate the high-frequency noise and vibrations, mainly originating from the machinery;
- Finite Element Analysis (FEA): used to predict the vibrations of the ship structure excited by the propellers and machinery;
- Boundary Element Method (BEM): used for the prediction of the vibrations in the fluid domain. Often used together with the FEA and coupled at the ship-fluid boundary with fluid-structure interaction.

Within the scope of this research, a combination of the FEA and the BEM is advised for the assessment of the effect of mitigation methods on the low-frequency underwater radiated noise originating from the machinery. This approach was also concluded Zhang et al. (2019) in Section 1.2. In Sections 2.4.1 and 2.4.2 the main principles and origin of the FEA and BEM are explained. Application of the techniques to the problem at hand can be found in Sections 2.5 to 2.7.

2.4.1. Finite Element Analysis (FEA)

The Finite Element Analysis (FEA), also referred to as the Finite Element Method (FEM) is a way of analysing a complex system by splitting it into multiple small, less-complex elements. The complex system is simplified using a finite number of discrete components (Zienkiewicz, Taylor, & Zhu, 2005). In this way, the original problem described by differential equations ('strong form') is converted to a set of algebraic equations ('weak form') that can be systematically solved for the unknown quantities and is suitable for computer calculations. FEM is capable of handling irregular boundaries, complex geometries, different materials and boundary conditions throughout the structure and more (Colomé, 2020).

A standard generalised procedure for conducting a FEA consists of five main steps:

1. Discretisation of the domain
2. Defining the shape function or interpolation functions
3. Formulation of the system of equations
4. Assembly of the global system
5. Solve the global system of equations

The steps are visualised in Figure 2.6, yellow boxes indicate processes performed by the user and green boxes indicate processes performed by the FEM software used.

Discretization of the domain

Discretization of the domain is the first step in performing a FEA. The complex structure is broken down into a finite amount of elements. Multiple element types can be used to divide the structure, as can be seen in Figure 2.7. The top and bottom rows of the elements are called linear and quadratic respectively. The type and size of the elements influence the accuracy of the results, but also the required computational time. Quadratic elements are more accurate, but longer computational times are required. Discretization of the domain is also called 'meshing'.

Defining the shape functions

The next step after discretizing the domain is defining the shape functions. The shape functions are functions that describe the area and the link between the nodes. Shape functions are often polynomial functions that are assumed as an approximation of reality. For linear elements the shape functions are linear and for quadratic elements the shape functions are quadratic.

Formulation of the system of equations

An element in a dynamical problem is described by equations of motion in the form of differential equations, also called the 'strong form'. Using the shape functions, the differential equations can be described with approximate integral functions, the 'weak form' of the problem. The integral form of the problem is easier to solve and allows for the mass and stiffness matrix to be derived. The weak form of an element k has the following form:

$$\mathbf{M}^k \ddot{\mathbf{u}} + \mathbf{K}^k \mathbf{u} = \mathbf{f}^k \quad (2.7)$$

Where \mathbf{M}^k is the elemental mass matrix, \mathbf{K}^k is the elemental stiffness matrix, \mathbf{f}^k is the force vector acting on the element and $\ddot{\mathbf{u}}$ and \mathbf{u} are respectively the vectors for the accelerations and displacements of the DOF's of element k . (Colomés, 2020)

Assembly of the global system

The matrices \mathbf{M}^k and \mathbf{K}^k are $n \times n$ -dimensional, where n is the amount of DOF's per element. In the full problem, numerous elements are interconnected and a global system, similar to eq. (2.7), has to be assembled. The different elemental matrices \mathbf{M}^k and \mathbf{K}^k are combined for all elements, taking into account the elements' orientation relative to the global coordinate system. A transformation procedure is applied to \mathbf{M}^k and \mathbf{K}^k to transform the element properties from the local coordinate system of element k to the global coordinate system. This process yields the global system:

$$\mathbf{M}\ddot{\mathbf{u}} + \mathbf{K}\mathbf{u} = \mathbf{f} \quad (2.8)$$

The next step is to impose the boundary conditions of the system. Known quantities for displacements, accelerations or forces on specific nodes can be substituted into the respective vector in eq. (2.8). (Colomés, 2020)

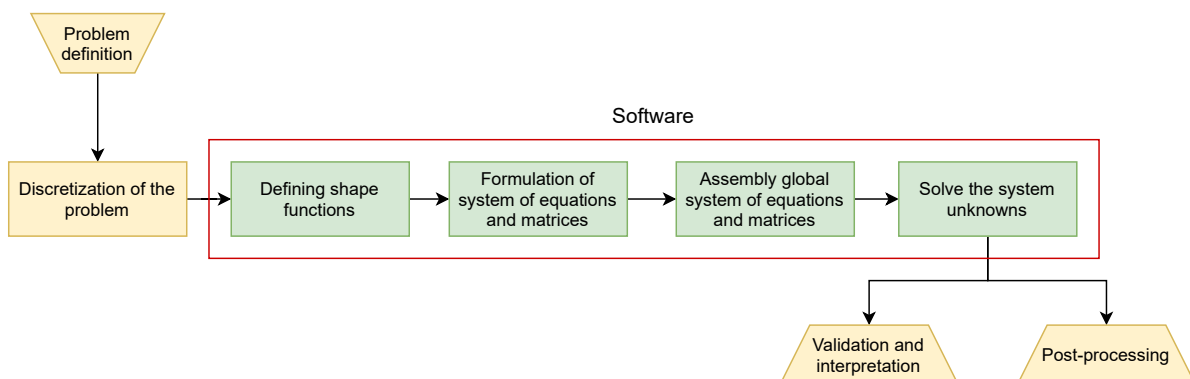


Figure 2.6: Flowchart Visualising the Process for a FEA.

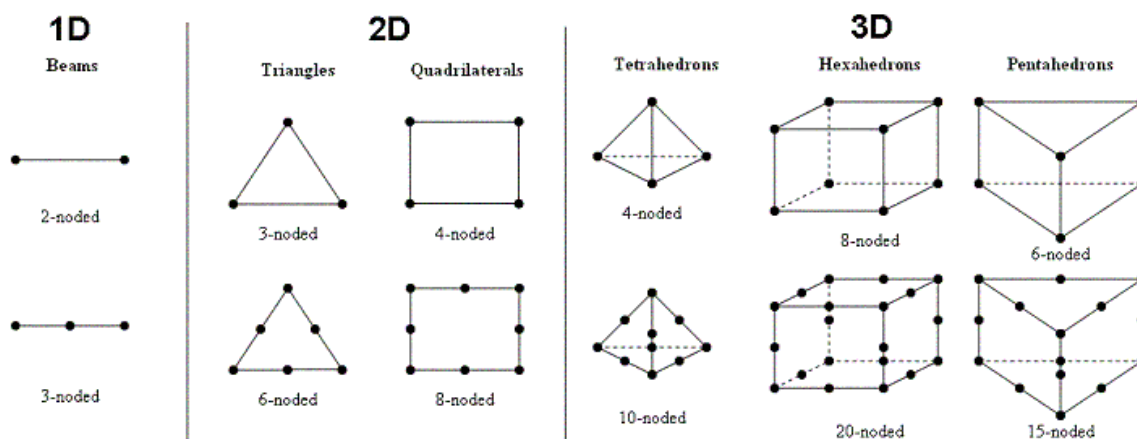


Figure 2.7: Different Element Types Used in FEM. (Açikgöz, 2019)

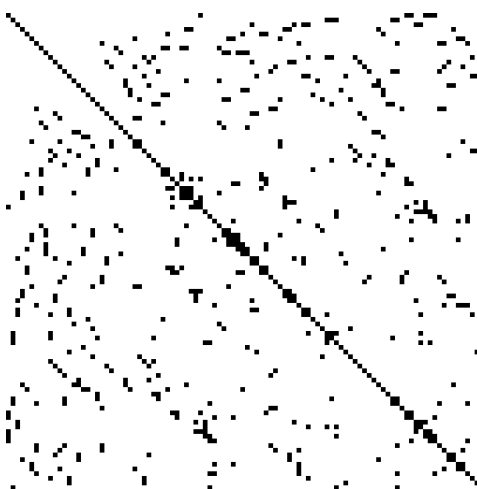


Figure 2.8: A Typical Example of a Sparse Matrix for a FEA. (Alexandrov, 2007)

Solve the global system of equations

The global system from eq. (2.8) can be solved for the unknown system parameters. The matrices \mathbf{M} and \mathbf{K} are large sparse matrices, meaning a matrix that consists of mainly zero values. A typical example of a sparse matrix for a FEM problem can be seen in Figure 2.8, white indicates a zero entry in the matrix and black indicates a non-zero entry in the matrix. FEM sparse matrices are usually substantial and advanced solvers are implemented to solve the global system.

The FEA procedure explained above is general and applicable to any structure or similar problem. The procedure is similar for fluids, however, a different differential equation is used as a starting point and the elemental and global system of equations have slightly different definitions. Application of the FEM to the acoustics of a ship is shown in Section 2.5.

2.4.2. Boundary Element Method (BEM)

The boundary element method (BEM) is similar to FEM in the sense that it converts the (partial) differential equation into integral form that results in a system of linear algebraic equations. The main difference with the FEM is that with the BEM only a mesh of the boundary of the domain is required in contrast to discretizing the entire domain into smaller elements. (Kirkup, 2007)

The BEM is a valuable alternative for the analysis of problems, especially for exterior problems where the outer boundary can be assumed to be at an infinite distance. The ocean around a noise radiating ship is an example of this as the ocean is large enough to be considered infinite when modelling. Applying the FEM to large domains such as an ocean requires thorough thinking to not create an excessive amount of elements

unnecessarily increasing the calculation costs. When choosing the BEM for this situation, simply a mesh at the boundary of the domain (the wet surface of the ship) is required. A reduced time for meshing and for the numerical computation of the solution is the result. (Kirkup, 2007)

Figure 2.9 shows the discretization of an external 2D-problem using the BEM. The domain S is divided in n smaller elements, also called panels, such that $\tilde{S} = \sum_{i=1}^n \Delta \tilde{S}_i$. The problem can be described by the Helmholtz equation, the Sommerfeld radiation condition and the boundary conditions along the boundary S . Extensive mathematical operations on this initial problem statement yield the solution to the problem of ship radiation into an infinite domain E in an efficient manner. For detailed instructions on the BEM the author refers to Kirkup (2007), who documented all steps in great detail.

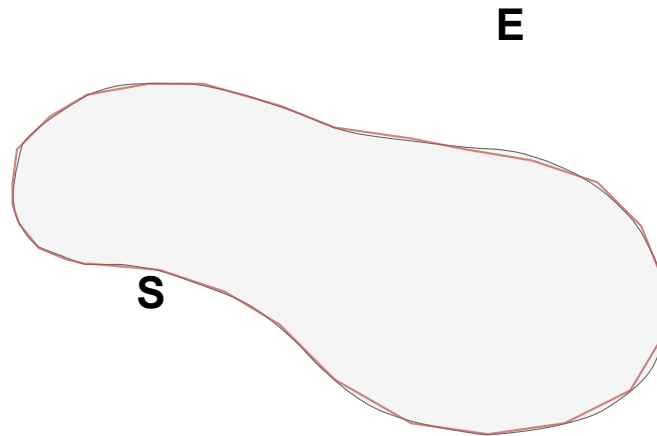


Figure 2.9: The Domain and Discretization for an External 2D-Problem.

2.5. Structural Acoustics

Sound and noise are characterised by waves travelling through a medium. In this section, sound travelling through a solid medium is discussed. The acoustics within a structure can be divided into four subcategories, as seen in Figure 2.10. Generation includes the source of the vibrations that start the acoustic process. Transmission is the mechanism that conveys the vibrations from the generating source to the structure. Propagation is defined as the process where the vibration energy is divided and transferred throughout the structure. And lastly, the energy of the vibrations is radiated outwards from the structure to air or water. In the problem of URN in this thesis, the generation is caused by the ship's machinery, the transmission is done through the mounting mechanisms of the ship's machinery to the hull structure and the radiation is realised by means of outwards radiation from the ship's wet hull surface into the water. (Cremer et al., 2005)

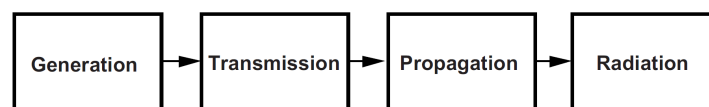


Figure 2.10: The Process of Acoustics in a Structure. (Cremer et al., 2005)

Several different types of waves exist within structures. Similar to air or water, within a structure longitudinal waves are present. Moreover, structural elements are able to resist shear forces, accommodating the presence of shear waves. Furthermore, oftentimes a structure has one or two dimensions significantly smaller with respect to the length of the waves. These structural elements are called plates and beams and are able to vibrate using bending (flexural) waves. Examples of the different types of waves are shown in Figure 2.11. (Hambric, 2006)

All waves and wave types can be described fundamentally by the wave characteristics found in Figure 2.12. An (acoustic) wave can be described by a fluctuating quantity (dependent on the type of wave) around the mean quantity of the medium. In Figure 2.12 the fluctuating quantity is the pressure in longitudinal waves, but for bending waves the quantity would be the displacement of the structural element. The waveform

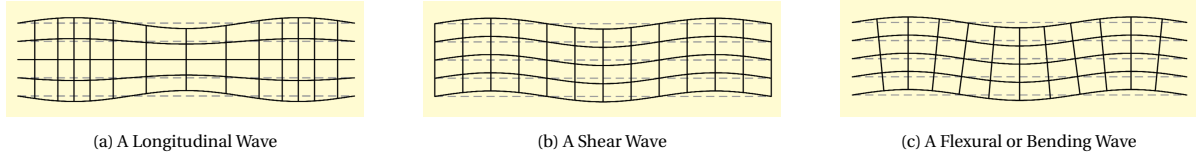


Figure 2.11: Different Types of Waves in Structures. Displacements are Exaggerated. (Hambric, 2006)

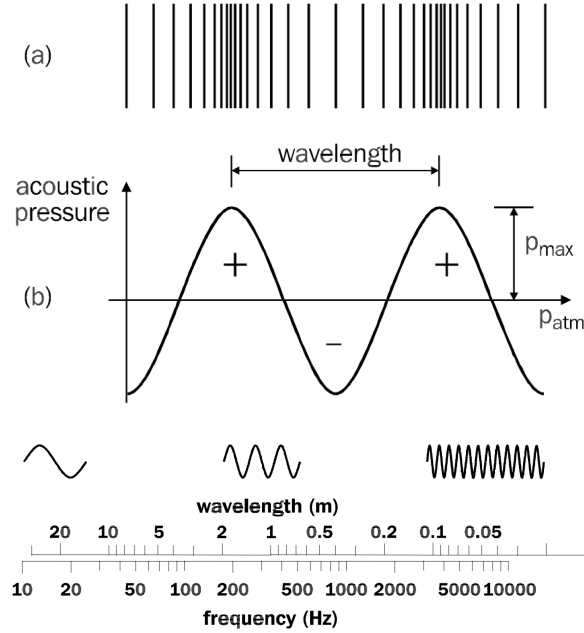


Figure 2.12: Characteristics of Waves. (Hansen, 2001)

can be characterised by an amplitude, wavelength, wave speed, frequency and wave period. The amplitude (p_{max}) and wavelength of a wave are as seen in Figure 2.12. The wavelength λ , the wave speed c , the frequency f and the period T are related by: (Hansen, 2001)

$$c = f\lambda \quad (2.9)$$

$$T = 1/f \quad (2.10)$$

Most of the sound radiated from a structure is due to flexural waves. The main reason for this is that flexural waves move the structure transversely, producing waves in the adjacent fluid domain (Hambric, 2006). For acoustics, the transient response of the structure is not often looked at, instead, it is more useful to look at the response in the frequency domain. The global system that is solved to obtain the frequency response spectrum of the ship is of the same form as Equation (2.8), this time including the damping within the structure:

$$\mathbf{M}\ddot{\mathbf{u}} + \mathbf{C}\dot{\mathbf{u}} + \mathbf{K}\mathbf{u} = \mathbf{f} \quad (2.11)$$

Under the assumption that the excitation \mathbf{f} and the response displacement \mathbf{u} have time-harmonic frequency dependence $e^{i\omega t}$, this can be written in the frequency domain as:

$$-\omega^2\mathbf{M}\tilde{\mathbf{u}}(\omega) + i\omega\mathbf{C}\tilde{\mathbf{u}}(\omega) + \mathbf{K}\tilde{\mathbf{u}}(\omega) = \tilde{\mathbf{f}}(\omega) \quad (2.12)$$

Rewrite to obtain to the complex frequency response matrix $\mathbf{H}(\omega)$:

$$(-\omega^2\mathbf{M} + i\omega\mathbf{C} + \mathbf{K})\tilde{\mathbf{u}}(\omega) = \tilde{\mathbf{f}}(\omega) \quad (2.13)$$

$$\mathbf{H}(\omega) = \tilde{\mathbf{u}}(\omega)\tilde{\mathbf{f}}(\omega)^{-1} = (-\omega^2\mathbf{M} + i\omega\mathbf{C} + \mathbf{K})^{-1} \quad (2.14)$$

However, in acoustics often the velocity is used in contrast to the displacement. A reason for this is that this allows for easier computation of the power of a signal, a measure that is suitable in acoustics. Derivation of the response spectrum considering the velocities is done by the substitution of:

$$\tilde{\mathbf{u}}(\omega) = \frac{\tilde{\mathbf{v}}(\omega)}{i\omega} \quad (2.15)$$

Resulting in:

$$\left(i\omega\mathbf{M} + \mathbf{C} + \frac{1}{i\omega}\mathbf{K}\right)\tilde{\mathbf{v}}(\omega) = \tilde{\mathbf{f}}(\omega) \quad (2.16)$$

$$\mathbf{A}(\omega) = \tilde{\mathbf{v}}(\omega)\tilde{\mathbf{f}}(\omega)^{-1} = \left(i\omega\mathbf{M} + \mathbf{C} + \frac{1}{i\omega}\mathbf{K}\right)^{-1} \quad (2.17)$$

In which $\mathbf{A}(\omega)$ is the admittance matrix, the inverse of the impedance matrix $\mathbf{I}(\omega)$ (Cremer et al., 2005). The impedance is defined as the ratio between the forcing and the velocity of the structure and gives information about the structure's resistance to a forcing (Dalmont, 2001). The system matrices \mathbf{M} , \mathbf{C} and \mathbf{K} are assembled using the methods described in Section 2.4.1.

2.6. Fluid acoustics

Sound waves in a fluid differ from sound waves in air due to the differences in the mechanical property of both mediums. The most important difference is the increased wave speed in a fluid as a result of a higher density. In air, the speed of sound is approximately 340 m/s and in seawater the speed of sound is approximately 1500 m/s. An important consequence of this is that the wavelength of a sound signal with the same frequency is $\frac{1500}{340} \approx 4.4$ times longer in seawater than in air (using Equation (2.9)). Another important difference between air and water in terms of sound is the decibel scale with which the level of the signal is indicated. In air, the unit for the sound level is [dB re 20 μ Pa at 1m] and in water, the unit is [dB re 1 μ Pa at 1m]. The difference in reference pressure for the determination of the decibel level makes a comparison of the two complicated and not straightforward. For example, a supertanker radiating noise at 190 dB re 1 μ Pa at 1m underwater, has a noise level of approximately 128 dB re 20 μ Pa at 1m in air. (Nieukirk, 2015)

In fluid acoustics, a distinction can be made between internal and external situations. An internal problem includes boundary conditions on all sides of the domain and is solved by utilising the conservation of mass and momentum (Navier-Stokes) equations. An external problem is characterised by a domain without boundaries accommodating acoustic waves that propagate into infinity. A typical example of this is a radiating submerged structure in an infinite fluid. The external problem can be solved by applying the Helmholtz equation and the Sommerfeld radiation condition at infinity, however, other methods exist as well. (ANSYS, 2021)

In an external radiating acoustics problem different fields can be defined each denoting a space with different characteristics. The different types of fields are: (Hansen, 2001)

- **Free field:** Propagation of sound is possible without any obstructions.
- **Near field:** Region within one wavelength or three times the largest dimension of the radiating structure. The particle velocity and the sound pressure are not in phase in the field.
- **Far field:** Defined as the field that starts where the near field ends and extends into infinity. In the far-field, the sound level decays by 6dB for each doubling of the distance from the sound source.
- **Direct field:** The field that consists of sound coming directly from the source, without being influenced by reflections from boundaries or objects.
- **Reverberant field:** The field coming from the source indirectly by means of reflection from a boundary or object.

The complex shape of a ship and the different placements of the machinery equipment on-board results in a directivity pattern of the URN of the ship. In all directions around the ship the radiated sound properties can differ. Analytical formulations do not suffice in the determination of the URN due to the directivity effect and instead, numerical simulations are utilised.

Using the methods as described in Sections 2.4.1 and 2.4.2, the matrix system describing the fluid acoustics is obtained from the governing differential equations:

$$\mathbf{M}_F \ddot{\mathbf{p}} + \mathbf{C}_F \dot{\mathbf{p}} + \mathbf{K}_F \mathbf{p} + \bar{\rho}_0 \mathbf{R}^T \ddot{\mathbf{u}} = \mathbf{f}_F \quad (2.18)$$

In which \mathbf{M}_F , \mathbf{C}_F , \mathbf{K}_F and \mathbf{R}^T are the acoustic fluid mass, damping, stiffness and boundary matrices respectively, \mathbf{f}_F is the acoustic fluid load vector, \mathbf{p} is the nodal pressure vector, $\bar{\rho}_0$ is the acoustic fluid mass density constant and $\ddot{\mathbf{u}}$ is the nodal acceleration vector at the boundary. The system matrices are derived using the methods described in Sections 2.4.1 and 2.4.2 using shape functions and the weak form (integral) notation of the governing differential equations.

2.7. Fluid-Structure Coupling

Due to the higher density of water compared to air the fluid-structure interaction occurs at the interface of the structure and the water. The interface of the structure and the air has negligible fluid-structure interaction effects.

At the interface between the ship's hull and the water, there is interaction between the fluid and structure. The vibrations of the structure press against the fluid and cause pressure fluctuations in the fluid. On the other hand, pressures in the fluid exert forces onto the structure resulting in displacements of the structure. This process is called fluid-structure interaction (FSI) and in short, it implies that the normal particle velocity of the structure and the fluid are equal at a given place. The in-plane or tangential particle velocity is not necessarily equal for the fluid and the structure. (Hambric & Fahnlne, 2007)

The FSI can be described mathematically and is done in the remainder of this section. The matrix equations found for the structure and the fluid in respectively Sections 2.5 and 2.6 are recalled in Equations (2.19) and (2.20) using the subscript S for structure and F for fluid.

$$\mathbf{M}_S \ddot{\mathbf{u}}_S + \mathbf{C}_S \dot{\mathbf{u}}_S + \mathbf{K}_S \mathbf{u}_S = \mathbf{f}_S \quad (2.19)$$

$$\mathbf{M}_F \ddot{\mathbf{p}}_F + \mathbf{C}_F \dot{\mathbf{p}}_F + \mathbf{K}_F \mathbf{p}_F + \bar{\rho}_0 \mathbf{R}^T \ddot{\mathbf{u}}_F = \mathbf{f}_F \quad (2.20)$$

The fluid particle acceleration at the boundary $\ddot{\mathbf{u}}_F$ is the same for the fluid as for the structure and thus the subscripts of the structure displacements \mathbf{x} and fluid pressures \mathbf{p} are removed. Furthermore, because the fluid is only forced by the structure and the structure is forced by the fluid, the forcing term in the fluid equation is 0 and the forcing term in the structure equation is supplemented:

$$\mathbf{M}_S \ddot{\mathbf{u}} + \mathbf{C}_S \dot{\mathbf{u}} + \mathbf{K}_S \mathbf{u} = \mathbf{f}_S + \mathbf{f}_F \quad (2.21)$$

$$\mathbf{M}_F \ddot{\mathbf{p}} + \mathbf{C}_F \dot{\mathbf{p}} + \mathbf{K}_F \mathbf{p} + \bar{\rho}_0 \mathbf{R}^T \ddot{\mathbf{u}} = 0 \quad (2.22)$$

Where the fluid forcing vector $\mathbf{f}_F = \mathbf{R}^T \mathbf{p}$. (Zhang et al., 2019)

The final coupled fluid-structure system can be obtained by combining Equations (2.21) and (2.22):

$$\begin{bmatrix} \mathbf{M}_S & 0 \\ \bar{\rho}_0 \mathbf{R}^T & \mathbf{M}_F \end{bmatrix} \begin{Bmatrix} \ddot{\mathbf{u}} \\ \ddot{\mathbf{p}} \end{Bmatrix} + \begin{bmatrix} \mathbf{C}_S & 0 \\ 0 & \mathbf{C}_F \end{bmatrix} \begin{Bmatrix} \dot{\mathbf{u}} \\ \dot{\mathbf{p}} \end{Bmatrix} + \begin{bmatrix} \mathbf{K}_S & -\mathbf{R}^T \\ 0 & \mathbf{K}_F \end{bmatrix} \begin{Bmatrix} \mathbf{u} \\ \mathbf{p} \end{Bmatrix} = \begin{Bmatrix} \mathbf{f}_S \\ 0 \end{Bmatrix} \quad (2.23)$$

It is worthy to mention that this notation clarifies what is to be expected from the fluid-structure coupling. An added mass effect of the water to the structure is introduced as is seen by the lower-left term in the mass matrix. The added mass has as a result that the eigenfrequencies of the structure are decreased and the amplitudes are altered.

3

Methodology

This chapter describes the methodology used to answer the research questions. The problem is modelled using FEM, allowing for complex processes to be analysed. To achieve good and practical results, a simplified base model is created in Sections 3.1 to 3.3 with which the basic dynamic and acoustic properties can be studied. After that, a resilient mount is applied to the base model in Section 3.4 to judge the effect of a mount and its changing parameters on the URN. Subsequently, in Section 3.5, the combined model is schematised as a 2-DOF system with a dynamic stiffness representing the base model. The 2-DOF schematisation is used for fast calculations of the normalised effect of resilient mount parameter combinations on the URN, such that no large amount of FEM model runs are needed. Finally, Section 3.6 explains how the data is obtained from the models and how the data is processed.

3.1. Simplification Options

The choice of using a simplified model in contrast to a more detailed model is based on various advantages. The main reason is that a simplified model is easier to work with, especially when errors occur and adjustments need to be made. The error can be more easily identified due to the simpler nature of the model.

The second reason is that interpretation of the results is more straightforward since the processes happening in the model are less complex and easier to understand. More assumptions are made in the simplified model and the influence of those on the results should be considered during the interpretation.

The third reason concerns the computational time required to solve the model. A simplified model consists of less detail and thus fewer nodes and finite elements. Fewer elements lead to a reduced time to solve the model. When modelling errors occur and adjustments need to be made, significant time is saved when a new model run takes less time. Furthermore, when different model scenarios are calculated, substantial time reduction can be achieved on every scenario and thus on the total calculation time.

A simplified model can be achieved in multiple ways and depends on the results that are to be obtained and the required model characteristics and properties needed to achieve the results.

The simplified model is used to obtain a first-order assessment of the URN of a ship and the influence of mitigation methods on this. This is a dynamic and acoustic problem, which is analysed in the frequency range of 0 – 200 Hz (as explained in Section 3.2.2). The following properties in a model are considered to model dynamic and acoustic properties:

- **Mass and stiffness:** The mass and stiffness of a system determine the eigenfrequency ω_n of a system via the basic Equation (3.1):

$$\omega_n = \sqrt{\frac{\text{stiffness}}{\text{mass}}} \quad (3.1)$$

Equation (3.1) describes the eigenfrequency of a fundamental mass-spring system. In more complex structures, Equation (3.1) has a more complex notation, however, the ratio between the mass and the

stiffness of the system is always included. A more complex system also possesses multiple eigenfrequencies each belonging to their respective mode shape.

The distribution of the mass and stiffness throughout the structure is important, as different modes dynamically activate different parts of the ship. The mass and stiffness distribution thus have a different effect per mode shape depending on the parts of the ship that are translated and the corresponding mass and stiffness.

- **Dimensions and geometry:** The dimensions and geometry of the system influence the mass, the stiffness, and thus the eigenfrequencies and mode shapes.
- **Structural damping:** Vibrations in a structural system do not continue with the same amplitude towards infinity. Instead, multiple mechanisms dissipate the vibration energy by conversion of kinetic energy into heat or movement of the air. Due to these mechanisms, the vibration amplitude decays over time and damping is introduced into the system. The magnitude of the damping affects the amplitude of the response of the system. (In transient calculations the damping also leads to a shift in the phase of the response).

The importance and the level of detail for the described properties depend on the frequencies that are analysed. Higher frequencies result in mode shapes with smaller waves in the structure. Modelling smaller waves requires more structural detail to capture the waves accurately. This effect is explained using Figure 3.1 and Equation (3.2) that describe the eigenfrequencies and mode shapes of a simply supported beam.

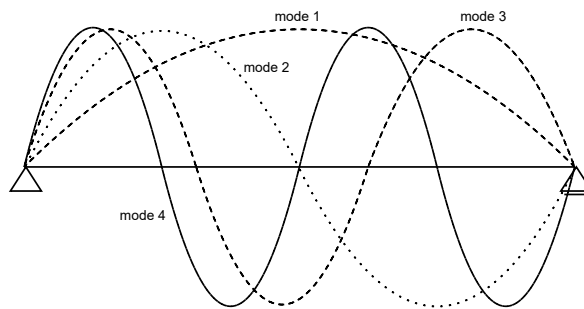


Figure 3.1: The First Four Mode Shapes of a Simply Supported Beam.

$$\omega_n = \frac{(\pi n)^2}{L^2} \sqrt{\frac{EI}{\rho A}} \quad (3.2)$$

Where n is the mode number, L is the length of the beam, EI is the stiffness of the beam and ρA is the mass of the beam (Metrikine & Tsouvalas, 2020). From the equation, it is clear that higher mode numbers and higher frequencies go hand in hand. Looking at Figure 3.1, mode 4 has the highest frequency and corresponds to the smallest wavelength. Smaller wavelengths fit into smaller details of the modelled structure. So, to correctly model mode shape 4, more detail in the structure is needed. Now for a simple beam, this is easily solved by increasing the number of finite elements used in the computation. However, for complex structures such as ships, more structural elements and details need to be added for higher analysis frequencies.

A complex structure has local and global dynamic modes. Global modes mean that the structure in its entirety moves, for example, as portrayed in Figure 3.1. Local modes are modes in which not the entire structure moves but a local part of that structure. A part of the structure finds resonance at that particular frequency and is dynamically activated with an amplitude much greater than the remainder of the structure. Global modes are mainly influenced by large scale properties of the ship and their distributions. Local modes are influenced by local details and the properties of those.

Taking the previous into account the options are explored to simplify a ship model. The available options are listed below, including advantages and disadvantages that arise when implementing the option.

- **Ship segment:** A small slice from a ship is taken for the analysis. The slice only represents a portion of the ship, but contains higher local details. Depending on the thickness of the slice, the model size reduces, the computational time is reduced and the model is easier to work with. Due to the high local detail, higher modes can be described more accurately. However, low-frequency global modes of the ship are not captured since the global geometry is not represented in the model.
- **Double bottom system:** The ship is modelled as its double bottom system. A ship often has a double bottom system delivering more strength to the ship. In addition to this, the double bottom ensures an extra safety layer for water tightness in case of collision. This method reduces the model size and the calculation time significantly. However, the global stiffness behaviour of the ship is indescribable. The behaviour of the floor on a local level is expected to show better results as more detail is implemented on that level.
- **Equivalent Beam:** The ship is modelled as a equivalent beam with appropriate mass and stiffness. The geometry is strongly simplified reducing the number of finite elements needed to describe the problem, thus reducing the computational time. Furthermore, the equivalent beam model is a simple case that is easy to work with and easy to interpret taking the assumptions into account. It is expected that global modes are described but due to the lack of detail local modes are not included properly. Geometric anomalies are expected to affect the mode shapes. Consequently, the URN pattern and directionality are influenced. The name equivalent beam comes from the beam-like shape with properties equivalent to a reference ship. In the modelling, solid elements are used instead of beam elements.
- **Half-cylinder:** A half-cylinder is used to represent the ship. This method is similar to the beam, as the half-cylinder can be seen as a beam as well. The main difference between the beam and the half-cylinder is the geometric shape. The geometry is more complex, but more accurately describes the shape of a ship. The negative effects of the beam method on the mode shapes, the URN pattern and the directionality could be (partly) solved by implementing a half-cylinder to model the ship.
- **Simplifying existing ship model:** An existing FEM model of a ship can be taken as a starting point as it is elaborate and contains a high level of detail. From this model details and elements can be removed that are not required to model the desired effects. The mass and stiffness of the model are altered by the removal of excess elements and thus the global and local modes can be different. The removed elements result in a reduced computational time needed for the calculation. The complex starting point has as a consequence that the model is complex to work with. Furthermore, interpretation of the results could be challenging as the influence of the removed elements is hard to estimate.

The advantages and disadvantages of the aforementioned methods are summarised in trade-off Table 3.1. The best simplification methods are the beam and the half-cylinder. This is due to the fact that the beam and the half-cylinder are expected to have a good balance between decent results and ease of work. The beam is computed to be the best method for the simplified model. Compared to the beam, the cylinder model is expected to be more complex and computationally intense. The results are expected to show improved results due to the enhanced geometry.

Looking at the challenges of modelling the half-cylinder, it is decided to first develop the beam model. The half-cylinder model requires detailed data on the structure of a ship, the girders and the spacing. The choice for the level of detail goes hand in hand with a significant amount of assumptions leading to uncertainties in the results.

Table 3.1: Weighted Trade-Off Table for Method of Simplification.

Method	Computational time	controllable	Interpretation	Model setup	Results accuracy	Local modes	Global modes	Final score
Weight	5	8	9	10	7	6	6	
<i>Ship segment</i>	7	5	6	3	5	9	1	254
<i>Double bottom system</i>	7	8	8	5	4	7	2	303
<i>Beam</i>	8	10	8	9	4	2	7	364
<i>Half-cylinder</i>	7	8	8	5	8	5	8	355
<i>Simplified existing ship model</i>	5	4	6	5	9	9	9	332

3.2. Framework for the Simplified Model

In this section, the framework of the simplified model is explained. The framework defines the conditions in which the model is created and the reference data that was obtained using similar conditions. The necessity for this flows from the fact that output from the simplified model should be obtained in similar conditions to the measurements and models in the papers to allow for proper comparison and verification of the model results.

3.2.1. Reference Case and Validation Data

Reference data to validate the simplified model can be found in (M. Ainslie et al., 2009), discussing the source level spectra of the different RANDI classes, the Wales & Heitmeyer (W&H) model for source level and measurements of the M/V Overseas Harriette (OH) (Arveson & Vendittis, 2000), as explained in Section 2.2. Furthermore, Jansen and de Jong (2017) did measurements of ship source levels close to the Port of Rotterdam and made distinctions between the type of ship, length, speed and deadweight. Lastly, MacGillivray and de Jong (2021) compared the RANDI and W&H models to a new model and indicated possible errors.

A case needs to be chosen in order to set up the simplified model and to compare the results of this model to appropriate data. The reference case needs to contain the following data:

- **Source level spectrum (0 – 200 Hz):** This spectrum is used for comparison of the model data in terms of the shape of the curve and magnitudes.
- **Machinery input spectra (0 – 200 Hz):** Machinery specifications or data that leads to an input spectrum.
- **Ship type:** Ship type that is modelled in the simplified cylindrical case. The simplified model needs correct dimensions and properties to recreate a representative dynamic response.

For this research the RANDI tanker/merchant class and the Wales & Heitmeyer source level model are used, the OH ship at 12 knots shows close resemblance and can be used as a real-world example. The ship used by Zhang et al. (2019) falls into the merchant/tanker class, this is useful since power machinery vibration data is shared. The input spectrum for the machinery in the model can be derived from this. The corresponding spectra of the RANDI classes, the W&H model and the measurements can be seen in Figures 3.2 to 3.4. The simulated URN from the ship used by Zhang et al. (2019) can be found in Figure 3.6, please note the different unit on the y-axis.

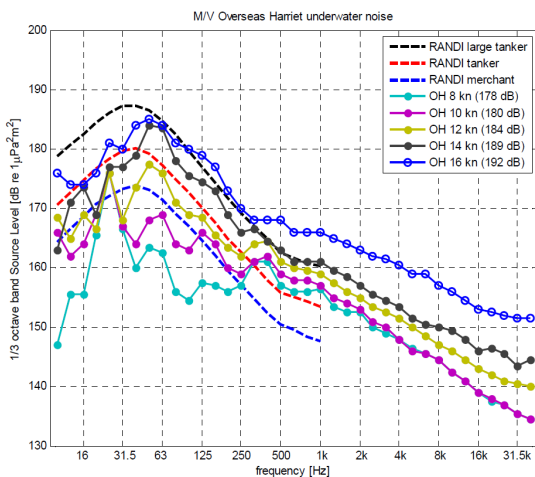


Figure 3.2: The Spectra for Source Levels for 3 RANDI Classes and the OH for Different Speeds. (M. Ainslie et al., 2009)

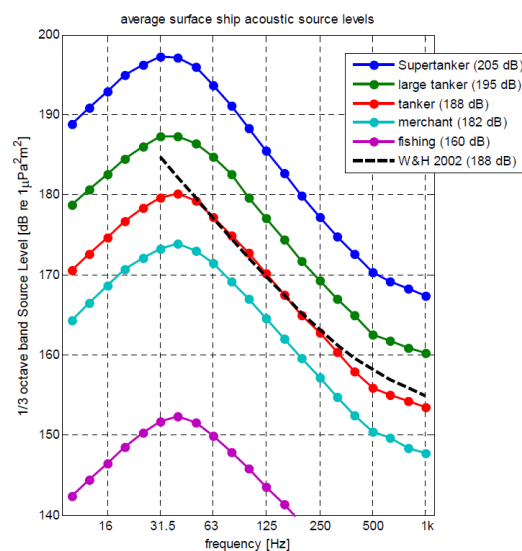


Figure 3.3: The Spectra for Source Levels for the 5 RANDI Classes and the Wales & Heitmeyer model. (M. Ainslie et al., 2009)

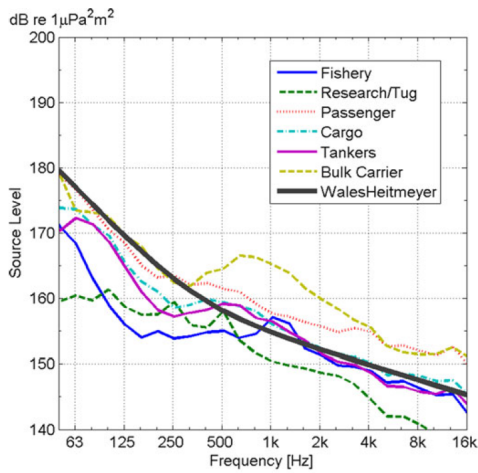


Figure 3.4: The Spectra of the W&H Model and Measurements of Ship Classes Close to the Port of Rotterdam. (Jansen & de Jong, 2017)

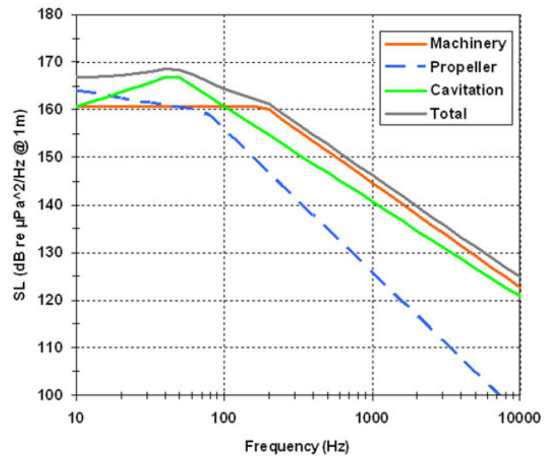


Figure 3.5: Decomposed Source Level Noise Spectrum for a Generic Merchant Ship at 15 knots. (Audoly et al., 2017)

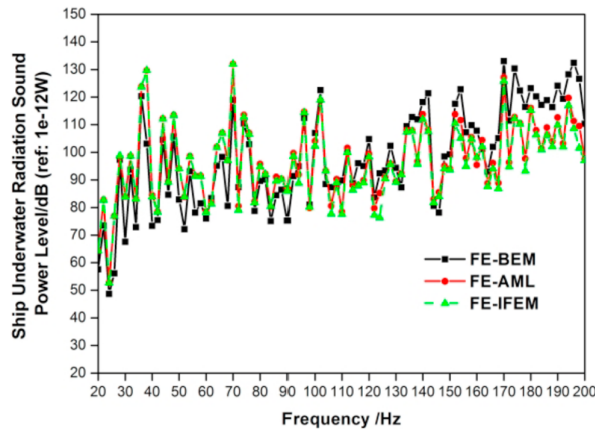


Figure 3.6: Simulated URN of the Merchant/Tanker Class Ship Analysed by Zhang et al. (2019).

Figures 3.2 and 3.3 portray the total source level of a ship taking into account all noise-producing factors from a ship. In this research, only noise produced by the machinery is looked at. The Wales & Heitmeyer spectrum can be computed for a speed of 0 m/s by omitting the velocity term from the equation. However, the accuracy and reliability of the resulting spectrum are unclear since the authors are not clear about the applicable velocity range of the model. In another paper, Audoly et al. (2017) shows the source level spectrum of a generic merchant ship at 15 knots decomposed in the different ship noise generation processes, see Figure 3.5. The figure shows that for all three different generation processes the noise levels are in the same order of magnitude in terms of decibels. The total source level combining all three processes is slightly higher due to the logarithmic relation between sound pressure and decibel level. Figure 3.5 indicates that the source level graphs of Figures 3.2 and 3.3 can still be used to verify the noise from the model as the source level and its frequency dependence are not greatly different for the machinery only compared to the total noise.

Data from the RANDI model is based on old measurements from World War 2 that are not available anymore and rests on assumptions that are outdated. Furthermore, it lacks statistical uncertainty ranges that make interpretation of the accuracy of the model difficult. The W&H model has no speed dependence and used a small sample size for deriving the model. A small sample size troubles the confirmation of the model's applicability to other ships. A recent study performed by (MacGillivray & de Jong, 2021) compared the RANDI and W&H models to a large data set (ECHO) obtained in 2017 consisting of 1862 ships, the results are shown in Figures 3.7 and 3.8. It can be seen that the models on average overestimate the actual source level of the ship in the range of 10 – 200 Hz. At maximum the average residual error can be over 10 dB and should be

taken into account during the comparison of the results of this research with the reference data. The band around the solid lines represent the standard deviation around the mean.

Moreover, MacGillivray and de Jong (2021) computed the average source level spectra of the ECHO data set and compared it to the models and a new model derived from the ECHO data set. In Figure 3.8 the results can be seen and it is clear that the RANDI and W&H models overestimate the source levels up to 200 Hz.

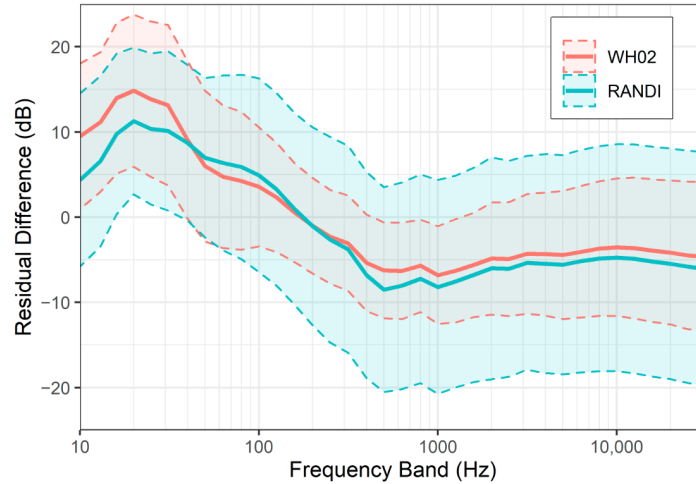


Figure 3.7: Mean Residual Errors of the Randi and W&H Models Compared to Recent Data From 2017. (MacGillivray & de Jong, 2021)

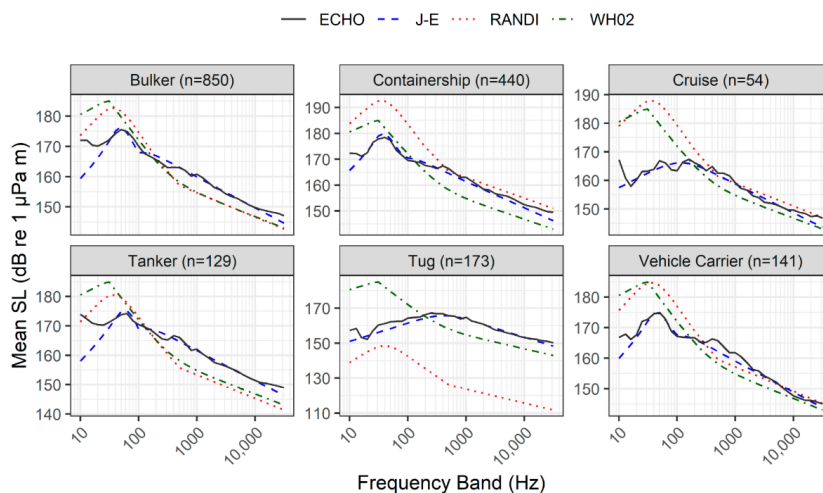


Figure 3.8: Comparison of the Mean Source Level Spectra of the ECHO Data Set, RANDI and W&H Models, and the New Model Created by MacGillivray and de Jong (2021).

Due to the logarithmic relation between the sound pressure and the decibel level (see Equation (3.4)), the differences in terms of decibels seem minor but could be substantial in terms of sound pressure. An increase of the sound pressure by a factor of 2 only increases the decibel level by 6 dB. Another interesting feature of this relation becomes clear with the summation of two sound signals. In Table 3.2 two sound signals of different levels are combined, the machinery could be the 160 dB signal and cavitation could be the 170 dB signal (compliant with Figure 3.5, exaggerated). The combined decibel level of the two signals is only 172.4 dB, being only slightly higher than the original loudest signal of 170 dB. Now, when the sound pressure of the 160 dB signal is reduced by 50%, the total combined level is 171.3 dB. So, for a decrease of 50% of the 160 dB signal, the total dB level is reduced by 1.1 dB.

This example shows that if one signal is louder than the other signal, a decrease of that softer signal results in a minor decrease in the total decibel level. It is thus evident that attenuation of the loudest signal is most effective in reducing the combined sound level.

However, it should be realised that Figure 3.5 concerns a situation where the ship has a cruising speed of 15 knots. It is expected that for lower cruising speeds the relative contribution of the machinery noise increases and that of the other components decreases, as can be concluded from the model formulations used for Figure 3.5 by AQUO (2015). Attenuation of the machinery noise could thus just be as effective as attenuation of the cavitation noise in reducing the combined URN of the ship. In reality, attenuation of all components is needed to achieve a quieter ship throughout all operating conditions and noise frequencies.

Table 3.2: The Combination of Two Sound Signals of Different Decibel Levels, Including the Reduction of One Signal.

	dB level	SPL [Pa]	Reduction	Reduced dB level	Reduced SPL [Pa]
	160	100	50%	154	50
	170	316	100%	170	316
Combined SPL		416			366
Combined dB	172.4			171.3	

3.2.2. Analysis Frequency Range

The frequency range for the analysis of the underwater radiated noise is 20 – 200 Hz. The range follows from the following factors and reasoning, sorted by importance first.

- **Marine mammals:** Lower frequencies travel further and attenuate slower than higher frequencies. Because of these two characteristics, there is an ambient noise field present in all parts of the oceans. A significant portion of this low-frequency ambient noise is caused by ships, as could be seen in Figure 1.1. This figure makes clear that within a frequency range of approximately 10 – 300 Hz ambient shipping noise is present.
- **Modelling accuracy:** When modelling waves, enough elements should be used to accurately capture the waves and the vibrations of the structure. Higher frequencies come with a decreased wavelength and thus more computational elements are required. Furthermore, additional detail in the CAD model is needed as the smaller waves are influenced more by those details. The tipping point for the frequency where it becomes challenging to obtain accurate results is found in various papers during the literature study (see Chapter 1) to be around 200 Hz.
- **Domain size:** The domain size is coupled to the wavelength of the acoustic waves. There are requirements for the domain size to accurately capture the waves (explained in Section 3.3.4). For a wave frequency that goes towards zero, the wave length and required domain size go towards infinity. 20 Hz is chosen as the lower frequency analysis bound, such that a balance is found between the desired lower bound (0 Hz) and the computational limits.
- **Computational time:** An increase in detail, smaller elements and a larger domain result in an increase in the total amounts of nodes and elements in the model. naturally, the total computational time to solve the model increases with a higher number of elements. Thus, the point where accurate results are obtained with the smallest amount of elements is the ideal model setup.

3.2.3. Type of Machinery and Input Spectra

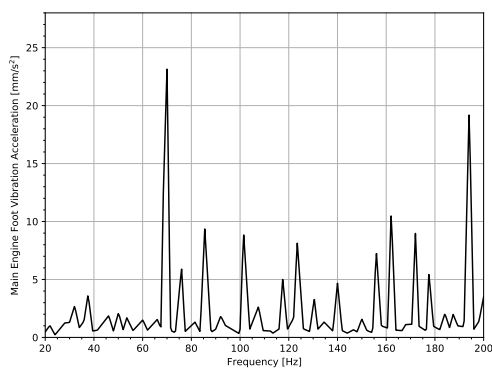
The type of machinery is the main engine, the gearbox and the diesel generator unit. The type of machinery used should belong to the tanker or merchant ship class as determined in Section 3.2.1. The vertical vibration and exertion of force from the machinery on the hull of the ship is looked at as this type of motion excites the hull with the largest magnitude compared to other load directions. Rotational movement and horizontal translations are not taken into account as those either do not excite the ship's hull significantly, are challenging to model, or are not found in measurements in the literature.

Zhang et al. (2019) provided machinery foot acceleration data measured on the ship belonging to the merchant class in terms of length. The ship's velocity during the measurements is not defined in the paper as well as the exact construction and mounting of the machinery to the hull. The ship's propulsion system uses a Daihatsu Diesel engine of which the specifications and characteristics can be found in Table 3.3. The

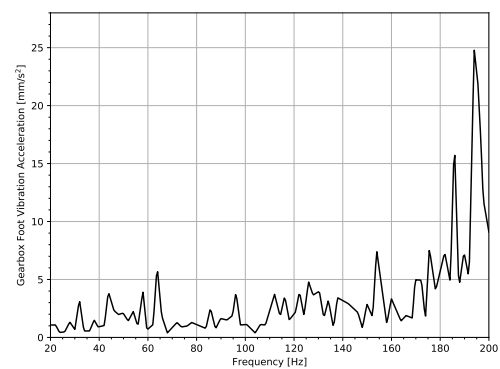
accelerations at the foot of the individual types of machinery have been measured over a frequency range of 20 – 200 Hz and can be found in Figures 3.9a to 3.9c. Together with the mass of the machinery and Newton's second law ($F = ma$) the force exerted by the machinery on the ship's structure can be derived, which is presented in Figure 3.9d. The mass of the gearbox is not given and is thus assumed to be not of influence on the total force exerted by the machinery.

Table 3.3: Machinery Specifications. (Daihatsu Diesel, 2021; Zhang et al., 2019)

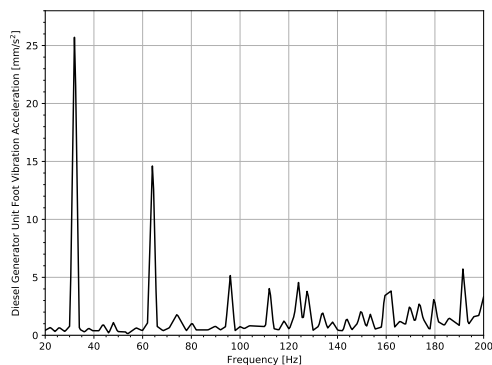
Specification	Engine	Diesel Generator Unit
Type	6DKM-26 Daihatsu Diesel	Generator (DKBH4320/06) & Diesel engine (R6160ZC)
Power output	1618 kW	720 kW
Rotation speed	750 r/min	1000 r/min
Mass	18,0 ton	2,84 ton



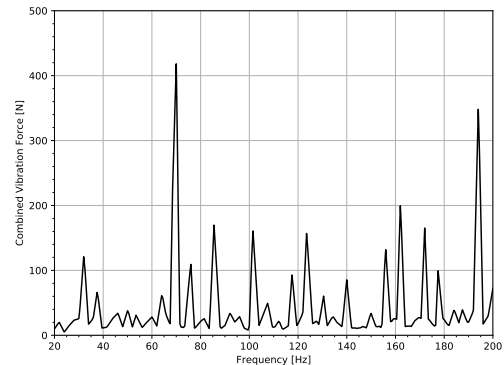
(a) Main Engine Foot Accelerations



(b) Gearbox Foot Accelerations



(c) Diesel Generator Unit Foot Accelerations



(d) Combined Machinery Force Input Spectrum

Figure 3.9: The Machinery Acceleration Data and the Combined Force Input Spectrum. (Zhang et al., 2019)

3.2.4. Operating Conditions

The operating conditions of the ship are assumed to stay constant throughout the analysis. A change in operating speed, draught, rotation or any other characteristic that influences the results from the analysis is not looked at. These changes affect the URN of a ship, however, those effects are out of the scope of this research and should thus be limited.

The operating conditions for the simplified ship model that should be specified are the cruising speed and the draught. The cruising speed is jointly defined via the force input spectrum, however, Zhang et al. (2019)

did not define the corresponding cruising speed to the force spectrum of Figure 3.9. The draught chosen is 7.9 m to resemble similar values of the OH ship during the measurements.

3.2.5. Boundary Conditions

The bathymetry, the fluid flow speed and the waves influence the noise pattern in the water. However, the source level of the ship is a measure of the URN that is by definition independent of such environmental influences (de Jong, 2009). The source level acoustic metric is described in more detail in Section 3.2.6. The ship does have a cruising speed, but no fluid flow around the hull is assumed. The cruising speed only influences the intensity of the machinery vibrations.

3.2.6. Acoustic Metric

A similar acoustic metric for the model results and the reference data is needed to allow for an accurate comparison. The URN is expressed as the source level SL of the ship. The source level is defined as the level relative to $1 \mu\text{Pa}^2$ at a 1 m distance from the acoustic centre of the ship. The acoustic centre is a point in space somewhere within the ship from where the far-field noise seems to be radiated from. The source level is calculated from the far-field radiated sound pressure in order to minimize the effect of the near-field and to allow the sound waves to fully develop. The source level SL is mathematically described by:

$$SL = SPL(r) + 20 \log_{10} \left(\frac{r}{r_{ref}} \right) \quad [\text{dB re } 1 \mu\text{Pa}^2 \text{m}^2] \quad (3.3)$$

Where SPL is the sound pressure level at distance r from the source and r_{ref} is the reference distance of 1 m. The sound pressure level SPL is defined by:

$$SPL(r) = 10 \log_{10} \left(\frac{p_{rms}^2(r)}{p_{ref}^2} \right) \quad [\text{dB re } 1 \mu\text{Pa}^2] \quad (3.4)$$

Where p_{rms} is the root mean square sound pressure and p_{ref} is the reference sound pressure of $1 \mu\text{Pa}$. (de Jong, 2009)

In Equation (3.3) the viscous damping of the fluid is not included. The acoustic metric for this research is the source level, on which the viscous damping shows no effect. The viscous damping attenuates the acoustic pressure with large distances and is frequency dependent. In the models, the fluid viscosity is set to zero to eliminate this effect, and thus this effect should not be included in Equation (3.3). The source level is therefore determined by computation of the far-field underwater radiated sound pressure of a ship and calculation of the source level using Equations (3.3) and (3.4).

Due to complex noise radiation patterns, wave interference and other processes, the radiated noise magnitude is different in all directions. The source level is a source property that also has a directional component. This means that the source level is dependent on the direction of radiation and can be different in different directions. In real ship source level measurements, the average source level over a range of angles is taken. The SL is measured at a fixed position whilst a ship passes. This has been done by (Jansen & de Jong, 2017).

The source level in this research is expressed as the average source level over the directions in which the order of magnitudes is similar. In Section 3.6 this is further elaborated upon after the directionality results have been presented and the angles to average can be determined.

3.3. Equivalent Beam Model

An equivalent beam (EB) model was set up to approximate a reference ship. The beam was configured to have the same global properties in terms of mass, stiffness and dimensions. A reference ship was chosen such that the model results can be verified against the reference models and classes presented in Section 3.2.1. The ship that is mimicked is the Giant 5 Barge of Boskalis, of which the CAD model is provided by Nevesbu. The barge does not have propulsion machinery, this data was taken from Zhang et al. (2019), as the ship class and properties are moderately similar. The ship can be seen in Figure 3.10.



Figure 3.10: The Giant 5 Barge Owned by Boskalis.

3.3.1. Model Shape and Dimensions

The dimensions of the ship can be found in Table 3.4. Because the general shape of the barge shows a good resemblance with a beam, the dimensions for the beam are kept the same.

Table 3.4: Dimension of the Giant 5 Barge.

Dimension	Magnitude
Length L	137 m
Width B	36 m
Depth d	8,5 m
Design draught D	6,45 m

The beam was modelled in Ansys using 3D solid elements (see Section 3.3.6). Although the name (Equivalent Beam) might suggest a 1D beam model such as the Euler-Bernoulli beam model or the Timoshenko beam model, this name was chosen here because a 3D solid is modelled shaped as a beam with the equivalent properties of the reference ship.

3.3.2. Materials and Properties

The material assigned to the beam is fictitious and is derived from the global properties of the Giant 5 Barge from Boskalis. A FEM model is available from which the mass and stiffness of the ship and the beam can be derived. The total mass of the Giant 5 Barge is $8,5656 \cdot 10^6$ kg. The stiffness was determined by performing a static analysis and simply supporting the ship as a beam. A known load was applied to the midpoint of the ship and the corresponding deflection was calculated, see Figure 3.11. With Equation (3.5) corresponding to Figure 3.12, the stiffness (EI) of the ship was calculated to be $1,585 \cdot 10^{13}$ Nm². From the stiffness and the dimensions of the beam, the Young Modulus $E_{eq,beam}$ is $8,604 \cdot 10^9$ N/m². Furthermore, the Poisson ratio of the equivalent beam is set to 0, as the ship is not solid and compression of an outer surface would not result in an expansion in a different direction.

The density of the beam was obtained by dividing the total mass of the FEM model by the volume of the equivalent beam. Resulting in a density $\rho_{eq,beam}$ of 204,32 kg/m³.

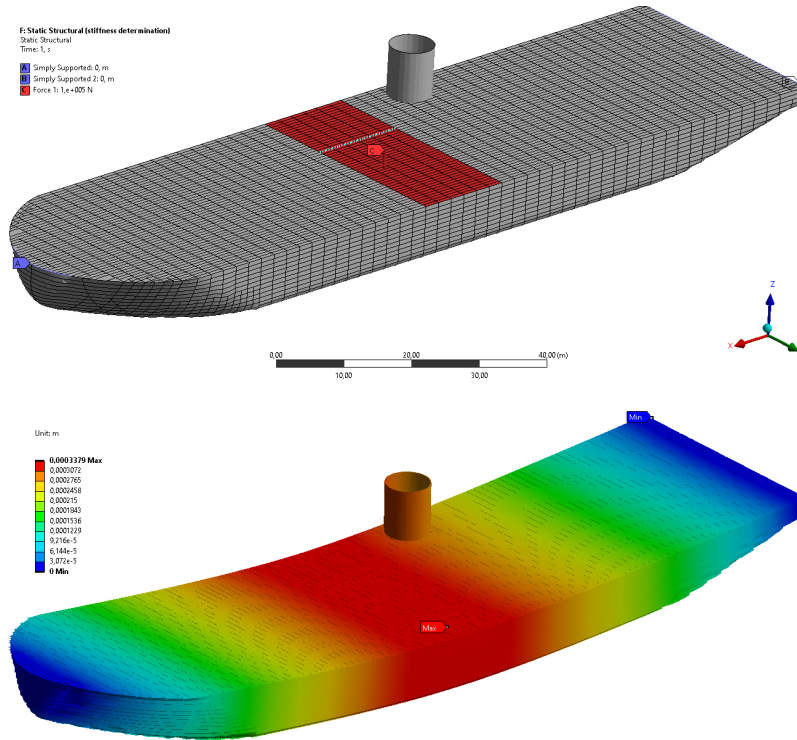


Figure 3.11: FEM Model of the Giant 5 Barge from Boskalis provided by Nevesbu Modelled as a Simply Supported Beam (TOP). Results of the Simply Supported Beam Static Analysis (BOTTOM).

$$w = \frac{Fl^3}{48EI} \quad (3.5)$$

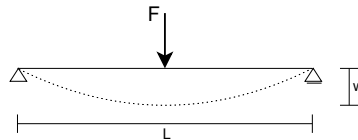


Figure 3.12: Deflection of a Simply Supported Beam Subjected to a Point Load.

For the acoustic fluid domain, the properties of seawater at 20 degrees Celsius are taken. The density is 1025 kg/m^3 and the speed of sound is 1522 m/s .

Damping

Damping in the system is caused by multiple processes and has to be implemented in the model. The two most prominent damping processes are structural damping and acoustic radiation damping. Damping due to fluid surface waves is neglected. The acoustic vibrations of the ship hull are expected not to show large wave formations in the fluid as the amplitudes of the acoustic vibrations are small.

Structural damping can be modelled using Rayleigh damping or a constant structural damping coefficient (hysteretic damping) within Ansys 2021R2. Rayleigh damping utilises two input values α and β to describe the system damping as a function of the frequency. α influences the magnitude of the damping coefficient mainly at the low frequencies and β influences the magnitude of the damping coefficient mainly at the higher frequencies.

The acoustic radiation damping is implemented in the model using Perfectly Matched Layers (PML) on the outside of the computational domain, see Section 3.3.4.

Frequency-dependent viscous damping as a function of distance from the source is not taken into account as the acoustic metric is the source level. In the calculation of the source level the frequency-dependent propagation can also be omitted, saving time and preventing possible calculation errors. The viscous damping is eliminated from the model by setting the fluid viscosity to 0. Since there is no flow in the model, setting the viscosity to 0 has no other undesired effects on the results of the model.

In Ansys the structural damping matrix is derived as follows:

$$[C] = \alpha [M] + \left(\beta + \frac{g}{\Omega} \right) [K] + \dots \quad \text{material dependent terms} \quad (3.6)$$

Where $[M]$, $[C]$ and $[K]$ are respectively the mass, damping and stiffness matrices, α and β are the Rayleigh damping constants, g is the constant structural damping coefficient and Ω is the excitation circular frequency. The extra material-dependent terms are left out of this formulation for clarity, the full damping matrix can be found in Appendix A.

Damping is a property that is difficult to predict beforehand and oftentimes this is calculated from time-series data from measurements. For the modelling of the EB model, no reference time-series measurements are available, meaning that the required model damping should be estimated. Rayleigh damping combined with the range of frequencies in this research leads to large over- and/or underestimations of the damping due to the non-linear relation with the frequency. It is opted for a constant structural damping coefficient of 0,02 as this is confirmed by sources for welded steel structures (Kudu, Uçak, Osmancikli, Türker, & Bayraktar, 2015).

3.3.3. Equivalent Beam Dynamics Behaviour Check/Range of Applicability

A comparison between the dynamic behaviour of the equivalent beam and the Giant 5 Barge is made to see how accurate the beam describes the barge in terms of dynamics. Table 3.5 shows the comparison of the identified eigenfrequencies for both models for the same mode during a dry and free modal analysis. A dry free modal analysis has no fluid domain or added mass and no supports. Higher frequency modes are not identified as the Giant 5 Barge model is not suitable for this. Local element resonances were identified by Ansys as a mode and those modes troubled the data.

Table 3.5: Comparison of Modes and Eigenfrequencies of the Giant 5 Barge and the Equivalent Beam.

Mode nr.	Type	Barge freq. [Hz]	EB freq. [Hz]	Tuned EB freq. [Hz]
1	Bending 1	2.52	2.98	2.52
2	Torsion 1	3.52	7.14	6.02
3	Bending 2	6.10	8.05	6.79
4	Torsion 2	7.11	14.51	12.23
5	Bending 3	10.01	15.34	12.93
6	Torsion 3	10.60	22.31	18.81
7	Bending 4	13.52	24.48	20.64
8	Torsion 4	14.68	30.74	25.92
9	Lat. bending 1	16.05	37.73	31.81
10	Bending 5	<i>Not Identified</i>	35.14	29.63
11	Torsion 5	18.78	39.98	33.71

From Table 3.5 can be concluded that the frequencies of the EB model are significantly higher than the Giant 5 Barge for all identified modes and the absolute and relative difference increases for higher frequencies.

The eigenfrequencies of the EB model can be tuned by adjustment of the mass and stiffness of the beam. However, being a prismatic beam, matching all modes is unrealistic. Adjusting the stiffness of the beam influences the eigenfrequencies, but also influences the deformation magnitudes in static cases. It is thought that this further influences the sound radiation properties of the beam. Adjustment of the mass does not have such effect and thus this method is more appropriate to match the eigenfrequencies in this case. The density of the EB model is adjusted such that the first eigenfrequency corresponding to the first bending mode match

with the barge. The required adjustment is easily calculated using Equation (3.1) and the new density is 287.4 kg/m^3 .

As can be seen from the tuned eigenfrequencies in Table 3.5, after tuning the first eigenfrequencies match. The higher frequencies are reduced and closer to the frequencies of the barge, however, still not comparable. Tuning the beam to other modes shows similar results.

A possible explanation for this could be the non-prismatic characteristic of the ship. For the EB beam, the mass and stiffness along the beam are kept constant in contrast to the barge where this varies. Different modes have different mode shapes in which parts of the structure move more than other parts. With bending modes, the full cross-section of the ship is displaced. With torsional modes, the ship's middle line does not displace and the port and starboard sides have the greatest displacement. The mass on the sides of the ship potentially participates in torsional more than in bending modes. The mass in the middle line of the ship participates more in the bending modes of the ship. This works the same with the stiffness of the ship. It is because of this mass and stiffness distribution and the combination with the mode shapes that the frequencies of the EB beam and the Barge model do not match.

Furthermore, the open spaces within the ship compared to the solid beam have a probable influence on this. The solid structure behaves differently due to shear within the structure during bending.

Although it is clear that a perfect match in terms of modes and eigenfrequencies seems unrealistic, it does not mean that the model is useless. The graphs presented in Section 3.2.1 show no clear peaks from eigenfrequency resonance and the spectra are more smoothed out. It is possible that the EB model in terms of URN spectra shows results that are in accordance with this, as most types of ships are in the same range.

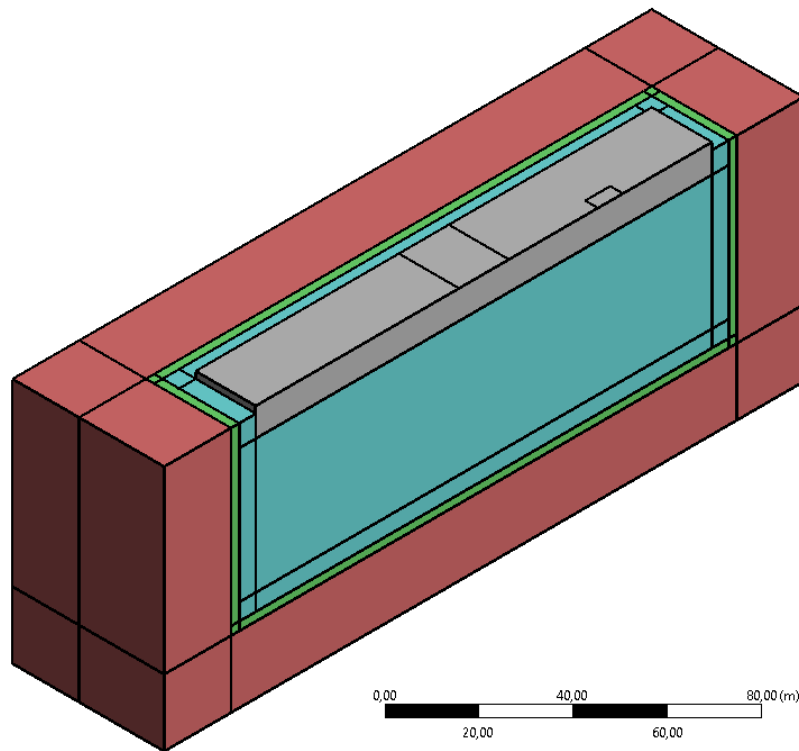


Figure 3.13: Half-Space Model Used for the FEM Simulations. Grey: EB, Blue: Acoustic Domain, Green: Buffer Layer, Red: PML region.

3.3.4. Fluid Domain

The equivalent beam is surrounded by an acoustic fluid domain representing the ocean. The acoustic fluid domain is modelled to be infinite in all directions to minimize the effect of physical boundaries on the radiated noise pattern. The surface of the acoustic fluid domain is modelled as a free surface.

Although literature (see Section 1.2) has pointed out that the BEM is the most promising method to model the infinite acoustic fluid domain in terms of calculation speed and accuracy, this technique is not available in the software used in this research. In Ansys 2021 R2 there are three possibilities for modelling the infinite

acoustic fluid domain according to Howard and Cazzolato (2015). The first technique makes use of Perfectly Matched Layers (PML) that are used to absorb the incident acoustic waves and to prevent waves from reflecting back into the acoustic domain. The PML is located in the PML region on the outside of the acoustic fluid domain and has a certain thickness depending on the wavelength of the acoustic waves.

The second technique makes use of radiation boundaries that are applied to the outer surface of the acoustic domain. The radiation boundary imposes a Robin boundary condition on the applied faces, also called an impedance boundary condition. This boundary condition requires incident waves to be normal to the radiation boundary and plane wave conditions to exist to accomplish optimal absorption of the acoustic waves.

The third technique utilises infinite acoustic elements to model the boundaries of the model. The infinite acoustic elements are applied to the outer face of the acoustic region where the Sommerfeld radiation condition is satisfied. This condition implies that acoustic waves propagating outwards of the domain do not propagate inwards. The infinite acoustic elements need to be applied to the outer face of a spherical acoustic region with a constant radius. (Howard & Cazzolato, 2015)

The three methods of modelling infinite fluid available in Ansys 2021 R2 have different fields of application. For the problem at hand, radiation boundaries are not applicable, since this requires plane waves that propagate in normal direction relative to the boundary. The acoustic radiation of the equivalent beam is a 3D problem with radiation in all directions and does not satisfy the two requirements for radiation boundaries.

Infinite acoustic elements require a spherical fluid domain and spherical spreading of the acoustic pressure waves. It is expected that the equivalent beam mainly radiates noise in the downwards direction. The sides of the beam are not dynamically activated when the beam is excited in the vertical direction. Furthermore, a spherical acoustic domain would lead to large domain sizes in all direction which would increase the total amount of computational elements significantly.

Perfectly Matched Layers are used to model the infinite acoustic fluid domain around the equivalent beam. The build-up of the infinite acoustic fluid domain can be seen in Figure 3.13. The acoustic domain in outwards directions consists of the acoustic fluid domain, a buffer layer and the PML region. A radiation boundary is located on the face between the acoustic domain and the buffer layer for the computation of the far-field characteristics. The buffer layer is applied to avoid the effects of the PML region on the radiation boundary. The PML region dissipates the pressure waves and minimises the reflection back into the acoustic domain.

The domain was modelled as a half-space, meaning that the model is divided in half and symmetry conditions are imposed on the symmetry plane. This technique is used to roughly halve the number of elements and speed up the computation time. The implications of using symmetry conditions is that certain modes (e.g. torsion) of the equivalent beam cannot occur.

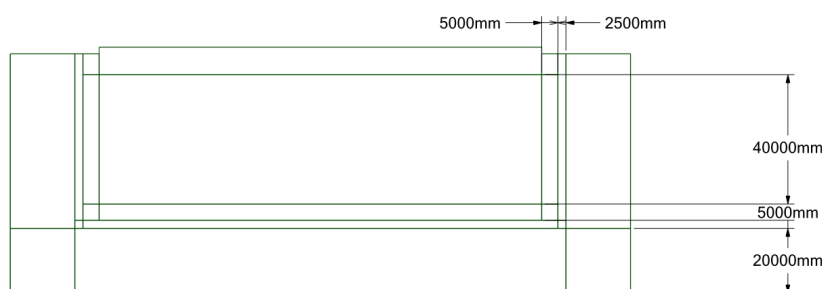


Figure 3.14: Dimensions of the Fluid Domain.

The size and element requirements for the different layers of the acoustic domain can be found in Table 3.6.

The size of the layers and acoustic fluid domain and the element size depends on the frequencies that are modelled. Looking at Table 3.6, it can be seen that the total size of the acoustic domain should be larger than $\frac{3}{4}$ of the largest wavelength. This requirement naturally imposes a limit to the lower frequency bound that can be analysed. A lower bound towards 0 Hz leads to an infinite size for the domain and is impossible.

Table 3.6: Requirements for the Different Layers Within the Infinite Acoustic Fluid Domain. (Howard & Cazzolato, 2015)

Layer	Size	No. of elements
Acoustic body	$\geq \frac{1}{2}$ largest wavelength	-
Buffer layer	-	3-4
PML region	$\geq \frac{1}{4}$ largest wavelength	3-4

To avoid a substantial fluid domain that leads to a long calculation time and a large solution file size, the lower analysis frequency bound is set to 20 Hz. This is also in accordance with Figure 1.1. The resulting largest wavelength thus occurs at the frequency of 20 Hz and can be computed using Equation (2.9):

$$\lambda = \frac{c}{f} = \frac{1522}{20} \approx 75 \text{ m}$$

The resulting layer thickness of the acoustic body (A_t), buffer layer (B_t) and PML region (P_t) are computed as follows:

$$A_t = \frac{75}{2} = 37,5 \rightarrow 40 \text{ m}$$

$$B_t = 2,5 \text{ m}, \quad 4 \text{ elements, see Section 3.3.6 for element size}$$

$$P_t = \frac{75}{4} = 18,75 \text{ m} \rightarrow 20 \text{ m}$$

The layer thicknesses are rounded up to the nearest tenfold to assure the layer thickness is sufficient and to allow for easier fitting of the element size within the layer. A schematic including the final dimensions of the fluid domain is found in Figure 3.14. An additional layer of 5 meter thickness is added underneath the acoustic body to be able to satisfy the mesh elements sizes explained in Section 3.3.6. Without this extra layer the mesh size would increase around the radiation boundary decreasing the accuracy of the far-field data.

In the horizontal directions the domain size and layer thicknesses are reduced to save computational time. Due to the vertical input, the expectation is that no significant noise emission occurs in the horizontal direction and the main noise emission occurs in the vertical downwards direction. Furthermore, the machinery has no eccentricity from the centre line of the ship so no modes are activated that result in a sideways emission of noise.

3.3.5. Boundary Conditions and Model Inputs

The boundary and interface conditions that are imposed on the model are:

- **Pressure:** A pressure boundary condition of 0 Pa is applied to the outside face of the PML region, as is required by the software and the modelling technique.
- **Radiation boundary:** A radiation boundary condition is applied to the outside faces of the acoustic fluid body on the boundary with the buffer layer. This boundary condition defines the source surface for radiation to the far-field domain. This technique is taken from Howard and Cazzolato (2015).
- **Fluid structure interface:** To couple the fluid and the structure, a fluid-structure interface is defined on the boundary between the equivalent beam and the acoustic body surrounding the beam. On this interface, coupling conditions are imposed that match the pressure and the displacement of the fluid and the structure. The coupled equations given in Section 2.7 are solved on this interface.
- **Symmetry plane (fluid):** A symmetry plane boundary condition is applied to the section surface created by dividing the total model in half. The symmetry planes have pressure gradients of zero perpendicular to the plane and thus the results can be mirrored.
- **Symmetry (structural):** Displacements gradients of zero in the beam are required in the lateral direction to properly introduce the half-space with symmetry in the structural domain of the model. This is implemented using a displacement constraint ($u_x = 0$) in lateral direction.

The input applied to the model is the combined machinery force spectrum as seen in Figure 3.9d. For a linear system, it is more efficient to multiply the model response spectrum to a unit force with the actual force spectrum. Because this is only half of the full space model, the unit response should be corrected with a factor of $\frac{1}{2}$. The place of application of the input and other boundary conditions can be seen in Figure 3.15. The input location is arbitrarily chosen at $\frac{3}{4}$ towards the rear end of the beam and the input is applied directly to the EB model. The force is evenly spread out over the application location. The exact machinery location and connection properties are not specified by Zhang et al. (2019).

In Figure 3.15 some boundary conditions overlap making the diagram unclear. To clarify, the right-front face of the model is completely a symmetry plane and the far-field radiation surface (B) is on the bottom side of the inside surface body (C).

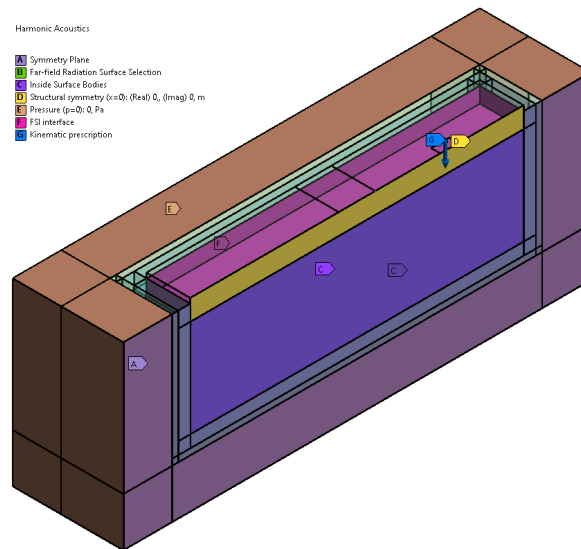


Figure 3.15: Boundary Conditions Imposed on the EB Model.

3.3.6. Mesh and elements

The element size is dependent on the smallest wavelength in the analysis corresponding to the upper analysis frequency bound of 200 Hz. Because the wave speed in the equivalent beam and the fluid differs, both domains have different required maximum element sizes. The elements per wavelength (EPW) ratio should be at least 12 for linear elements and 6 for quadratic elements. (Howard & Cazzolato, 2015)

In this model, quadratic elements are used because significantly fewer elements are present in the total model. The number of DOFs per element is increased, however, it is expected that the total computational time is shorter for quadratic elements compared to linear elements. An explanation on linear and quadratic elements is given in Section 2.4.1.

The element size e_{fluid} can now be computed using:

$$e_{\text{fluid}} = \frac{c}{f \cdot \text{epw}} = \frac{1522}{200 \cdot 6} = 1,27 \text{ m}$$

This requirement is applicable to the acoustic body.

For the buffer layer and PML region, there are different requirements as explained in Section 3.3.4. The buffer layer and the PML region should have a thickness of at least 3-4 elements. The function of the buffer layer is to minimize the effect of the PML region on the acoustic domain and the far-field radiation boundary. Because of the extra 20 meter layer below the acoustic body, the buffer layer does not need to fulfil the requirements as the requirement is already met by the extra layer.

For the EB structure, a required minimum element size of 2,1 m is found. This value is derived using Figure 3.1 and Equation (3.2) in combination with the frequency of 200 Hz and the beam properties. The

maximum mode number n_{max} is found from which the wavelength and thus the element size follows. Figure 3.16 shows the dependence of the element size on the upper frequency analysis bound.

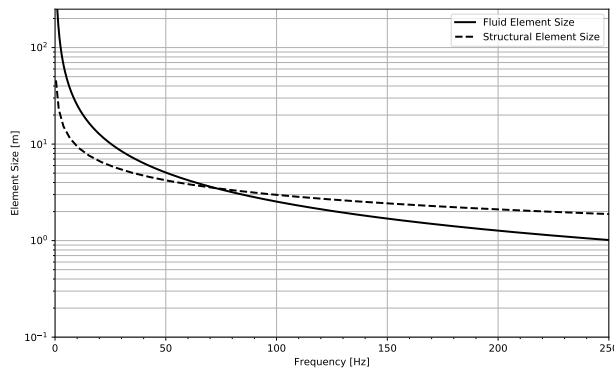


Figure 3.16: Acoustic Fluid and Structural Element Size Requirement Versus Frequency.

The types of elements used in the mesh are:

- **FLUID220/221:** A higher-order quadratic acoustic fluid element consisting of 20 nodes for the cubic option (FLUID220) and consisting of 10 nodes for the pyramid option (FLUID221). Used to model the acoustic fluid domain, the buffer layer, and the PML region. Blue, green and red regions in Figure 3.17.
- **SOLID186/187:** A higher-order quadratic structural element consisting of 20 nodes for the cubic option (SOLID186) and consisting of 10 nodes for the pyramid option (SOLID187). Used to model the equivalent beam. Grey region in Figure 3.17.
- **SURF154:** A higher-order surface 8-node element used on the fluid-structure interface between the equivalent beam and the acoustic fluid domain. Various quantities are brought together in this element and interface conditions are maintained. The interface between the grey and blue region in Figure 3.17.

The mesh of the model can be seen in Figure 3.17.

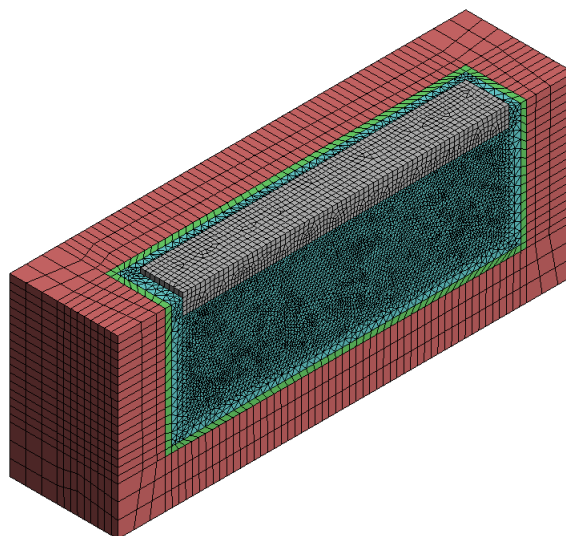


Figure 3.17: Mesh of the EB Model.

3.4. Resilient Mount Application in EB Model

This section explains how the resilient mount is applied to the EB model and how the parameters are varied to analyse the influence of mount parameter tuning on the underwater radiated noise.

3.4.1. Schematisation of the Resilient Mount

The 2D schematic in Figure 2.4 is an extensive model to describe the dynamics of the machinery, the resilient mount and its foundation structure. Simplifications to this model need to be made in order to model the resilient mounts with the available data from the reference case. Reasons for this are that only vertical vibration information is known and no specifications of the foundation beam and underlying structure are provided. Furthermore, the dimensions and the excitation locations within the machinery itself are unknown. Below all the simplifications are listed accompanied by an explanation.

- **Only vertical movement of machinery:** Only vertical acceleration is available in the literature and the force attachment location and detailed specifications of the machinery are not available. Horizontal movements and rotations in all directions are thus hard to model and to predict.
- **Foundation schematisation:** No specifications concerning the foundation and its elements were provided in the literature. The foundation beam is assumed to be massless and to equally distribute the load to the underlying structure on the application face. This accommodates proper spreading of the point force from the spring-damper unit to the ship hull structure.
- **Foundation beam and hull structure characteristics in EB model:** The dynamic response of the foundation beam and the ship hull structure are represented by the EB model. In the original EB model, the structure and the response of the ship should already have been accounted for.

After applying the simplifications, the resilient mount is schematised as seen in Figure 3.18. In theory, the schematised model is a combined system with a vertical displacement u_M of the machinery and a vertical displacement $u_{EB}(x)$ of the equivalent beam. The vertical displacement $u_{EB}(x)$ is influenced by the response of the EB model and the interaction with the fluid.

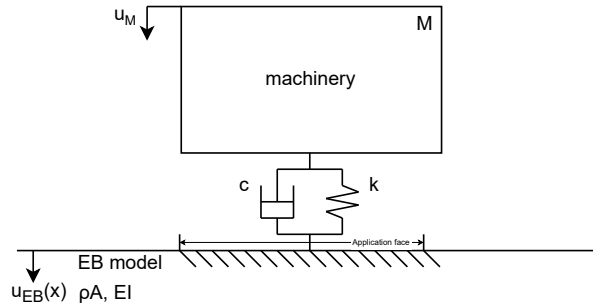


Figure 3.18: Schematisation of Resilient Mount System Applied to the Machinery of the EB Model.

3.4.2. Mathematical Formulation and Parameter Influence

A reduced analytical formulation can be derived for part of the model as seen in Figure 3.18. The equations for the full model are more extensive and challenging to do by hand. In this section, a part of the model is described analytically in order to make a qualitative judgement on the mount parameters c and k and how the system is expected to respond to a change in those parameters. The part of the model that is analysed here is the transfer of the machinery input accelerations to the EB accelerations. This is just a part of the total URN computation, however, higher accelerations lead to more URN.

The starting point is the EOM for the machinery mass:

$$M\ddot{u}_M = c(\dot{u}_{EB}(x) - \dot{u}_M) + k(u_{EB}(x) - u_M) \quad (3.7)$$

$$M\ddot{u}_M + c(\dot{u}_M - \dot{u}_{EB}(x)) + k(u_M - u_{EB}(x)) = 0 \quad (3.8)$$

Equation (3.8) is converted to the frequency domain for a harmonic analysis. It is assumed that the solution takes the form: $u_M = \tilde{U}_M(\omega)e^{i\omega t}$, $\dot{u}_M = i\omega\tilde{U}_M(\omega)e^{i\omega t}$ and $\ddot{u}_M = -\omega^2\tilde{U}_M(\omega)e^{i\omega t}$. Rewriting the displacement amplitude as a function of the acceleration amplitude yields:

$$-\omega^2\tilde{U}_M(\omega) = \tilde{A}_M(\omega) \quad (3.9)$$

$$\tilde{U}_M(\omega) = \frac{\tilde{A}_M(\omega)}{-\omega^2} \quad (3.10)$$

Substituting and crossing out $e^{i\omega t}$ results in:

$$M\tilde{A}_M(\omega) + c\left(\frac{\tilde{A}_M(\omega)}{i\omega} - \frac{\tilde{A}_{EB}(\omega)}{i\omega}\right) + k\left(\frac{\tilde{A}_M(\omega)}{-\omega^2} - \frac{\tilde{A}_{EB}(\omega)}{-\omega^2}\right) = 0 \quad (3.11)$$

Rewriting the equation leaves:

$$\tilde{A}_{EB}(\omega) = \frac{\left(M + \frac{c}{i\omega} - \frac{k}{\omega^2}\right)}{\left(\frac{c}{i\omega} - \frac{k}{\omega^2}\right)}\tilde{A}_M(\omega) \quad (3.12)$$

Equation (3.12) can be used to qualitatively assess the influence of a change of the characteristics c and k of the resilient mount. No quantitative judgement can be made as the equation only represents part of the transfer from the machinery accelerations to the EB accelerations. The multiplier of $\tilde{A}_M(\omega)$ is the dynamic amplification factor (DAF) of the mount.

The DAF has the form $\frac{r+x}{x}$ where $x = \frac{c}{i\omega} - \frac{k}{\omega^2}$ and r is a positive constant. It is evident that an increase of x leads to a decrease of the DAF and vice versa. This means that an increase of c and a decrease of k results in a lower DAF, lower accelerations in the beam and eventually lower underwater radiated noise. It is expected that the relative influence of a change in c is larger for higher frequencies, as damping is applied per oscillation and higher frequencies have more oscillations. The relative influence of k is expected to be greater at lower frequencies, because inertial effects are more dominant at low frequencies compared to high frequencies.

This quick assessment of the effect of a change in mount parameters is based on heavy simplifications, so the judgement should be used with caution. In the real model, the equations are more complex and other phenomena could occur.

3.4.3. Parameter Tuning

Mount parameters such as the stiffness k and the damping c can be derived from off-the-shelf mounting systems produced by various companies. It is a goal of this research to find the influence of changing resilient mount parameters on the URN of a ship. Base parameters are taken from references, but deviations are applied to see the influence of a change in parameters. Market product data is thus used to get a feeling for the order of magnitude around which the parameters are varied.

In a brochure provided by [Vulkan Couplings \(2012\)](#) resilient mounts for marine applications can be found. The main requirement for choosing a suitable mount is the design load that should be able to withstand the total weight of the machinery of 20840 kg (204 kN). At least four resilient mounts are required to achieve stable mounting of the machinery, leading to a static load of 51 kN per mount. A suitable resilient mount from the brochure is type VDM-AV/ZA40S. This is a rubber mount suitable for heavy marine machinery and has a stiffness of 7.5 kN/mm ($7.5 \cdot 10^6$ N/m). With four mounts the total stiffness k is $30 \cdot 10^6$ N/m. The displacement corresponding to the static load of 51 kN is ± 1.7 mm, the dynamic displacement is not a quantity of interest in this research. The applicability of this mount type concerning the physical boundaries of the ship is therefore not assessed and it is assumed to be sufficient.

Typical damping coefficients for heavy marine applications are not provided by [Vulkan Couplings \(2012\)](#) or other manufacturers. ([Dassault Systemes, 2022](#)) provides order of magnitudes of damping ratios for several applications. The damping ratio is different from the damping coefficient and they are related via:

$$c = \zeta 2\sqrt{km} \quad (3.13)$$

Where c is the damping coefficient and ζ is the damping ratio. The influence of the magnitude of the damping ratio on the dynamics of a system was explained in Section 2.3.2. Dassault Systemes (2022) gives a ζ of 0.05 for rubber and 0.3 for auto shock absorbers. The selected resilient mount is partly made of specially designed rubber but is fundamentally different from the auto shock absorber. It is therefore decided that the base damping ratio is 0.1.

Table 3.7 shows the parameters for which the model is run, time constraints did not allow for more runs. A single run takes approximately 7.5 hours to complete. The base case include the parameters as argued above. In the succeeding runs, one parameter is varied and the other parameter is kept at the base case value. This means that all variations of the stiffness parameter run with a damping coefficient of $16 \cdot 10^4$ Ns/m and all variations of the damping run with a stiffness coefficient of $30 \cdot 10^6$ N/m.

Table 3.7: Resilient Mount Run Parameters.

	Stiffness coefficient k	Damping ratio ζ	Damping coefficient c
base case	$30 \cdot 10^6$ N/m	0.1	$16 \cdot 10^4$ Ns/m
	$10 \cdot 10^6$ N/m	0.02	$32 \cdot 10^3$ Ns/m
	$20 \cdot 10^6$ N/m	0.06	$95 \cdot 10^3$ Ns/m
	$40 \cdot 10^6$ N/m	0.14	$22 \cdot 10^4$ Ns/m
	$50 \cdot 10^6$ N/m	0.18	$28 \cdot 10^4$ Ns/m

3.4.4. FEM Modelling

This section explains how the resilient mount is modelled in addition to the EB model as explained in Section 3.3. The approach explained in Section 3.3 is applicable, however, some additional details are explained that are different compared to earlier sections.

Figure 3.19 shows a close up of the input location of the model. At the input location, an mck system is applied to the EB model. The mass is modelled as a rigid 1x1x1m cube with density 20840 kg/m^3 and a stiffness of $2 \cdot 10^{20}$ Pa. The mass is built up out of 64 (4x4x4) elements, as a lower amount of elements would cause technical software problems. The mass is centred at 1 m above the input location and is constrained in x and y-direction.

The mass is connected to the EB model via a longitudinal spring connection element of 1 m. The spring is connected to both bodies via remote attachment, meaning that the connection forces are equally distributed over the attached faces. The connection element is connected with rigid behaviour to the mass, ensuring no deformations on the contact face. The connection behaviour to the EB model is set to deformable, allowing for deformations of the EB model. The force of the spring is spread evenly over the attached face (green surface in Figure 3.20).

The spring element can be assigned stiffness and damping properties to model both the effects of the spring and the damper of the resilient mount. Full settings of the spring connection element for the base case are found in Appendix B. In the model case without a resilient mount but with acceleration input, stiffness and damping of the spring connection element are set to respectively 10^{20} N/m and 0 Ns/m. This model case is required to be able to correctly compare the mount cases with the case without a mount.

It would be best to model the input as a force on the mass. The kinematics of the mass are not described and interaction between the EB model and machinery mass block occurs. Unfortunately, only acceleration data was provided by the literature and in order to model the resilient mount a mass block is needed. A spring element with a harmonic force applied to it has no physical meaning when modelled. The mass is technically zero, leading to an infinite eigenfrequency of the machinery. Inputting the force ($m \cdot a$), derived from the available acceleration, on the mass block also has no physical meaning. In the EOM of Equation (2.2), the right-hand side becomes $m\ddot{u}(t)$, after which it cancels out with the inertial term on the left-hand side. The result is meaningless. Because of these reasons, it is decided to input the accelerations onto the mass block of the model instead of a force.

Inputting the accelerations instead of a force has some implications that have to be taken into account. First of all, no interaction between the EB and the machinery block occurs as the kinematics of the mass

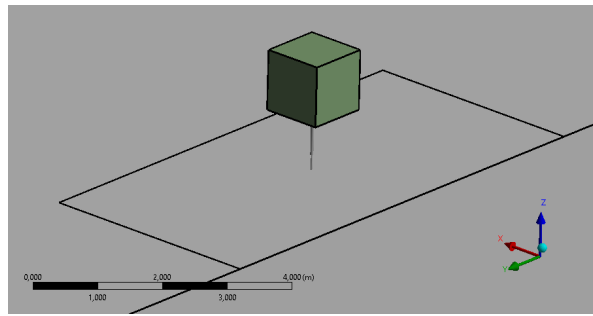


Figure 3.19: Close Up of the Machinery Block and Mount Geometry.

block are prescribed. Furthermore, changing the stiffness of the system leads to different outcomes for input accelerations or input forces. When the stiffness goes to infinity and accelerations are prescribed, the forces will go to infinity. The displacements are coupled to the accelerations via Equation (3.10) and take place as is prescribed. The underlying structure has to comply with the displacements regardless of the stiffness. On the other hand, when the stiffness goes to infinity and the force is used as input, the displacements go to zero.

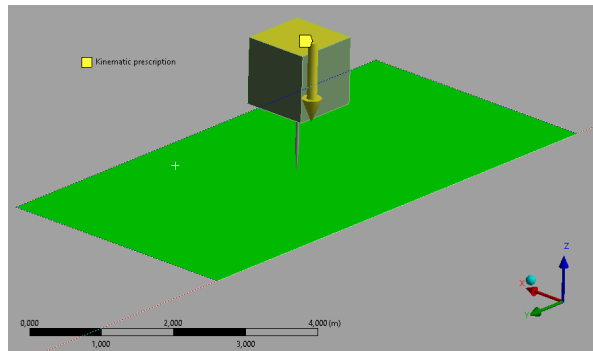


Figure 3.20: Modelling of the Machinery Block, the Mount and the Input.

Ansys 2021R2 allows only for displacements to be prescribed during a harmonic analysis. The displacements can be derived from the accelerations via Equation (3.10). The displacements have an inverse relationship with the accelerations coupled through the frequency. Displacements at lower frequencies are exponentially increased when the frequency goes to zero, as is seen in Figure 3.21. A unit acceleration is converted to displacements and imposed on the mass block in the model, seen as the kinematic prescription in Figure 3.20.

It is expected that the input of accelerations/displacements overestimates the results compared to a force input. At lower frequencies, the overestimation is expected to increase due to the quadratic increase of the input displacements.

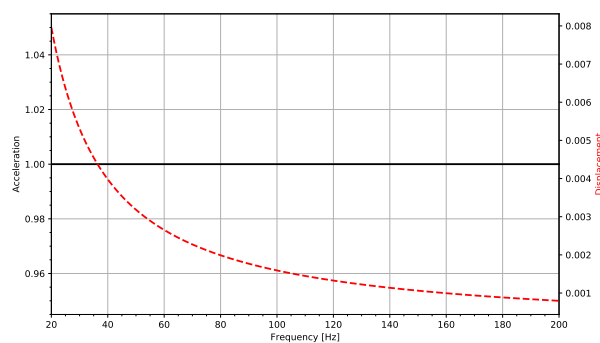


Figure 3.21: Unit Acceleration Amplitude and Corresponding Absolute Displacement Amplitude as a Function of Frequency.

3.5. 2-DOF Mount Schematisation

A more extensive parameter study can be conducted using a 2-DOF schematisation of the EB model and the resilient mount. The 2-DOF schematisation can be solved analytically allowing for very short run times and more freedom in the resilient mount parameter selection. Figure 3.22 shows this schematisation in which $K_{d,2}$ is the dynamic stiffness representing the EB model without the resilient mount. The dynamic stiffness $K_{d,2}$ is derived by application of a unit force to the EB base model of Section 3.3 and computing the averaged complex displacement of the force application location. The complex displacement is computed for the full frequency analysis range of 20 – 200 Hz. $K_{d,2}$ is then calculated using Equation (3.14):

$$K_{d,2}(i\omega) = \frac{\tilde{F}_{\text{unit}}(\omega)}{\tilde{U}_{\text{EB}}(\omega)} \quad (3.14)$$

Where $\tilde{F}_{\text{unit}}(\omega)$ is the unit force and $\tilde{U}_{\text{EB}}(\omega)$ is the averaged complex displacement of the EB model. This schematisation should match the EB model results for all combinations of parameters (k_1 and c_1) of the resilient mount. The 2-DOF schematisation computes the displacement of the machinery block u_1 and the displacement of the equivalent beam at the force input location u_2 . The metrics of interest in this research are not the displacements but the acoustic pressures and the source levels. Since the EB model is a linear model¹, the normalised results of the displacements should match the normalised results of the acoustic pressures. The transfer from acoustic pressure to source level is a non-linear computation requiring the absolute values of the pressures. The limitation of this 2-DOF schematisation is thus that normalised source levels cannot be computed.

The force input of the 2-DOF schematisation is expected to be more accurate for reasons explained Section 3.4.4. The disadvantage of this is that no absolute values with a physical meaning can be obtained. For this, acceleration input is needed. This is another limitation of the 2-DOF schematisation.

The derivation of the complex displacement amplitudes $\tilde{U}_1(\omega)$ and $\tilde{U}_2(\omega)$ is given below. The EOM's for the two masses are:

$$\begin{cases} m_1 \ddot{u}_1 + c_1(\dot{u}_1 - \dot{u}_2) + k_1(u_1 - u_2) = F_1 \\ m_2 \ddot{u}_2 + c_1(\dot{u}_2 - \dot{u}_1) + c_2 \dot{u}_2 + k_1(u_2 - u_1) + k_2 u_2 = 0 \end{cases} \quad (3.15)$$

Rewrite in matrix notation:

$$\begin{bmatrix} m_1 & 0 \\ 0 & m_2 \end{bmatrix} \begin{bmatrix} \ddot{u}_1 \\ \ddot{u}_2 \end{bmatrix} + \begin{bmatrix} c_1 & -c_1 \\ -c_1 & c_1 + c_2 \end{bmatrix} \begin{bmatrix} \dot{u}_1 \\ \dot{u}_2 \end{bmatrix} + \begin{bmatrix} k_1 & -k_1 \\ -k_1 & k_1 + k_2 \end{bmatrix} \begin{bmatrix} u_1 \\ u_2 \end{bmatrix} = \begin{bmatrix} F_1 \\ 0 \end{bmatrix} \quad (3.16)$$

Transformation to the frequency domain for harmonic analyses:

$$-\omega^2 \begin{bmatrix} m_1 & 0 \\ 0 & m_2 \end{bmatrix} \begin{bmatrix} \tilde{U}_1(\omega) \\ \tilde{U}_2(\omega) \end{bmatrix} + i\omega \begin{bmatrix} c_1 & -c_1 \\ -c_1 & c_1 + c_2 \end{bmatrix} \begin{bmatrix} \tilde{U}_1(\omega) \\ \tilde{U}_2(\omega) \end{bmatrix} + \begin{bmatrix} k_1 & -k_1 \\ -k_1 & k_1 + k_2 \end{bmatrix} \begin{bmatrix} \tilde{U}_1(\omega) \\ \tilde{U}_2(\omega) \end{bmatrix} = \begin{bmatrix} \tilde{F}_1(\omega) \\ 0 \end{bmatrix} \quad (3.17)$$

Rewriting as a system of equations grouping terms dependent on $\tilde{U}_1(\omega)$ and $\tilde{U}_2(\omega)$:

$$\begin{cases} (-\omega^2 m_1 + i\omega c_1 + k_1)\tilde{U}_1(\omega) - (i\omega c_1 + k_1)\tilde{U}_2(\omega) = \tilde{F}_1(\omega) \\ \underbrace{(-\omega^2 m_2 + i\omega c_2 + k_2)}_{K_{d,2}(i\omega)}\tilde{U}_2(\omega) - (i\omega c_1 + k_1)\tilde{U}_1(\omega) + (i\omega c_1 + k_1)\tilde{U}_2(\omega) = 0 \end{cases} \quad (3.18)$$

The first term in the second equation is the dynamic stiffness of the EB model $K_{d,2}(i\omega)$. Substituting $K_{d,2}(i\omega)$ and writing in matrix notation gives:

¹Linear, in this case, means that the quantity of interest scales linearly with the input of the system. Doubling the input force doubles the displacements of the equivalent beam and doubles the acoustic pressures.

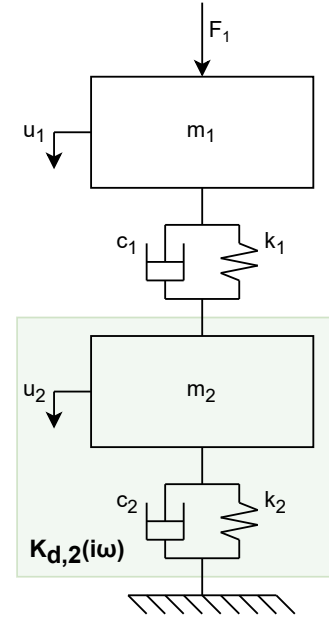


Figure 3.22: 2-DOF Schematisation

$$\underbrace{\begin{bmatrix} -\omega^2 m_1 + i\omega c_1 + k_1 & -i\omega c_1 - k_1 \\ -i\omega c_1 - k_1 & K_{d,2}(i\omega) + i\omega c_1 + k_1 \end{bmatrix}}_{\mathbf{A}(\omega)} \underbrace{\begin{bmatrix} \tilde{U}_1(\omega) \\ \tilde{U}_2(\omega) \end{bmatrix}}_{\mathbf{u}(\omega)} = \underbrace{\begin{bmatrix} \tilde{F}_1(\omega) \\ 0 \end{bmatrix}}_{\mathbf{B}(\omega)} \quad (3.19)$$

This system of equations can be solved for the complex displacement amplitudes $\tilde{U}_1(\omega)$ and $\tilde{U}_2(\omega)$ using:

$$\mathbf{u}(\omega) = \mathbf{A}(\omega)^{-1} \mathbf{B}(\omega) \quad (3.20)$$

3.6. Solving and Data Processing

This section explains how the models are solved and how to data is processed.

3.6.1. Solution Strategies

To solve the model a full harmonic acoustic analysis is performed in Ansys 2021R2. The analysis frequency range is set to 20 – 200 Hz with 361 solution intervals (step size of 0.5 Hz) for the base EB model and 91 solution intervals (step size of 2 Hz) for the Ansys model including the resilient mount. The analysis is time and memory consuming, more solution intervals are possible, but this increases the computational time and required memory considerably.

A Far-field Maximum Pressure radial solution entry is placed at a radius of exactly 1000 meters below the bottom of the beam centred at the input application location. This solution entry is used to record the far-field acoustic pressure in Pascals caused by the vibrations of the beam in all directions. The acoustic pressure is as a result of a unit acceleration or force on the beam, so the pressure should be corrected for the input spectrum. Next, the acoustic pressures are converted to the Source Level spectrum of the beam in Decibels using Equations (3.3) and (3.4). The source level spectrum is determined relative to the point at the bottom of the beam exactly centred with the input application location.

3.6.2. Capturing the Results and Spatial Averaging

The far-field acoustic pressures are computed in the radial directions below the beam. 300 spatial intervals are used to compute the pressures at 1000 meters from the ship's machinery location. The Ansys scripting feature was used to automatically save the spatial acoustic pressure data over the analysis frequencies to a .csv file. A Python script was then used to modify and read the exported .csv file before general Python data analysis was performed.

A wave interference pattern (radiation pattern) emerges in spatial directions in the acoustic domain. Due to the harmonic forcing on the beam, a sinusoidal vibration pattern occurs as depicted in Figure 3.23. Towards the ends of the beam, the vertical displacements are partly dissipated as a result of the system damping. Every place of the beam with large deformations could be seen as an acoustic source from which waves are radiated as shown by the crosses in Figure 3.23. The combined wave patterns amplify and cancel out at the locations where the lines intersect. Looking at some distance below the radiating structure, an oscillating pattern occurs. Specific locations experience the amplified sound waves and elsewhere the cancelled-out waves are experienced. Because the structure dissipates the structural waves in outwards direction, the waves do not completely cancel out, but the pressure level is decreased or increased from its mean value.

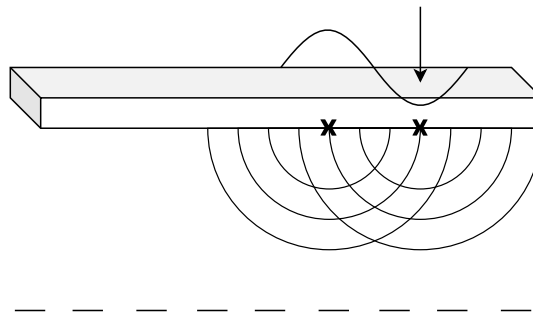


Figure 3.23: Schematic Showing the Generation of Interfering Waves

A harmonic input of a higher frequency shows more oscillations and more radiating 'crosses' on the beam. In the wave interference patterns more waves simultaneously amplify or cancel out each other, altering the total radiated noise pattern as a function of frequency.

Fluctuations in the spatial pressure pattern are caused by the unique radiation characteristics and the wave interference of the structure. The pattern is expected to smooth out for larger distances as the wave pattern develops. The relative influence of the distance between the radiating 'crosses' of the structure decreases as the radiated distance from the source increases. Furthermore, pressure gradients in a fluid naturally lead to pressure redistribution and evening out of the fluctuations.

Spatial averaging is applied to obtain more constant results as a function of frequency and to compare the model data with real ship measurements. In real ship measurements, spatial averaging is also applied as the noise is measured during a ship passage. The noise levels are generally defined as the average over $\pm 30 - 45^\circ$ of the closest point of approach (CPA) of the ship. (ITTC, 2017)

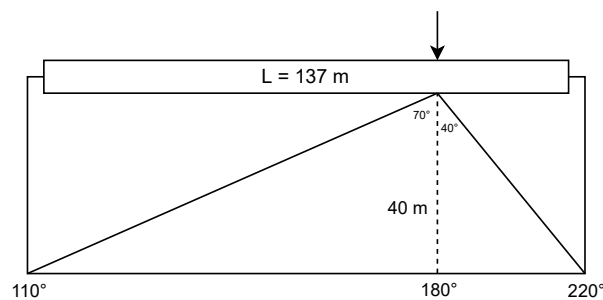


Figure 3.24: Model Dimension and Directions Within the Acoustic Domain [Not to Scale].

Figure 3.24 shows the directions and angles within the acoustic domain of the model together with model dimensions required to calculate the angles. The corners of the acoustic domain could show unwanted artefacts in the model results because of a non-continuous radiation plane. The average value over the $150 - 210$ degrees direction is calculated to account for the frequency-dependent changes in the directional radiation pattern. This angle range is in accordance with literature definitions of the ITTC (2017) and is within one radiation plane of the model.

3.7. Assumption Overview

In this chapter, numerous assumptions have been made. Assumptions go hand in hand with the modelling of real-world problems and the number of assumptions grows for simpler models. It is important to obtain an overview of the assumptions made to judge and interpret the results within the right context.

The assumptions made during the construction of the equivalent beam model are:

- No pre-stress of the beam from hydrostatic pressures;
- Prismatic beam, no spatial variations in density or stiffness;
- Symmetry conditions on the equivalent beam prevent lateral eigenmodes;
- Acceleration input application location;
- Acceleration only in Z-direction;
- Individual machinery accelerations combined into one unit;
- Machinery rigidly connected to ship;
- Poisson ratio of 0;
- Constant structural damping ratio of 0,02;
- Fluid properties (density, temperature and wave speed) to remain constant;
- Combination of dimensions and dynamical properties of the Giant 5 barge, and the machinery acceleration input from [Zhang et al. \(2019\)](#).

In the application of the resilient mounts to the existing EB model the following assumptions are made in addition to the previously mentioned assumptions made for the EB model without resilient mounts:

- Resilient mount simplified to a single spring and damper;
- Deformable remote attachment to EB model.

4

Results

This chapter shows the results that have been found using the models and the methodology described in Chapter 3. Section 4.1 presents the results obtained from the base EB model with a force input. Section 4.2 presents the results of the EB model with and without a resilient mount and with acceleration input. Furthermore, the results of the parameter study of the resilient mount conducted with the 2-DOF schematisation are described.

All results of a single analysis frequency are plotted at 192 Hz. This frequency is chosen as the acoustic response was found to be the highest.

4.1. Equivalent Beam

Figure 4.1 shows the 3D model including the acoustic response to a unity force at 192 Hz. This frequency is chosen for this image as the acoustic response was found to be the highest to this frequency. It is evident that the main acoustic waves originate from the location exactly under the force application. In Figure 4.2 it can be seen that the beam structure has the largest displacement at the force location and that the structural waves spread from there out. The waves are rapidly reduced and the far left end of the beam experiences minimal deformations.

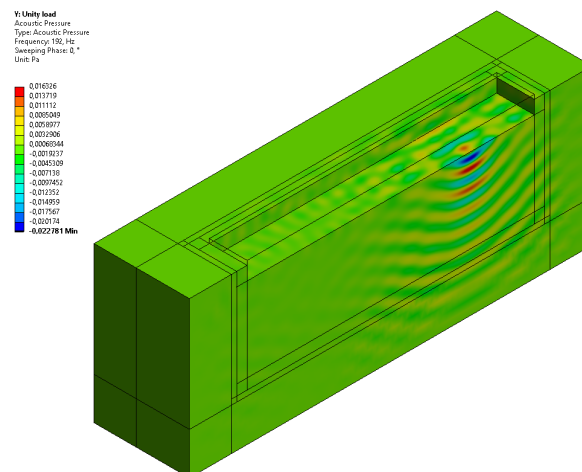


Figure 4.1: Acoustic Waves in the Equivalent Beam Model at 192 Hz.

4.1.1. Far-Field Acoustic Pressure

Figures 4.3 and 4.4 show the directional far-field acoustic pressure pattern as a result of the unity load and the machinery force spectrum as given in Figure 3.9d. 90 and 270 degrees coincide respectively with the bow (left) and the stern (right) of the EB model. The radius of the line on which the far-field data is computed is

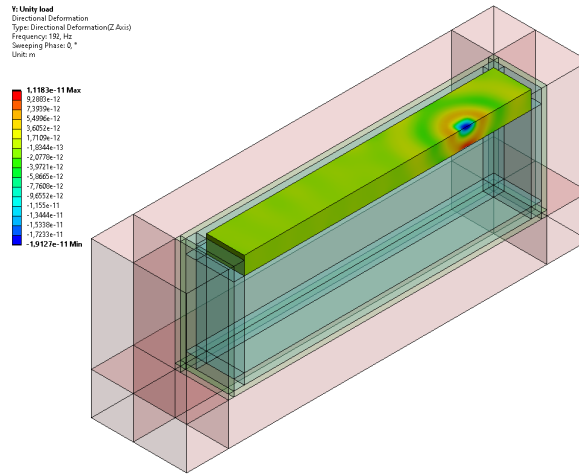


Figure 4.2: Displacements of the Equivalent Beam Model at 192 Hz.

1000 meters. The solid line represents the pressures at 192 Hz, the frequency showing the largest pressure response straight below the force application location. The dashed line represents the frequency averaged spatial pressure data.

The acoustic domain of the model fits narrowly around the beam in vertical direction to save computational time. However, this does not accommodate proper sideways noise radiation as the domain is too small in those directions to fully develop the acoustic waves. The maximum angle range between which acceptable data can be expected is between 110 and 220 degrees. No data of meaningful magnitude is found in Figures 4.3 and 4.4 outside of this range.

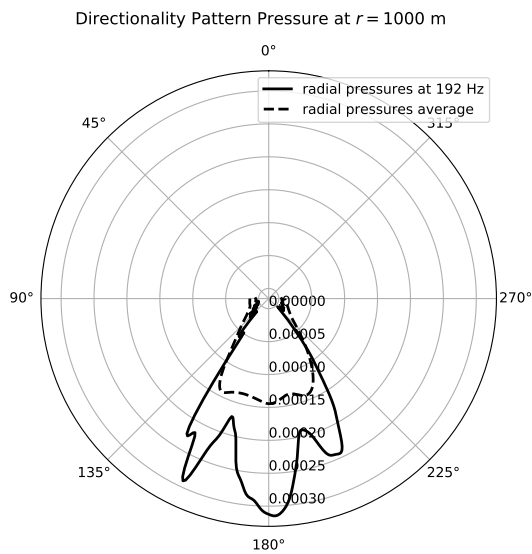


Figure 4.3: Directional Far-Field Acoustic Pressure Pattern Due to Unity Load.

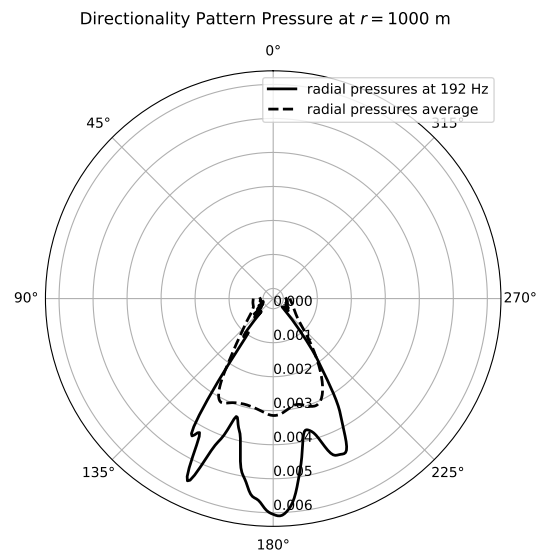


Figure 4.4: Directional Far-Field Acoustic Pressure Pattern Due to Machinery Force Spectrum.

Figures 4.5 and 4.6 shows respectively the far-field acoustic pressure spectrum due to the unity load and the machinery force spectrum. In Figure 4.5 the 180 degrees line corresponds to the far-field location located straight underneath the force application location, the maximum line corresponds to the maximum pressure over all directions and the average line is the average as explained in Section 3.6.2. It can be seen from the 180 degrees line that the eigenmodes of the beam mainly influence the low-frequency noise. Significant peaks can be seen in the data at frequencies below 50 Hz. At frequencies above 90 Hz, individual eigenmodes no

longer show a significant increase in acoustic pressure. The acoustic pressures seem to gradually increase for higher frequencies. An interesting phenomenon occurs where there is a constant oscillation in the far-field acoustic pressure data, this is elaborated upon in the discussion in Section 5.2.

The applied spatial averaging (see Section 3.6.2) seems to reduce the sinusoidal pattern, as is seen in the averaged and maximum far-field acoustic pressure spectrum (Figure 4.5). No large changes were seen in the machinery force acoustic pressure spectrum as the force spectrum overrules the unit response. Peak reduction at some frequencies is noticeable.

Figure 4.6 clearly shows that the influence of the machinery force input spectrum is of great importance to the overall pressure spectrum. The peaks are relatively high compared to the rest of the spectrum, flattening out the influence of the individual eigenmode peaks. The largest peak response of the system to a unit load occurs at around 20 Hz in Figure 4.7. The peak is a doubling of the pressure resulting in a source level peak of just 6 dB. The remainder of the spectrum is significantly smoother and thus it is clear that the influence of the individual eigenmodes is only of importance at the lowest frequencies. The insignificance of the mode peaks is magnified due to the input spectrum, see Figure 4.6. The input force peaks are magnitudes larger than other areas of the spectrum, meaning that individual eigenmodes are only of importance if they coincide with a peak in the input force spectrum.

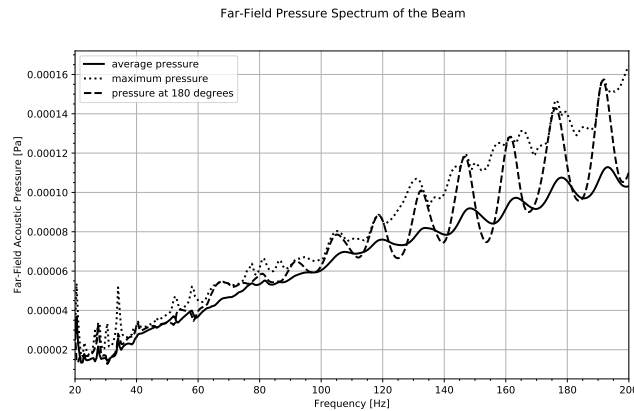


Figure 4.5: Far-Field Acoustic Pressure Spectrum for the Equivalent Beam Model With a Unity Load at 1000 m.

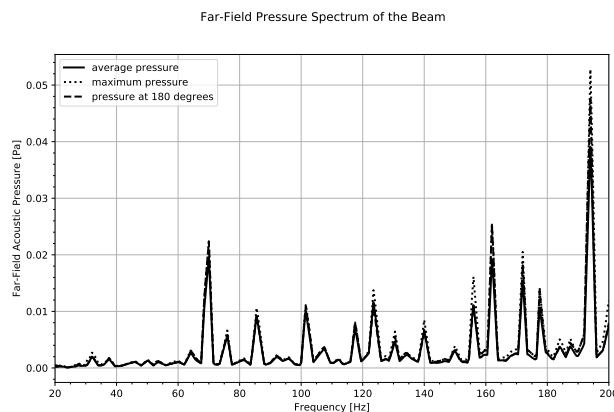


Figure 4.6: Far-Field Acoustic Pressure Spectrum for the Equivalent Beam Model With the Machinery Load at 1000 m.

4.1.2. Source Levels

Figures 4.7 and 4.8 show the calculated source level of the EB model for the analysed frequency range as a response to the unity load and the machinery force spectrum. The average spectrum is again taken over the 150-210 degrees direction and the maximum spectrum is taken as the maximum over all directions. The source level spectra are calculated from the pressure data in Section 4.1.1 using the equations from Section 3.2.6.

From the figures, it can be seen that the source level shows a rather linear relation versus frequency. At frequencies below 40 Hz, the influence of resonant peaks from the eigenmodes can be identified and from 90 Hz upwards effects from the wave interference patterns can be seen. The differences between the average, maximum and 180 degrees source level graphs are minimal, especially in the noise as a result of the machinery load. However, it should be noted that the magnitudes are in Decibel scale and the relative difference could be misleading.

Figure 4.8 shows substantial changes in noise levels for different frequencies. Around 70 Hz a difference of just over 30 dB re $1 \mu\text{Pa}^2\text{m}^2$ was calculated. In terms of acoustic pressure, this is a factor difference of approximately 2^5 . The origin of the high fluctuation behaviour on the Decibel scale is the rough machinery force input spectrum found in Figure 3.9.

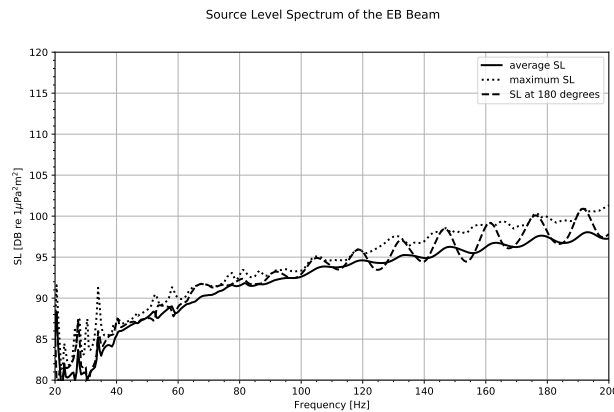


Figure 4.7: Source Level Spectrum for the Equivalent Beam Model With a Unity Load.

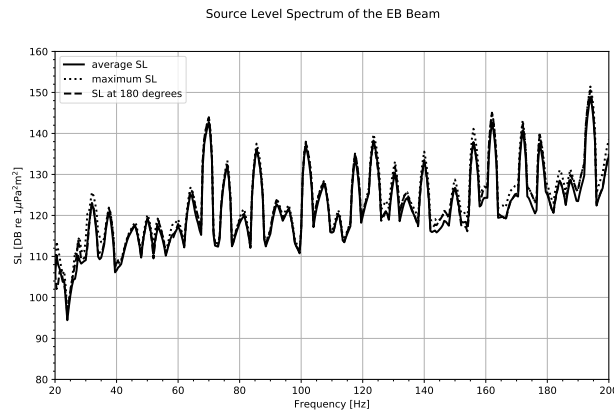


Figure 4.8: Source Level Spectrum for the Equivalent Beam Model With the Machinery Load.

The source level in all directions at 192 Hz and averaged over all frequencies can be seen in Figures 4.9 and 4.10. The source level at 192 Hz is chosen as this showed one of the loudest responses. From vertical to horizontal directions a more staggered pattern emerges. This is likely caused by the model constraints and the vertical radiation characteristic of the EB model.

As explained earlier, outside of the 110-220 degrees direction range no meaningful results should be expected. Improperly developed acoustic waves in these directions could result in this staggered pattern.

The EB model, its geometry and the vertical machinery forcing result in a predominantly downwards radiated noise wave pattern. At more horizontal angles, this could result in a staggered pattern as well.

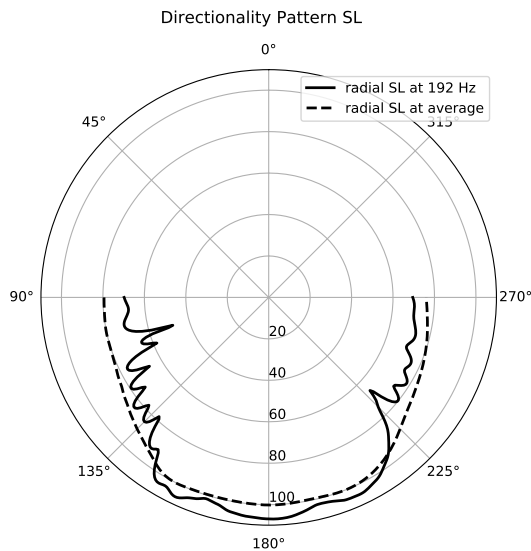


Figure 4.9: Directional Source Level Pattern Due to Unity Load

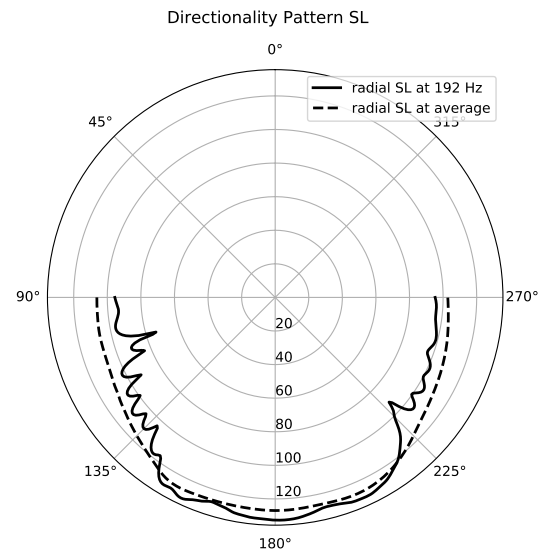


Figure 4.10: Directional Source Level Pattern Due to Machinery Force Spectrum

4.2. Resilient Mount Application

In this section, the results of the resilient mount are presented. First, the source levels for the case with no mount are compared to the cases with the resilient mount and changing mount parameters. The cases are computed with the acceleration spectrum as input on the machinery mass as explained in Section 3.4. This input is different from the base EB model, but given the lack of data, it was required to use acceleration as input on the model including the mount. The case with no mount is also computed with acceleration as input to accommodate proper comparison. A comparison of the far-field acoustic pressures is also plotted, however, the reduction of the pressure is very significant, making the graphs unclear. Normalised graphs of the pressure have been created and can be found together with the unnormalised graphs in Appendix D.2.

Subsequently, the results of the 2-DOF schematisation are presented showing the normalised complex displacement amplitude \tilde{U}_2 as a function of the mount damping ratio and stiffness. The models presented in this research are linear, implying that the normalised values of the displacement are similar to the normalised values of the acoustic pressure. Normalised values of the source level are not computed as the transfer from acoustic pressure to source level is non-linear. Absolute values of the acoustic pressures are needed, which the 2-DOF schematisation is not able to compute. Normalised values of the source level can be derived from Figures 4.11 and 4.13 and are presented in Section 4.2.3. All normalised results are normalised to the resilient mount with base settings of $k = 30 \cdot 10^6$ N/m and $\zeta = 0.1$ ($c = 16 \cdot 10^4$ Ns/m).

4.2.1. Source Levels

Figures 4.11 and 4.13 show the source level spectra of the EB model for the case without a mount (modelled as an infinite stiff mount) compared to the cases with varying resilient mount parameters. Figures 4.12 and 4.14 show the absolute decrease of the source level with a resilient mount relative to the case without a mount.

From Figures 4.11 and 4.12 it can be seen that the base settings of the resilient mount reduce the source level by approximately 55 dB re $1 \mu\text{Pa}^2\text{m}^2$ at the lowest frequencies and by approximately 48 dB re $1 \mu\text{Pa}^2\text{m}^2$ at the highest frequencies. At the lower frequencies strong peaks in the reduction are observed, with peak reductions of 62 dB re $1 \mu\text{Pa}^2\text{m}^2$ for the resilient mount with base settings. From 60 Hz and above a linear SL reduction was observed that gradually lessened for higher frequencies. The influence of a change in damping ratio ζ is interestingly opposite of the expectations posed in Section 3.4.2. An increase in the damping ratio leads to an increase of the source level along the entire frequency analysis range. A decrease in the damping ratio leads to a decrease of the source level along the entire frequency analysis range. The relative increase or decrease seems to grow for higher frequencies. A change of the damping ratio of the resilient from 0.18 to 0.02 increased the SL reduction from 45 dB re $1 \mu\text{Pa}^2\text{m}^2$ to 60 dB re $1 \mu\text{Pa}^2\text{m}^2$.

From Figures 4.13 and 4.14 it shows that the influence of a change in mount stiffness k has the most effect

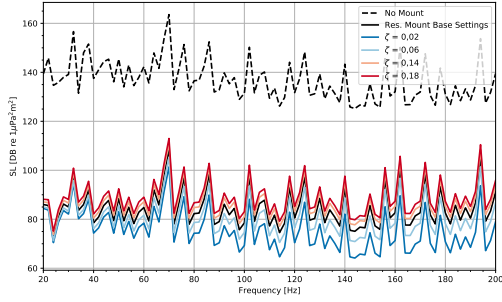


Figure 4.11: Source Level Spectrum for Different Damping Ratios.

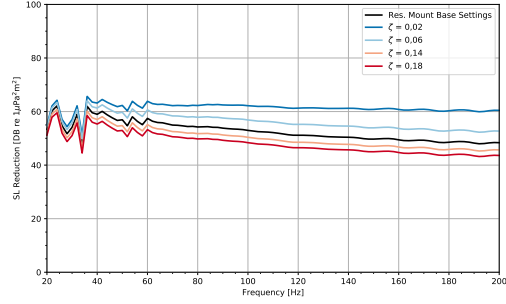


Figure 4.12: Source Level Reduction for Different Damping Ratios.

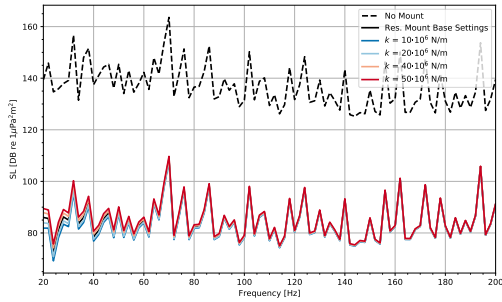


Figure 4.13: Source Level Spectrum for Different Stiffness Values.

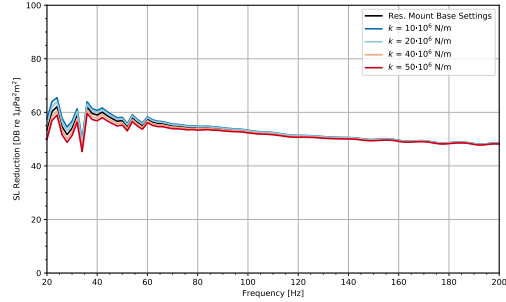


Figure 4.14: Source Level Reduction for Different Stiffness Values.

at the lowest frequencies. At the lowest frequencies, the change in source level between the highest and lowest stiffness is around 8 dB re $1 \mu\text{Pa}^2\text{m}^2$, whilst at the highest frequencies, the change is virtually zero. This was as expected from Section 3.4.2. Furthermore, the reduction of the resilient mount with base parameters are similar as described for Figure 4.12.

Figures 4.15 and 4.16 show the source level directionality patterns of the case with no mount compared to the cases with mount and varying damping ratio and stiffness. Both radial plots are computed at 192 Hz. It can be seen that the reduction in source level is rather constant in all directions. In Appendix D.1 the radial plots are given without the 'no mount' case and normalised to the source level of the case with the base settings. From the normalised radial plots, it can be seen that a change in damping ratio has an even effect on the source level in all directions. A change in the stiffness has slightly more effect on the source level at more horizontal directions (90 and 270 degrees). However, as explained in Section 3.6.2 the angle range within to expect useful results is 110 – 220 degrees, so not much can be said about the more horizontal directions.

4.2.2. 2-DOF Schematisation

In this section, the results of the 2-DOF schematisation of the EB model are presented. Firstly, the results are compared to Ansys to judge if the schematisation was correct. After that, the results of the parameter study conducted with the 2-DOF schematisation are presented. All results of the 2-DOF schematisation are expressed as the complex displacement amplitude \bar{U}_2 , see Section 3.5. The models in this research are linear, meaning that the normalised displacement is similar to the normalised pressures. Normalised results for the source levels are provided from the Ansys runs, as those are unobtainable from the 2-DOF schematisation.

The results of the 2-DOF schematisation of the problem were compared with the results from Ansys runs with matching mount parameters and a unit force input. The comparison can be seen in Table 4.1 and shows that the 2-DOF schematisation is accurately describing the model. The force input was used here for reasons explained in Section 3.5. The errors for both damping ratios are less than 1%, leading to the conclusion that the 2-DOF schematisation is accurate and usable for the parameter study.

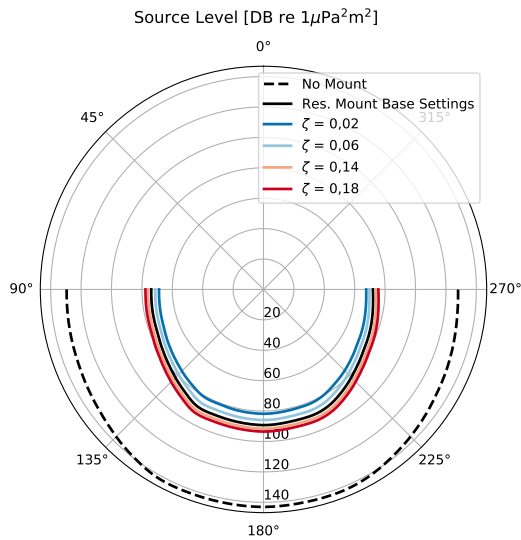


Figure 4.15: Directional Source Level Pattern at 192 Hz for Different Damping Ratios.

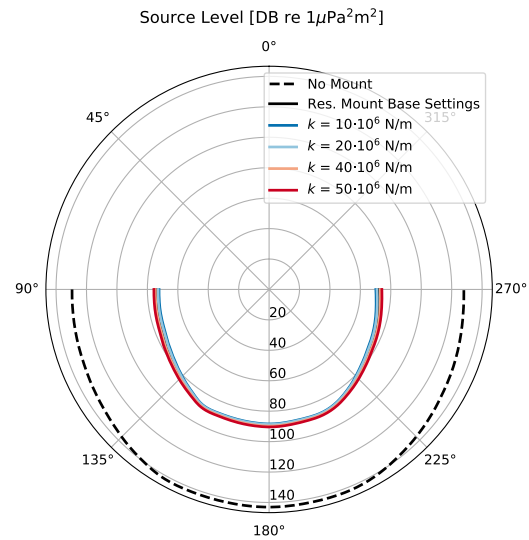


Figure 4.16: Directional Source Level Pattern at 192 Hz for Different Stiffness Values.

Table 4.1: Ansys Results and 2-DOF schematisation Results Comparison at 192 Hz.

Damping ratio ζ	Amplitude Ansys [m]	Amplitude 2-DOF [m]	Relative Error
0,02	$2,9924 \cdot 10^{-14}$	$2,9642 \cdot 10^{-14}$	0,94%
0,18	$2,0492 \cdot 10^{-13}$	$2,0454 \cdot 10^{-13}$	0,19%

4.2.3. Parameter Study

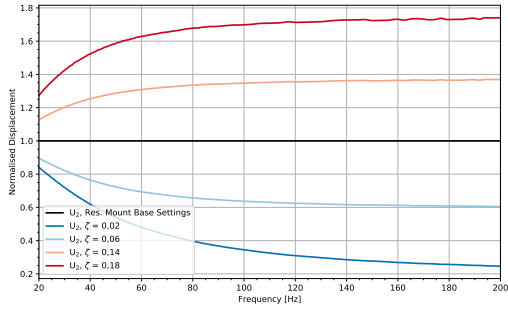
Figures 4.17a and 4.17b show the results obtained from the 2-DOF schematisation for different values of the damping ratio ζ and the stiffness k . It can be seen that a change in damping has an increasing influence on the response for an increase in frequency. The increase flattens out at higher frequencies. The stiffness has an opposite effect compared to the damping ratio. The influence of a change in stiffness increases exponentially towards lower frequencies and is nearly zero at the highest analysis frequencies.

Figures 4.17c and 4.17d shows the normalised source levels as a result of a change in the damping ratio or stiffness of the resilient mount. The results are computed by the runs performed in Ansys with acceleration input. It is observed that a reduction of the damping ratio has a significantly larger effect than an increase of the damping ratio. A decrease of the damping ratio from 0,1 to 0,06 results in a 5% reduction of the source level at frequencies above 100 Hz. A change stiffness from $30 \cdot 10^6$ N/m to $20 \cdot 10^6$ N/m results in a reduction of the source level at the lowest frequencies of approximately 5%. At the highest frequencies the reduction is almost negligible.

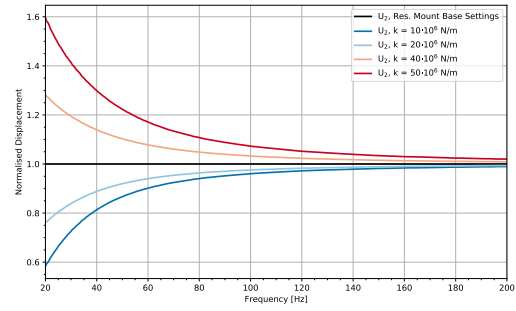
The staggered pattern in both Figures 4.17c and 4.17d originates from the acceleration spectrum multiplication to obtain the source levels. The transfer from acoustic pressure to source level is non-linear, resulting in the staggered artefacts of the acceleration spectrum being noticeable in the normalised source level graphs.

The 2DOF-schematisation allowed for quick calculations and thus more parameter combinations were possible than compared to Ansys. Figures 4.18a and 4.18b show the normalised displacement \tilde{U}_2 as a function of combinations of the damping ratio ζ and the stiffness k at 192 Hz. Figure 4.18a covers the full range of k (from 0 to 10^{11} N/m) and ζ (from 0 to 1) and Figure 4.18b covers the range of interest around the base settings of the resilient mount. Red indicates a relative increase in displacement, blue indicated a relative decrease in displacement and white indicated no change in displacement. Figure 4.18b is located in the very left part of Figure 4.18a. Figures 4.19a and 4.19b present a top view contour plot of Figures 4.18a and 4.18b.

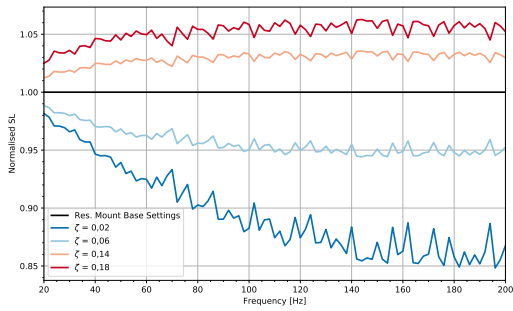
It can be seen that around the base settings of the resilient mount a decrease in the stiffness and damping ratio results in a decrease of the normalised displacements. Only for stiffness values approximately 10^3 times larger than the base settings ($30 \cdot 10^6$ N/m) it can be seen that an increase of the damping leads to a decrease



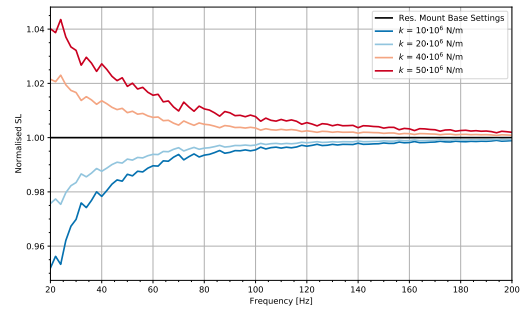
(a) Normalised Displacement \tilde{U}_2 for Different Damping Values.



(b) Normalised Displacement \tilde{U}_2 for Different Stiffness Values.



(c) Normalised Source Level for Different Damping Values.

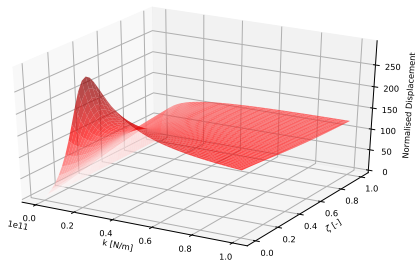


(d) Normalised Source Level for Different Stiffness Values.

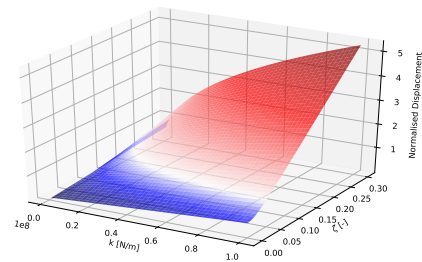
Figure 4.17: Displacement \tilde{U}_2 (a and b) and Source Level (c and d) Normalised to the Response with the Resilient Mount Base Settings.

of the response. Interestingly, it can also be seen that a higher stiffness increases the effect of a change in damping ratio. The slope along the ζ -axis increases for higher stiffness values around the resilient mount base settings.

Figures 4.18a, 4.18b, 4.19a and 4.19b are given with an alternative colour scheme in Appendix D.3.



(a) In Full Range.



(b) Around the Resilient Mount Base Settings.

Figure 4.18: Surface Plots of Displacement \tilde{U}_2 at 192 Hz for Combinations of stiffness Values and Damping Ratios Normalised to the Response with the Resilient Mount Base Settings.

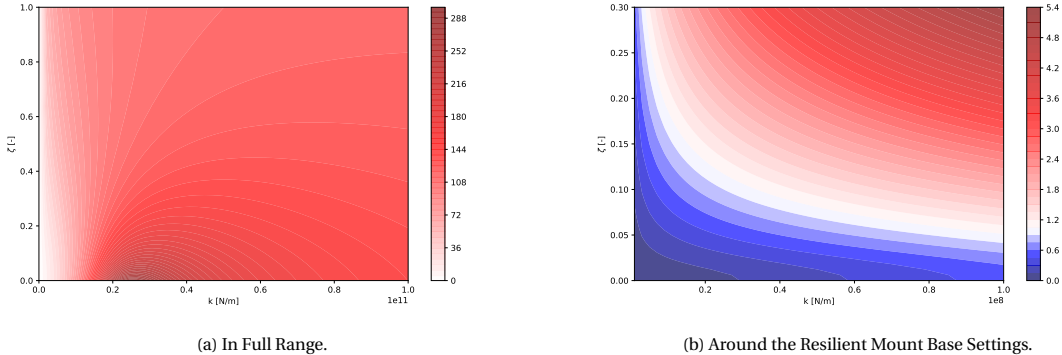


Figure 4.19: Contour Plots of Displacement \bar{U}_2 at 192 Hz for Combinations of stiffness Values and Damping Ratios Normalised to the Response with the Resilient Mount Base Settings.

5

Discussion

The methodology and findings presented in this research go hand-in-hand with assumptions. The impact of assumptions and limitations on model results is discussed in this chapter, and the results are interpreted in the context of the topic. Section 5.1 discusses the input of the model and the influence on the results. A comparison is made between acceleration and force input and the differences are quantified. The sinusoidal artefact in the model results is discussed in Section 5.2, along with possible causes and solutions. Section 5.3 assesses the EB model's accuracy by comparing the model results to the data from the reference case presented in Section 3.2.1. Section 5.4 discusses the steps made to obtain the parameter study of the resilient mount and gives an explanation of the results that were obtained. Sections 5.5 and 5.6 go into the remaining assumptions summarised in Section 3.7 and the computational limitations of the model. Finally, Section 5.7 reflects back on the results presented in Chapter 4 taking the presented discussion points into consideration. The significance of the research and its practical applications are discussed alongside the reflections on the results.

5.1. Model Input

The model input had an influence on the model that has to be acknowledged. In this section, the interpolation of the input spectrum by the model results is discussed. Furthermore, the difference in results between a force input and acceleration input is looked at.

5.1.1. Spectrum Interpolation

Figures 4.6 and 4.8 presented the far-field acoustic pressure and the source level spectra as a response to the machinery loads. The rough data for the machinery input spectra lead to the response data showing a large magnitude spread over the frequencies. The machinery acceleration data were obtained from literature but were available in graph form as opposed to database form. The input frequency points of the machinery data do not necessarily overlap with the analysis frequency points. The machinery input data is therefore forced to be interpolated for frequency points that do not match with the analysis frequency points. For this reason, peaks in the machinery input data were partially skipped. Peaks are the most important features of the spectrum, as maximum responses are expected there.

The interpolation to match the frequency analysis points can be seen in Figure 5.1 for the engine and it shows that peaks were reduced by the computation. The largest peak reduction occurs around 70 and 101 Hz and is 11%. It is evident that the magnitudes of the peaks of Figures 4.6 and 4.8 are slightly reduced due to this interpolation effect. The largest effect is noticeable in Figure 4.6 and the effect is barely noticeable in Figure 4.8 as it is in Decibel scale. This effect occurred also for the gearbox and the diesel generator to a similar extent.

The parameter variation of the resilient mount required multiple model runs to be conducted. Model runs were time-consuming and took up to 33 hours. The frequency analysis step was increased during the parameter variation such that a single run lasted 7.5 hours. This resulted in an interpolation of the input spectrum similar to the base EB model presented in Figure 5.1. The interpolated input spectrum for the resilient mount parameter variations is given in Figure 5.2.

The combined input spectrum was already interpolated to a frequency step size of 0.5 Hz during the

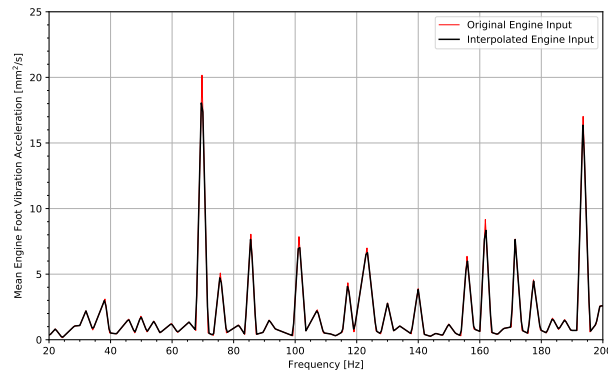


Figure 5.1: Original Input Spectrum Versus the Interpolated Input Spectrum for the EB Model.

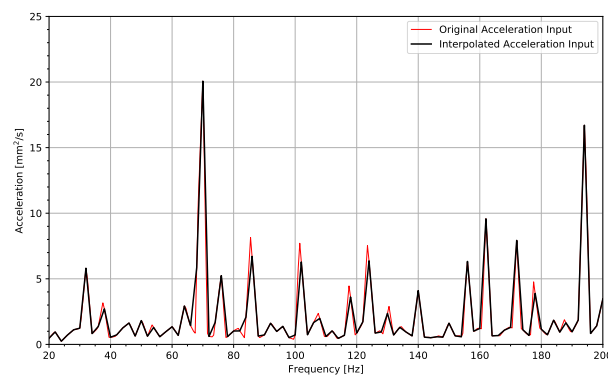


Figure 5.2: Original Input Spectrum Versus the Interpolated Input Spectrum for the Resilient Mount Application.

combination of the separate machinery spectra. The interpolation has missed parts of the peak in the middle of the spectrum. However, the largest peaks are fully accounted for.

5.1.2. Acceleration Versus Force Input

Acceleration input was expected to overestimate the source levels compared to force input. This expectation was first mentioned in Section 3.4.4 and was verified by the results. For the case of no-mount, the force input results and the acceleration input results were computed. The force input results were obtained by removing the machinery mass and applying the force $F_{\text{machinery}} = M_{\text{machinery}} \cdot a_{\text{machinery}}$ on the input location.

The force input is derived from acceleration with the assumption of a rigid connection. However, the acceleration spectra measured by Zhang et al. (2019) are a result of a machinery force with some sort of stiffness and damping within the mounting system. The forces due to the accelerations of the machinery are thus not equal to the force exerted on the ship's hull structure. Furthermore, the accelerations of the machinery do not correspond to a rigid mounting system and applying those accelerations to a rigid mount most-likely lead to an overestimation of the source level spectrum.

In Figure 5.3 the source level of both the acceleration input and the force input are plotted. Figure 5.4 shows the same results but normalised to the force input, such that the relative differences between both methods are clearly observable.

From Figures 5.3 and 5.4 it was concluded that the acceleration input lead to overestimation of the source levels compared to the force input. The overestimation grows exponentially towards lower frequencies. This was caused by the relation between the displacement amplitudes and acceleration amplitudes of Equation (3.10). Ansys 2021R2 only allowed the displacement to be prescribed. Towards zero frequency, the displacement amplitudes go towards infinity, leading to infinite response of the model and infinite source level.

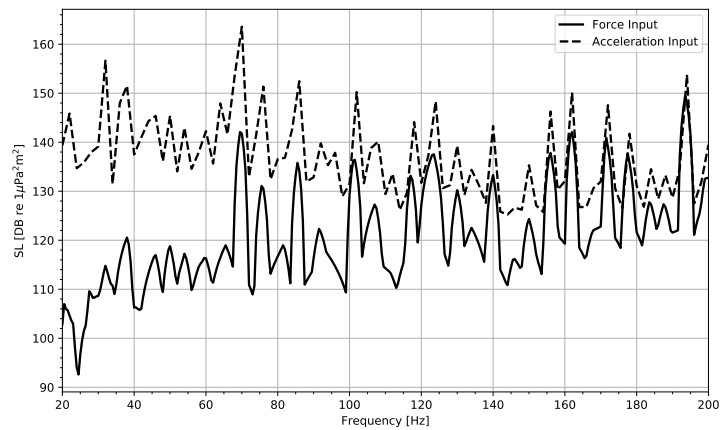


Figure 5.3: Source Level Spectra for Acceleration Input and Force Input.

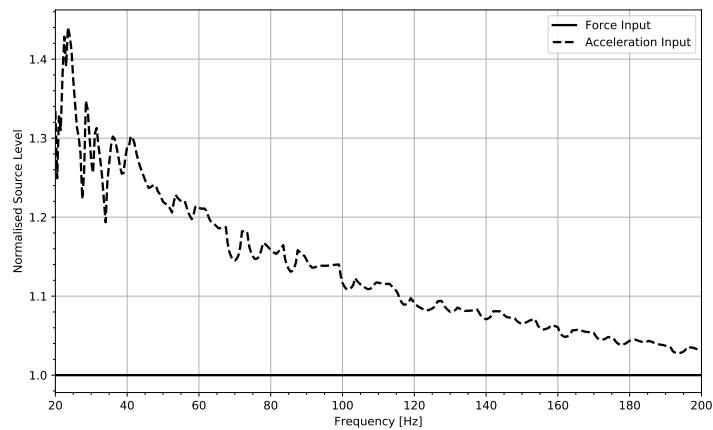


Figure 5.4: Source Level Spectra for Acceleration Input and Force Input Normalised to the Spectrum for Force Input.

The overestimation of the acceleration input was thought to be reduced during the application of the resilient mount. As explained in Section 3.4.4, the forces in the equivalent beam could be substantial for input accelerations and no resilient mount. This is because the displacements are prescribed and the high stiffness of the equivalent beam leads to high forces in the beam. With the application of the resilient mount, the machinery block can move individually and the prescribed displacements are not transferred to the equivalent beam through means of a rigid connection. The prescribed displacements on the machinery block will eventually result in a spring force on the equivalent beam, leading to smaller displacements and forces for a high stiffness of the equivalent beam.

5.2. Sinusoidal Pattern in Frequency Domain

A counterintuitive sinusoidal wave pattern was seen in the results of Figure 4.5. Possible explanations including the necessary data for proof are given in this subsection. The first plausible cause is the interaction with the PML layers. The second cause is the domain size of the model.

5.2.1. PML Layer Influence

A secondary model, similar to the EB model, was created in which a single point source was used to generate acoustic waves. The results revealed a sinusoidal pattern in the frequency domain, indicating that the sinusoidal pattern was caused by PML layer issues.

At the interface between the acoustic domain and the PML layer, the energy flux was computed to see if significant reflections would occur. The energy flux was computed by multiplying the acoustic pressure with the velocity and is plotted in Figure 5.5. Figure 5.5a corresponds to a frequency of 192 Hz and Figure 5.5b corresponds to a frequency of 196 Hz. At 192 Hz the far-field pressure response showed a maximum of the sine and 196 Hz showed a minimum of the sine. The quantitative magnitudes were not significant, as it could be seen that a clear fluctuating pattern occurs on the PML boundary for different frequencies.

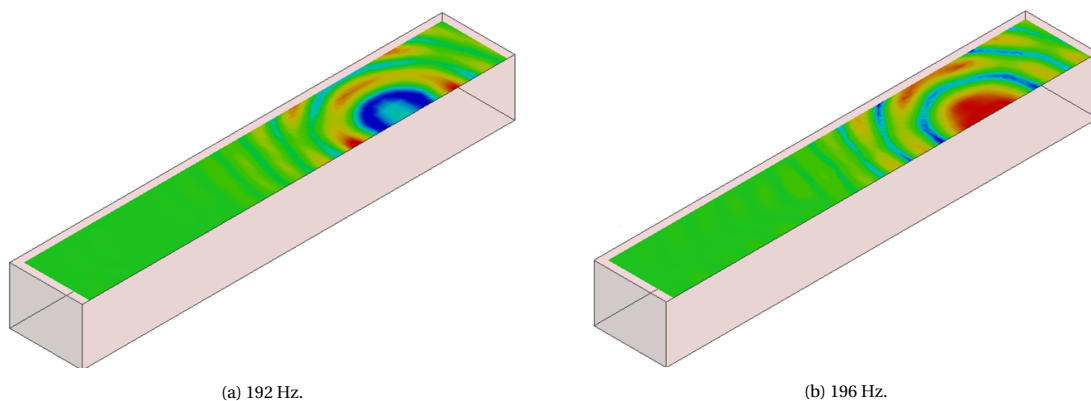


Figure 5.5: Energy Flux on the First PML layer for Different Frequencies.

Furthermore, the model was rerun with an increased amount of PML layers to judge the effect of more layers on the sinusoidal pattern. The original model had 3 PML layers and the new run had 5 PML layers. The results showed that an increase in the amount of PML layers did not result in a significant reduction of the amplitude of the sinusoidal pattern. The average values were the same for both the original model and the model with additional PML layers, however, a phase shift of the sinusoidal pattern was observed. The results are found in Appendix C.

It could be possible for the artefact to be resolved at higher PML layer numbers, but that would be contradictory to the statement of Howard and Cazzolato (2015) to use a minimum amount of 3 – 4 PML layers. It is thus concluded that the reflections of the first PML layer are the main contributing factor to the sinusoidal pattern in the data. Reflections are always present in computational models and can never be completely eliminated.

The total thickness of the total PML region has a minimum requirement, however, it is also possible for a very large PML layer to raise problems. Figure 4.5 showed acceptable results at low frequencies (below approximately 80 Hz) and the sinusoidal pattern artefact emerged above 80 Hz. The PML region thickness requirement was governed by the lowest frequency and the corresponding longest wavelength. The requirement set the minimum PML region thickness to a quarter of the wavelength. For high frequencies and shorter wavelengths, the chosen PML region thickness was significantly overdesigned. To solve this, a frequency-dependent geometry could be used that reduces the thickness of the PML region for higher frequencies.

Furthermore, viscosity in the acoustic fluid domain was set to zero to eliminate frequency-dependent damping of the domain. The goal of this was that far-field data could be transferred back to source level data with the same calculation for all frequencies. No damping in the fluid could result in a build-up of reflected waves. The application of a small amount of damping within the acoustic domain could potentially counter

said build-up of reflected waves.

Finally, an additional layer with high attenuation could be utilised in addition to the PML region to minimize boundary effects. This layer is called a 'false bottom'.

5.2.2. Domain Size

The domain size was shown to influence the sinusoidal pattern of the results. An additional model was created with an increased acoustic domain from 40 m to 80 m. The difference in results between the large and small model is plotted in Figure 5.6. The results are the far-field acoustic pressures at 180 degrees. It was observed that a larger domain reduced the amplitude and the period of the sinusoidal pattern.

Additionally, the average was increased since the wave energy was more concentrated in the downwards direction compared to the smaller model. The energy concentration resulted in larger far-field acoustic pressures. This effect is further elaborated upon in Section 5.6.

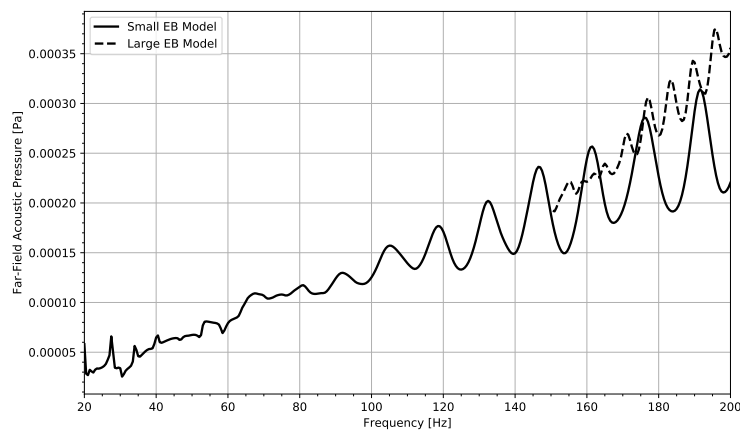


Figure 5.6: Raw Model Output to Unit Input Force for a Small Model (40 m) and a Large Model (80 m) at 180 Degrees.

5.3. Reference Data Comparison

An evaluation of the EB model without resilient mount results was made together with the reference data presented in Section 3.2.1 to check if the EB model showed proper results comparable with reality. From the data, it was expected that the machinery would induce a constant source level noise up to 200 Hz. This is shown by Figure 3.5, where the decomposed source level noise spectrum of a generic merchant ship was presented. The machinery noise in this figure was shown to be constant up to 200 Hz, from where it would gradually decline. The constant behaviour of the machinery noise was confirmed by Figure 3.6, where machinery URN was simulated. From the model results a rather constant spectrum resulted with a slight upwards trend towards the 200 Hz upper bound was found. In Figure 5.7 the EB model source level spectrum and the results from Zhang et al. (2019) are combined, it can be concluded that the data matches rather well. The EB model is most comparable to the red FE-AML line, as the modelling technique is the most analogous. The unit on the y-axis is different for both graphs, however, both are logarithmic. The change and spread in magnitudes are therefore comparable. Some observed differences are the magnitudes of the peaks below 60 Hz. Especially just below 40 Hz is a large peak in the data from Zhang et al. (2019), most likely as a result of the peak in the acceleration spectrum of the diesel generator (see Figure 3.9c). This was not accurately captured in the model of this research. The reason for this could be all forces were applied at 1 point in the EB model and the diesel generator force could have been applied at a different place within the ship where specific modes of the ship were better activated. Furthermore, the eigenmodes of the EB model could have been different than the ship from Zhang et al. (2019), resulting in peaks at different locations. Similar to what was found in Section 4.1.2, we see that the global dynamics and resonant peaks are of importance at low frequencies (below 60 Hz). At Frequencies above 60 Hz, the relative importance reduces and the spectrum more closely matches the data from Zhang et al. (2019).

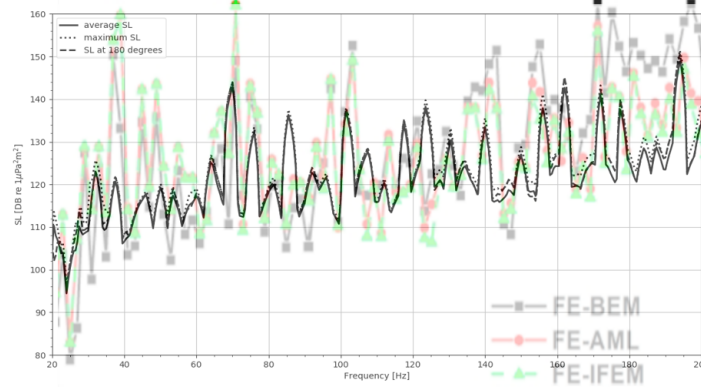


Figure 5.7: EB model Source Level Results and Results From Zhang et al. (2019) Comparison.

The expected magnitude of the machinery URN is roughly derived from Figures 3.3, 3.5 and 3.7. The merchant class ship average noise spectrum from Figure 3.3 shows a maximum source level of 173 dB re 1 $\mu\text{Pa}^2\text{m}^2$. Figure 3.5 shows that the constant machinery noise URN level is approximately 8,5 dB re 1 $\mu\text{Pa}^2\text{m}^2$ below the maximum total URN source level. A recent study performed by MacGillivray and de Jong (2021) showed that the previously used models overestimate source levels on average by 11 dB re 1 $\mu\text{Pa}^2\text{m}^2$ at 20 Hz and by -1 dB re 1 $\mu\text{Pa}^2\text{m}^2$ around 200 Hz. The standard deviation of the overestimation is approximately 10 dB, therefore the actual error could supposedly be higher or lower.

The cruising speed corresponding to the force input spectrum is unknown from the literature, however, it is known that the source level has clear dependence on the shipping speed (see Figure 5.8). In Figure 5.8, this research case best fits with the 'Bulkier' Class as it is most comparable to the merchant class from the reference case. From the figure, it can be seen that the speed differences in the 'Bulkier' subfigure show deviations of at least ± 10 dB from the mean value with outliers showing significantly larger deviations.

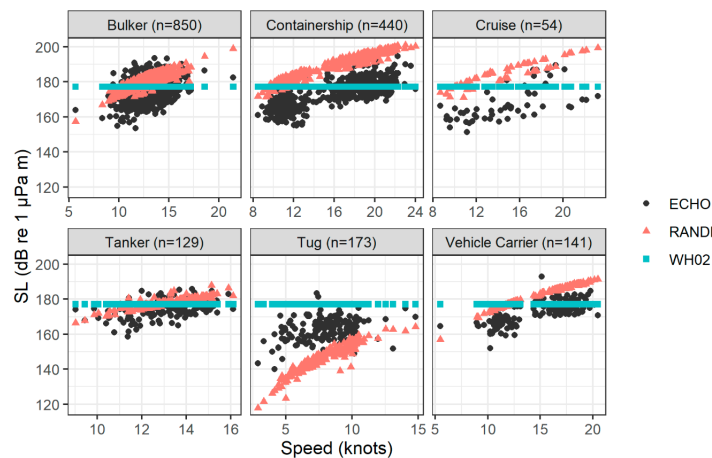


Figure 5.8: Speed Dependence of Source Level Versus Ship Type. Comparison Between RANDI and W&H Models and Echo Data Set. (MacGillivray & de Jong, 2021)

The aforementioned source level magnitudes from reference data and the corresponding spread are plotted together with the source level spectrum from the EB model in Figure 5.9. The blue band represents the range of expected average magnitudes of the source level spectrum. The dotted lines show the 1 standard deviation from the average expected source level.

Figure 5.9 clarifies that the EB model source level is lower than expected. The course of source level spectrum is verified to show the expected behaviour as it is on average parallel with the blue band. Reasons for magnitude under prediction could be as an effect of the assumptions listed in Section 3.7 as explained in Section 5.5. Furthermore, the operating conditions corresponding to the machinery force data of Zhang et al. (2019) are unknown. Forces on the ships from the data in Figures 3.2 and 3.5 could be magnitudes larger, explaining (a part of) the gap in the simulated magnitudes of the noise. Lastly, the blue band spread is

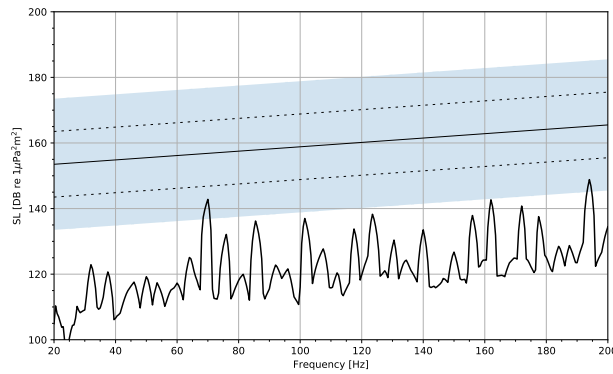


Figure 5.9: The Averaged Source Level Spectrum of the EB Model Plotted with the Expected Magnitude Range.

derived from literature based on full ship noise spectra, not limited to the machinery noise. It could be that parts of the uncertainty spread and overestimation of the RANDI and W&H models originate from cavitation or propeller vibrations noise. The effect of this would be a narrowing of the blue band and an upwards shift of the left part of the band.

5.4. Resilient Mount Modelling

The results obtained from the modelling of the resilient mount did not meet the expectations posed in Section 3.4.2. In this section, the assumptions and limitations of the mount modelling and 2-DOF schematisation are treated and an explanation of the results is given considering the assumptions and limitations.

The resilient mount was simplified to a single spring and damper unit placed underneath the machinery block. It is clear from Figures 2.4 and 3.18 that the resilient mount was significantly simplified and DOFs were eliminated by constraining the machinery movements in multiple directions.

Furthermore, the spring and damper unit was connected to the EB model via deformable remote attachment, ensuring that the force from the mount was equally divided over the input application face of the EB model. The deformable attachment was a simplification of reality that goes hand in hand with the resilient mount schematisation. The full mounting system would divide the total load via foundation beams and girders towards the hull structure of the ship. A less gradual force spreading occurred in the modelling approach of this research.

Moreover, the prescribed accelerations on the machinery block and resilient mount resulted in the resonance of the machinery mass to be missed in the Ansys runs. Through the acceleration, the displacements are prescribed. No excessive displacements are allowed in this case when the input frequency was around the resonance frequency of the machinery block and mounting system.

Lastly, the quantity of interest in this research was the acoustic pressure and source levels. Displacements of the machinery could be excessive and collide with the physical boundaries set by the ship. The mount parameters were chosen such that the static load could be carried. The corresponding static deflection was 1.7 mm, most likely not causing any issues. However, at resonant frequencies, the dynamic displacements could be excessive and it should be investigated whether these displacements could result in collision.

A force input was used in the 2-DOF schematisation as this was expected to yield more accurate results. Normalised results were obtained as those are more useful compared to absolute values since the force input has no physical meaning, as was explained Section 3.4.4. Slightly different results were obtained using the force input in the 2-DOF schematisation compared to the Ansys runs conducted with the acceleration input. This effect is noticeable when Figures 4.17a and 4.17b are compared with Figures D.5 and D.6. The stiffness dependent graph of the 2-DOF schematisation showed a larger influence of a changing stiffness on the response. This effect is most noticeable at lower frequencies.

Furthermore, Figure 4.17a shows small wiggles in the graphs indicating the presence of numerical errors in the calculation. The wiggles are of very small magnitude and were not treated any further in this research.

The 2-DOF system is used to interpret the results of the resilient mount. The findings are similar to the Ansys runs, but the 2-DOF system is easier to interpret. The frequency dependence of the results to changes in the resilient mount parameters was as expected. The stiffness of the mount had the greatest influence at lower frequencies, while damping had the greatest influence at higher frequencies. Furthermore, increasing the stiffness increased the response of the system. Interestingly, an increase in the damping of the mount increased the response of the system in contrast to the expectations.

The surface plot presented in Figure 4.18a showed a peak response of the system at a stiffness significantly higher than the base settings of the resilient mount. At higher stiffness values, an increase in the damping ratio does result in a decrease of the response. The peak in the surface graph was caused by the shift of the dominant eigenfrequency of the combined system for a higher stiffness of the mount. The eigenfrequency at the peak would be 192 Hz, the frequency at which the graph was created. For values significantly lower than the peak stiffness value, the response is decreased and an increase in damping value increases the response. This was mathematically proven to be true by the 2-DOF schematisation.

The base parameters of the resilient mount were derived from Vulkan Couplings (2012) and no detailed design was performed. It could occur that after a detailed design, the base parameters are located at a different location within Figure 4.18a leading to different parameter influences on the response. It is however not likely that the base parameter in this research would have been under-predicted by a factor of 10^3 . Subsequently, the complex stiffness of the model could not be correct. The complex stiffness was derived from the response of the base EB model to a unity load. The accuracy of the base EB model is checked against reference data in Section 5.3.

The increased response of the equivalent beam as a result of an increase in the damping of the resilient mount can best be explained by looking at transmissibility curves. A transmissibility curve shows the ratio between the input force and the transferred force of a system. In Figure 5.10 the ratio between the displacement amplitudes \tilde{U}_1 and \tilde{U}_2 are plotted to conclude that the equivalent beam can be seen as a rigid support to keep the explanation concise.

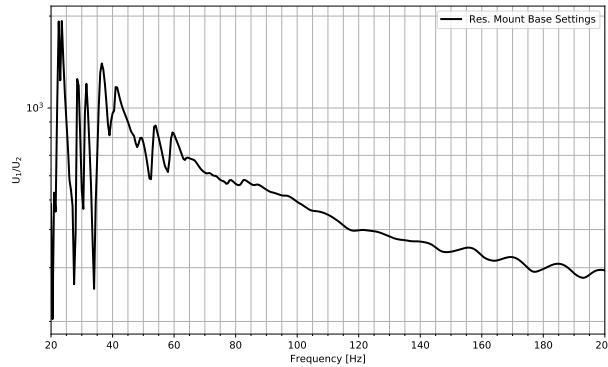


Figure 5.10: The ratio between \tilde{U}_1 and \tilde{U}_2 of the 2-DOF Schematisation over the Frequency Analysis Range.

The assumption of the equivalent beam as a rigid support allows the use of the transmissibility curve of an SDOF system, given in Figure 5.11. The transmissibility curve shows the ratio between the force acting on the machinery mass and the force transmitted at the bottom of the resilient mount. The intersection point of all curves is located at $\sqrt{2}$ ((Marino, Cicirello, & Hills, 2019)). A decrease in damping causes amplification left of this point and causes isolation right of this point. The eigenfrequency of the machinery mass and resilient mount (base settings) is calculated as follows:

$$\omega_1 = \frac{1}{2\pi} \sqrt{\frac{k_1}{m_1}} = \sqrt{\frac{30 \cdot 10^6 \text{ N/m}}{20840 \text{ kg}}} = 6.04 \text{ Hz}$$

From this value of the eigenfrequency and Figure 5.11 it can be concluded that the frequency analysis range from this research is in the isolation region, right of the intersection point of all curves. The isolation part of the curve explains why the response \tilde{U}_2 increases for an increase in damping.

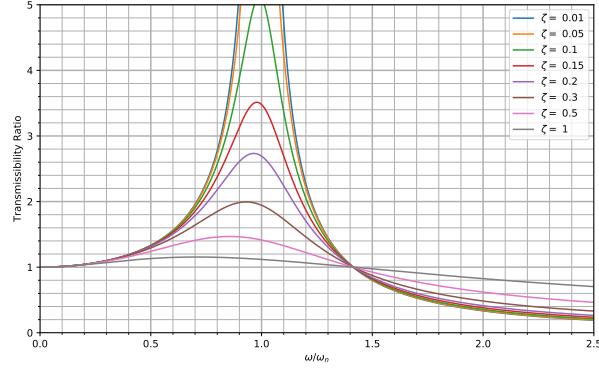


Figure 5.11: Transmissibility Curve of an SDOF System.

Li (2019) derived transmissibility curves for a 2-DOF system also showing the increased response for an increase in damping value right of the intersection point. The shape of the curves and the point of intersection is dependent on the mass ratio $\frac{m_1}{m_2}$ and the eigenfrequency ratio $\frac{\omega_1}{\omega_2}$. The mass ratio (μ) is undoubtedly lower than 1. The eigenfrequency ratio is more complex as the equivalent beam has multiple eigenfrequencies. The dry dominant eigenfrequency of the equivalent beam is located around 2.5 Hz (see Table 3.5) and the wet dominant eigenfrequency is lower due to the added mass effect of the liquid. The eigenfrequency ratio (β) is therefore at least larger than 2. The values of μ and β result in an intersection point of the transmissibility graph at approximately 2 or lower (see Appendix E). This means that the frequency analysis range used in this research is located entirely in the isolation area of the transmissibility curve of a 2-DOF system, verifying that an increase in damping results in an increase in response \tilde{U}_2 . Furthermore, this confirms that the assumption of a rigid support is acceptable and that Figure 5.11 can be used as explanation of the increased response to an increase in resilient mount damping.

The transmissibility curves of the 2-DOF schematisation with different parameters are plotted to verify that vibration isolation occurs in the 2-DOF schematisation and thus the EB model. The transmissibility of the 2-DOF schematisation is defined as the ratio between the force transmitted by the resilient mount to mass m_2 (\tilde{F}_2) and the input force applied to mass m_1 (\tilde{F}_1). The transmissibility is computed using:

$$\text{Transmissibility} = \frac{\tilde{F}_2}{\tilde{F}_1} \quad (5.1)$$

$$\tilde{F}_2 = k_1(\tilde{U}_1 - \tilde{U}_2) + c_1(\tilde{V}_1 - \tilde{V}_2) \quad (5.2)$$

Where \tilde{U} and \tilde{V} are respectively the displacements and velocities of the masses, k_1 is the stiffness of the resilient mount and c_1 is the damping of the resilient mount.

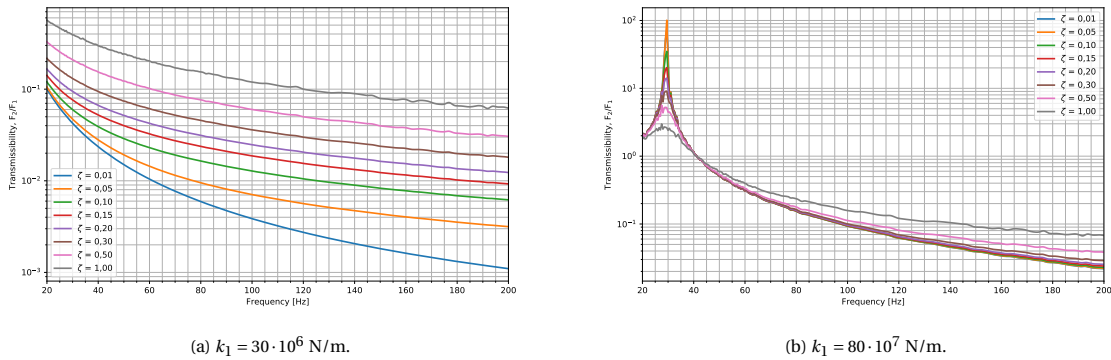


Figure 5.12: Transmissibility of the 2-DOF Schematisation for Different Mount Stiffness Values.

Figure 5.12a shows the transmissibility of the 2-DOF schematisation with the original resilient mount parameters. The shape of the curves and the relation between the transmissibility and the damping closely resemble the isolation region from Figure 5.11. Increasing the stiffness k_1 of the resilient mount was expected to shift the intersection point to the right. Figure 5.12b indeed shows the shift to the right of the intersection point when the mount stiffness was increased to $80 \cdot 10^7$ N/m. Furthermore, Figure 5.12b clearly showed the pattern of the 1-DOF transmissibility graph, where the damping reduced the transmitted force left of the intersection point, but increased the transmitted force right of the intersection point. This proves that the resilient mount from this research is located in the isolation range of the transmissibility graph and that vibration isolation occurs.

Finally, the normalised displacement \tilde{U}_2 for different damping values that was plotted in Chapter 4 is plotted again, this time using the increased stiffness value. Figure 5.13 shows this normalised spectrum for \tilde{U}_2 . At the low frequencies an increase in damping lead to a decrease of the response. Around the intersection point of the transmissibility graph (45 Hz) the response to a change in damping is flipped around and an increase of damping leads to an increase of the response. Figure 5.13 confirmed that a decrease in response of the model in this research is possible, but that the chosen resilient mount parameters were such that vibration isolation occurred leading to the fact that an increased mount damping increased the response of the equivalent beam model.

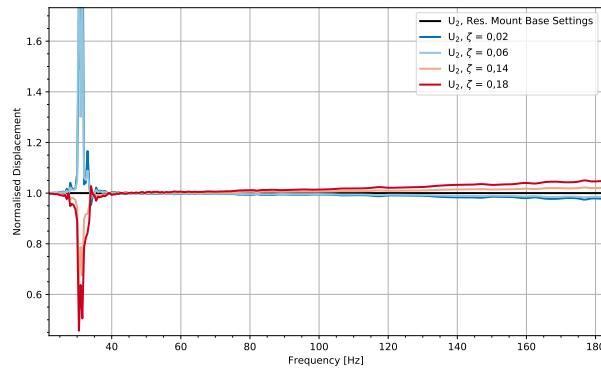


Figure 5.13: Displacement \tilde{U}_2 for Different Damping Values and a Resilient Mount Stiffness of $k_1 = 80 \cdot 10^7$ N/m Normalised to the Response with the Resilient Mount Base Damping Ratio.

5.5. Assumption Interpretation and Model Limitations

In the sections above the main contributions to the uncertainty of this research have been addressed. In this section, the remaining assumptions are touched upon and it is elaborated how these assumptions have influenced the results. Assumptions were made during the setup of the models as summarised in Section 3.7. The assumptions are deviations from reality and the effect on the results needs to be taken into account.

Pre-stress of the beam in lateral direction due to hydrostatic forces is not accounted for in the EB model. The pre-stress is expected to be compressive and is likely to increase the natural frequencies (Bai-jian, Fei, & Song, 2018). However, the relative changes in frequencies and the magnitude of the hydrostatic pressure are minimal thus barely influencing the natural frequencies. Furthermore, the source level spectrum is broad and thus a slight change in the system's natural frequencies has a negligible effect.

The prismatic characteristics used for the EB model are a simplification of reality. Described in Section 3.3.3 are the differences in terms of dynamical behaviour for the EB model and a detailed model of the Giant 5 Barge. It can be seen that the eigenfrequencies of the EB model and the barge do not match at every frequency. The influence of this on the results from the EB model is challenging to estimate. Because of the upwards error on the eigenfrequencies of the EB model compared to the barge, fewer eigenfrequencies are taken into account within the frequency analysis range. Fewer eigenfrequencies mean less excessive dynamic responses. This could thus mean that the results from the EB model are underestimating reality.

Additionally, the use of symmetry conditions in the EB model prevented modes unsymmetrical in lateral

direction to occur. The symmetry conditions imposed zero displacements and rotations of the EB cross-section on the symmetry plane that ran longitudinally across the centre of the beam. As an example, torsional modes are oftentimes not symmetrical in this direction and were thus not taken into account in the modelling.

Furthermore, local modes in the higher frequencies are not captured by the EB model and could result in a lower response than reality. Local modes are more likely to have higher amplitudes at higher frequencies compared to global modes as the local stiffness is often lower. A local mode of a ship floor compartment could excite the underlying fluid in a greater manner increasing the source level at that frequency. In the modelling approach of the EB model, the input is placed directly on top of the equivalent beam, representing the total mass and stiffness of the Giant 5 barge. Whilst, in reality, the machinery is located elsewhere within the ship where the underlying structure has a reduced local mass and stiffness compared to the ship as a whole. The response of the EB model and the effectiveness of the resilient mount thus have uncertainties.

The assumptions introduced at the input of the EB model are expected to have influenced the results. The application location, the direction and the hull connection were all assumed, as explained in Sections 3.2.3 and 3.3.5. All three assumptions influence the radiation pattern of the waves and the magnitude of the vibrations and thus the underwater radiated noise. The direct rigid hull connection is expected to have overestimated the response of the structure and the acoustic pressures as there is no energy loss. The application of the load at the top side of the EB model is expected to have caused underestimation of the URN, as the entire EB mass and stiffness are utilised in response to the acceleration input. In reality, the force is applied on the floor of the ship where the mass and stiffness of the structure separating the machinery and the fluid could be significantly lower.

Subsequently, the separate machinery component accelerations were combined into a single input. Individual components such as the engine and the generator could have different locations and a phase shift in the loading.

Finally, the machinery acceleration spectra could be as a result of some stiffness and damping on the ship of Zhang et al. (2019) instead of a infinite stiff case assumed in this research. Mount characteristics were not provided in the paper and therefore this assumption could not be eliminated.

The structural damping ratio influenced the amplitudes of the beam vibrations and magnitudes of the source level spectrum. A higher damping ratio dissipates the vibration waves along the length of the beam faster with increased distance from the force application location decreasing the URN.

The chosen fluid properties are assumed to be constant in time and in space. The result of this is that the wave speed is the same everywhere. In reality, these properties can change in time and space, altering the wave speed.

The Giant 5 Barge model is combined with machinery acceleration data from Zhang et al. (2019). This is done because limited data is available for this research. The classes of both ships are slightly different but were assumed to be comparable such that the data could be combined. This combination resulted in the creation of a fictitious ship that is not representing a real-world case. The machinery acceleration magnitudes could be different, influencing the final magnitudes of the acoustic pressures and the source level.

During the modelling of an infinite domain, the results should remain similar for adjustments of the computational domain size. Effects of the computational boundaries are unwanted but are hardly ever entirely eliminated. In this research, the results did change for an increase of the model dimensions as was seen in Figure 5.6. Unfortunately, computational limits were reached and larger, more detailed domains were not possible.

5.6. Computational Limits

Besides limitations introduced through the modelling approach described in this chapter, additional limits were reached in computational terms. The limits explained in this section can be related to time and memory. The number of elements of a numerical model significantly increases the total time needed to complete the calculation and the total result file size. The model used in this research consisted of approximately 600.000 elements with a computational time of around 30 hours and a result file size of 70 GB.

5.6.1. Mesh Size

The mesh size requirement is dependent on the highest frequency analysis. For a certain frequency, the mesh requirement is at least 6 quadratic elements per wavelength (see Section 3.3.6). This lower bound for the requirement was used in the EB model to achieve decent accuracy and reasonable computational times. This mesh size could show to be inaccurate towards the higher frequencies as the requirement is closely met. A smaller element size would allow computations at higher frequencies, but would significantly increase the total computational time and result file size.

5.6.2. Domain Size

Similar to the mesh size, the size of the domain was determined via requirements as set by Howard and Cazzolato (2015). From Figure 5.6 it was clear that the results deviated for a larger domain, indicating that the domain size influenced the results of the model. This is an unwanted effect in the modelling of infinity and is a limitation of the research. A larger domain size significantly increased the total amount of elements leading to very long computational times and large result files.

5.6.3. Frequency Analysis Range and Frequency Resolution

The lower frequency analysis bound was governed by the domain size and the upper bound was governed by the mesh size. Both were limited due to the computational time and memory. Furthermore, an increase of frequency resolution on the analysis frequency range would have increased the computational time and result file size leading to unmanageable models.

5.7. Result Interpretation, Scientific Impact and Practical Applications

The results obtained in this research have uncertainties coming from assumptions and from limitations raised through time constraints and data availability. The individual assumptions and limitations have been described in this chapter, but a combined consensus on the reliability and usefulness of the research and the results is given in this section.

Many assumptions affect the final results that are not easily quantified, let alone the combined effect of all assumptions on the results. It is clear that the assumptions significantly influence the results, as was for example seen from Figure 5.6. The effects are prominent in the pressure results, however, on the source level Decibel scale the effects are significantly reduced. The combined effect of the assumptions on the results of the base EB model was shown in Figure 5.9 to be significant. Furthermore, the acceleration input of the resilient mount Ansys runs overestimated the source levels as was seen from Figure 5.3. This overestimation is thought to especially occur at the infinite stiff case representing the case with no mount. The relative decrease in source level of the mitigation methods is thought to be more accurate, as the relative results both have the over-estimation due to the acceleration input. The normalised results of the 2-DOF schematisation are considered useful since the force input was used, eliminating the error from the acceleration input. Furthermore, the normalised results do not rely on the accuracy of the absolute values of the model response but on the changes of the model response compared to a change in model parameters.

The parameter study indicated that interesting dependencies of the URN on the damping and stiffness coefficient can occur. The design of a resilient mount should be approached with caution and no intuitive decisions should be made.

Subsequently, this research can strengthen the claims made by AQUO-SONIC (2015) that resilient mounts can achieve noise reduction of 20 – 40 dB re $1 \mu\text{Pa}^2\text{m}^2$. Although this research overestimated these numbers, there are good reasons for this. The claim that it will be more efficient at higher frequencies is also supported by this study, as the damping had a significantly larger impact at higher frequencies.

Besides the obtained results, an efficient methodology is presented with which an extensive parameter study can be conducted. the underwater radiated noise (URN) model takes a very long time to run due to the large number of elements needed. The proposed method requires the large model to be run only once, after which the characteristics of the model are extracted and adjustments can be analysed without running the large model again. This approach gives design freedom and speeds up the process of testing and designing mitigation methods for the URN.

In this research, challenges have been identified in the modelling of the URN of ships. In Chapter 6, rec-

ommendations for further research are proposed in order to tackle the challenges and to improve the overall modelling of URN of ships.

The effect of a resilient mount was seen to be effective in reducing the structure-borne URN of the machinery of a ship. However, the total URN of a ship is a combination of multiple noise-producing mechanisms, see Figure 3.5. Due to the logarithmic scale of the source level, a reduction of a part of the URN could have limited effects on the total URN, as was explained in Section 3.2.1. It is thus advised that all significant noise generation mechanisms should be treated for the reduction of the total URN of a ship. The reduction of the machinery structure-borne URN is a small piece of the total problem. At lower speeds or standstill, the machinery noise is expected to be the largest component, increasing the influence of mitigation on the total underwater radiated noise.

The noise received by a marine mammal is the combined of URN from a large number of ships. The mitigation of part of the URN of one ship is not likely to significantly reduce the total noise in soundscape of the ocean. Mitigation of URN should be applied consistently to ships to obtain clear improvements.

No effect of the mitigation measures on marine mammals can be quantified. It's hard to indicate how marine mammals experience noise and how much their living environment is improved per Decibel reduction in noise. It can be concluded that the mitigation method presented in this research undoubtedly has a positive influence on marine mammals. Especially the baleen whales and grey seal listed in Table 2.1 are influenced by the reduction in noise at frequencies below 200 Hz, as the analysis frequency range of this research is used by those species. The effect on higher frequencies could be estimated from the results of this research but no model results can be provided.

6

Conclusion and Recommendations

In this study, the effectiveness of mitigation methods in reducing structure-borne underwater radiated machinery noise from ships was researched. In this chapter, the results are concluded by answering the research questions posed in Chapter 1. Furthermore, the main limitations of the research are highlighted and the contributions of this research to existing knowledge are indicated. Finally, future continuations and recommendations for further research are given.

The answers to the research questions are:

In what frequency bands is most harm caused to marine mammals?

Different marine mammals communicate at different frequency bands and different sound levels. Every specie experiences its own type of nuisance due to URN from ships and therefore it is complicated to indicate a single frequency band that is governing for the harm caused to marine mammals by URN. Furthermore, harm was assumed to occur at frequencies utilised by marine mammals, since at those frequencies auditory masking and acoustic responses take place. It is physically true that low-frequency signals travel further in the ocean and as a result, ambient noise is present in the soundscape of the ocean at around 10 – 300 Hz. This was the range that was focused on in this research. Combined with modelling limits, the analysis frequency range was 20 – 200 Hz.

How can the ship and its machinery be modelled for the purpose of computing the URN in the right frequency bands?

The ship was modelled as an equivalent beam. The equivalent beam is a beam-shaped solid with similar global properties to a ship. The machinery was modelled as an input force directly on the equivalent beam. This approach showed that the ship could not be modelled as an equivalent beam for computing the specific eigenmodes. However, at frequencies above 40 Hz, the effect of eigenmodes became less relevant. The average slope and distribution of the source level spectrum above 40 Hz showed good accordance with the literature. The average magnitudes were shown to have been under-predicted by the equivalent beam model according to the available reference data.

What mitigation methods exist to attenuate the vibrations from onboard machinery?

Different mitigation methods exist for the mitigation of structure-borne machinery URN of ships. In this research, it was concluded employing a literature study that resilient mounts are the most promising mitigation method. Resilient mounts were assessed in the remainder of the research.

How can the selected mitigation methods be modelled for the purpose of computing the effects on the URN?

The resilient mount was first modelled using a spring-damper element in Ansys. The machinery was modelled as a rigid mass block on top of the spring-damper element and acceleration input was used on the machinery block. The damping and stiffness of the mount could be adjusted to see the effect of changing

parameters on the URN. Additionally, a 2-DOF schematisation of the machinery, resilient mount and the underlying model was created in which the underlying model was schematised as a dynamic spring. This schematisation allowed for a faster and more extensive study of the resilient mount parameters.

What is the influence of changing parameters of the mitigation methods on the URN?

The parameter study of the resilient mount showed interesting results. For an increase of the damping, the response of the system increased. This was counter-intuitive but could be explained with transmissibility curves indicating that the model in combination with the frequency analysis range caused vibration isolation of the machinery. During the vibration isolation, an increase of the damping increased the force transmitted to the equivalent beam and thus increased the response of the system. This effect was enhanced for higher frequencies.

A change in stiffness did have the expected effect on the URN. An increase of the stiffness increased the response of the system. The effect was most noticeable at the lower frequencies and almost negligible at the highest frequencies.

The results from this research showed that machinery structure-borne noise can be reduced by 45 – 65 dB re $1 \mu\text{Pa}^2\text{m}^2$ over the frequency analysis range of 20 – 200 Hz. At the lower frequencies, the reduction oscillated over the frequencies. From 60 Hz and above a linear SL reduction was observed that gradually lessened for higher frequencies. A change of the damping ratio of the resilient from 0.18 to 0.02 increased the SL reduction from 45 dB re $1 \mu\text{Pa}^2\text{m}^2$ to 60 dB re $1 \mu\text{Pa}^2\text{m}^2$. Furthermore, the normalised resilient mount parameter study gave clear insights into the parameter sensitivities and responses of the system. It was shown that the resilient mount does not show the expected response to a change in mount damping. The accuracy of the absolute results is subjected to uncertainties resulting from assumptions and limitations.

Acceleration input was used to assess the absolute decrease in URN for the resilient mount. The acceleration input was shown to have overestimated the 'no-mount' case used for comparison with cases including the resilient mount. The total reduction of URN of the resilient mount could thus have been over predicted. Furthermore, an effect of the PML region and the domain size on the results was present in the models. This effect influenced the magnitudes of the results, but could not be eliminated due to the computational limits reached. Lastly, limited model input data and reference data were available. The result magnitudes were obtained and compared with limited data in order to obtain a judgement on the accuracy of the model.

Taking these limitations into account, the results obtained in this research should be interpreted with caution. The results can support claims made by literature that a resilient mount can reduce structure-borne machinery noise by 20 – 40 dB re $1 \mu\text{Pa}^2\text{m}^2$ and that more reduction is achieved at the higher frequencies.

The effect of the application of the resilient mount on marine mammals was hard to quantify. The structure-borne machinery URN is a part of the total URN of a ship. Due to the logarithmic relation of the noise, the reduction of one part could have very limited effects. Furthermore, the total soundscape in the ocean is formed by the combined noise of many ships. Moreover, the relation between the perceived nuisance of marine mammals and the URN levels is hard to indicate. The effect is undoubtedly positive but could be negligible in the bigger picture. At low speeds and close distances, the machinery URN is governing and the influence of URN from other ships is reduced. In those cases, the reduction of structure-borne machinery URN with resilient mounts could be expected to be the most positive for marine mammals.

The first steps towards the modelling of mitigation methods for underwater radiated noise have been presented in this research. Various areas of this research can be improved upon to obtain more accurate results. Furthermore, additions to this research could prove to be interesting. The following recommendations for further research are proposed, sorted on importance first:

1. Limited input and reference data were available for the assembly of the models and for the judgement of the result accuracy. Furthermore, data were obtained from various literature sources. In reality, ships of the same class, size and power could show significantly different URN spectra. It would be interesting to obtain model input data and noise measurements of a real ship. Only with a real reference ship including all the necessary data, a full assessment on the accuracy of the models can be done;
2. The computational limits of the models were reached, limiting the frequency analysis range and introducing unwanted artefacts in the results. It would be interesting to look into the scaling of the model

to reduce the number of computational elements. Furthermore, a frequency-dependent mesh and domain size could be researched to save computational time and to resolve PML layer issues. Lastly, more frequency analysis points around peak responses and peak input spectra values could be used to more closely inspect the behaviour around these peaks;

3. In this research only resilient mounts were modelled. Although the resilient mount proved to be the most promising from literature, it showed interesting and counter-intuitive results. Other mitigation methods (such as tuned mass dampers) could also show interesting results that are worth researching. Moreover, the 2-DOF schematisation allows for quick adjustments of the modelled mitigation method. It can be interesting to look at non-linear dampers applied to the resilient mount;
4. The equivalent beam model was partly tuned to match the eigenmodes of the reference ship. From the results, it became clear that at higher frequencies the individual eigenmodes are not important. The spectrum showed a more constant behaviour and peaks did not occur. It could be interesting to tune the model to match the desired source level spectrum, after which mitigation measures can be applied;
5. For the modelling of the mitigation of URN to become applicable during the design phase of a new ship, it should be verified that the modelling approach applies to multiple cases and to new cases without reference data. More research on creating a generic case or model is thus needed.
6. This research is theoretical and the results should be used with caution. Practical aspects are to be checked before real-world application, such as physical constraints of the machinery, specific eigenfrequencies and interactions, and available resilient mount characteristics.

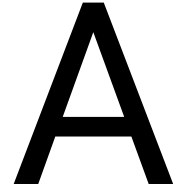
References

- Abrahamsen, K. (2012). *The ship as an underwater noise source*. doi: 10.1121/1.4772953
- Ainslie, M., de Jong, C., Dol, H., Blacqui re, G., & Marasini, C. (2009). Assessment of natural and anthropogenic sound sources and acoustic propagation in the north sea.
- Ainslie, M. A., & de Jong, C. A. (2016). Sources of underwater sound and their characterization. *Advances in Experimental Medicine and Biology*, 875, 27-35. Retrieved from <https://www.ncbi.nlm.nih.gov/pubmed/26610941> doi: 10.1007/978-1-4939-2981-84
- Alexandrov, O. (2007). *Finite element sparse matrix*.
- ANSYS. (2021). *Theory reference* (Vol. Release 2021 R2).
- AQUO. (2015). *Assessment of the solutions to reduce underwater radiated noise*. Retrieved from http://www.aquo.eu/downloads/AQUO_D5.3_Assessment_URN_reduction_rev1.0.pdf
- AQUO-SONIC. (2015). Guidelines for regulation on uw noise from commercial shipping.
- Arveson, P. T., & Vendittis, D. J. (2000). Radiated noise characteristics of a modern cargo ship. *The Journal of the Acoustical Society of America*, 107(1), 118-129. Retrieved from <https://www.ncbi.nlm.nih.gov/pubmed/10641625> doi: 10.1121/1.428344
- Audoly, C., Gaggero, T., Baudin, E., Folegot, T., Rizzuto, E., Salinas Mullor, R., ... Kellett, P. (2017). Mitigation of underwater radiated noise related to shipping and its impact on marine life: A practical approach developed in the scope of aquo project. *IEEE Journal of Oceanic Engineering*, 42(2), 373-387. doi: 10.1109/joe.2017.2673938
- Audoly, C., & Rousset, C. (2014). European project for achieving quieter oceans by shipping noise footprint reduction. *The Journal of the Acoustical Society of America*, 135(4), 2299-2299. doi: 10.1121/1.4877560
- Auf, M. (2020). Hull vibration analysis of a small multipurpose fishing vessel from newfoundland and labrador.
- A ıkg z, A. (2019). *Bending stress analysis and fatigue life estimation of involute spur gears by finite element method (fem)*.
- Bai-jian, T., Fei, W., & Song, C. (2018). Effect of prestress force on natural bending frequency of external prestressed steel beams. *The Open Civil Engineer Journal*, 12, 62-70.
- Buiten, J., & De Regt, M. (1987). *Handboek voor de lawaaibeheersing aan boord van schepen*.
- ClearSeas. (2020). *Underwater noise and marine mammals*. Retrieved from <https://clearseas.org/en/underwater-noise/>
- Colom s, O. (2020). *Introduction to computational dynamics for offshore structures: 4.1 introduction to finite elements* [Lecture slides]. TU Delft. Retrieved from <https://www.brightspace.tudelft.nl>
- Cremer, L., Heckl, M., & Petersson, B. (2005). *Structure-borne sound*. Springer Berlin Heidelberg New York.
- Daihatsu Diesel. (2021). *Propulsion systems: 6dkm-26e*. Retrieved from <http://www.dhtd.co.jp/en/products/marine/propulsion/6DKM-26e.html>
- Dalmont, J. P. (2001). Acoustic impedance measurement, part i: A review. *Journal of Sound and Vibration*, 243(3), 427-439. doi: 10.1006/jsvi.2000.3428

- Dassault Systemes. (2022). *Viscous damping ratios for different systems and materials*. Retrieved from http://help.solidworks.com/2022/english/SolidWorks/cworks/r_viscous_damping_ratios.htm?verRedirect=1
- de Jong, C. A. F. (2009). Characterization of ships as sources of underwater noise. *NAG/DAGA International Conference on Acoustics*.
- Erbe, C., Marley, S. A., Schoeman, R. P., Smith, J. N., Trigg, L. E., & Embling, C. B. (2019). The effects of ship noise on marine mammals—a review. *Frontiers in Marine Science*, 6. doi: 10.3389/fmars.2019.00606
- Gangemi, P. J. (2015). Attenuation of the structural and acoustic responses of a submerged hull.
- Hambric, S. A. (2006). Structural acoustics tutorial—part 1: Vibrations in structures. *Acoustics Today*, 2(4). doi: 10.1121/1.2961142
- Hambric, S. A., & Fahnlne, J. B. (2007). Structural acoustics tutorial—part 2: Sound—structure interaction. *Acoustics Today*, 3(2). doi: 10.1121/1.2961152
- Hansen, C. H. (2001). *Fundamentals of acoustics*.
- Heenehan, H., Stanistreet, J. E., Corkeron, P. J., Bouveret, L., Chalifour, J., Davis, G. E., ... Van Parijs, S. M. (2019). Caribbean sea soundscapes: Monitoring humpback whales, biological sounds, geological events, and anthropogenic impacts of vessel noise. *Frontiers in Marine Science*, 6. doi: 10.3389/fmars.2019.00347
- Herve, D., Wen, H., Wu, J., Amuaku, R., & Li, Z. (2018). Study on noise and vibration prediction and its reduction design in ro-ro passenger ship. *International Journal of Contemporary Applied Researches*.
- Hildebrand, J. A. (2009). Anthropogenic and natural sources of ambient noise in the ocean. *Marine Ecology Progress Series*, 395, 5-20. doi: 10.3354/meps08353
- Hovem, J. (2013). Ray trace modeling of underwater sound propagation. In *Modeling and measurement methods for acoustic waves and for acoustic microdevices* (chap. Chapter 23). doi: 10.5772/55935
- Howard, C. Q., & Cazzolato, B. S. (2015). *Acoustic analyses using matlab and ansys*. Taylor and Francis Group, LLC.
- Hsueh, W. J., & Lee, Y. (1994). A hydraulic absorber for wideband vibration reduction in ship hulls. *Journal of Offshore Mechanics and Arctic Engineering*, 116, 43-48.
- Hsueh, W. J., & Lee, Y. (1995). Design of bow absorber for vibration hull girders. *Journal of The Society of Naval Architects of Japan*, 117, 305-311.
- International Maritime Organisation. (2014). Guidelines for the reduction of underwater noise from commercial shipping to address adverse impacts on marine life.
- ITTC. (2017). *Guideline: Underwater noise from ships, full scale measurements*.
- Jansen, E., & de Jong, C. (2017). Experimental assessment of underwater acoustic source levels of different ship types. *IEEE Journal of Oceanic Engineering*, 42(2), 439-448. doi: 10.1109/joe.2016.2644123
- Kakinouchi, T., Asano, T., Tanida, K., & Takahashi, N. (1992). Active mass damper demonstration for ship vibration reduction. *Naval Engineers Journal*, 46-52.
- Kirkup, S. (2007). *The boundary element method in acoustics*.
- Kozaczka, E. (2000). Underwater ship noise.
- Kudu, F. N., Uçak, S., Osmancikli, G., Türker, T., & Bayraktar, A. (2015). Estimation of damping ratios of steel structures by operational modal analysis method. *Journal of Constructional Steel Research*, 112, 61-68. doi: 10.1016/j.jcsr.2015.04.019
- Köykkä, M. (2016). Modeling of ship structure-borne underwater radiated noise.

- Leaper, R. (2019). The role of slower vessel speeds in reducing greenhouse gas emissions, underwater noise and collision risk to whales. *Frontiers in Marine Science*, 6. doi: 10.3389/fmars.2019.00505
- Li, Z. (2019). Vibration transmissibility of two-dof vibrating systems.
- MacGillivray, A., & de Jong, C. (2021). A reference spectrum model for estimating source levels of marine shipping based on automated identification system data. *Journal of Marine Science and Engineering*, 9(4). doi: 10.3390/jmse9040369
- Marino, L., Cicirello, A., & Hills, D. A. (2019). Displacement transmissibility of a coulomb friction oscillator subject to joined base-wall motion. *Nonlinear Dynamics*, 98(4), 2595-2612. doi: 10.1007/s11071-019-04983-x
- Metrikine, A., & Tsouvalas, A. (2020). *CIE4140: Dynamics of structures* [Lecture slides]. TU Delft. Retrieved from <https://www.brightspace.tudelft.nl>
- Mohl, B., Wahlberg, M., Madsen, P. T., Miller, L. A., & Surlykke, A. (2000). Sperm whale clicks: directionality and source level revisited. *J Acoust Soc Am*, 107(1), 638-48. Retrieved from <https://www.ncbi.nlm.nih.gov/pubmed/10641672> (Mohl, B Wahlberg, M Madsen, P T Miller, L A Surlykke, A eng Comparative Study Research Support, Non-U.S. Gov't J Acoust Soc Am. 2000 Jan;107(1):638-48. doi: 10.1121/1.428329.) doi: 10.1121/1.428329
- National Research Council. (2000). *Marine mammals and low-frequency sound: Progress since 1994*. Washington (DC). Retrieved from <https://www.ncbi.nlm.nih.gov/pubmed/25077255> (National Research Council (US) Committee to Review Results of ATOC's Marine Mammal Research Program Review Book) doi: 10.17226/9756
- National Research Council. (2003). *Ocean noise and marine mammals*. Washington (DC). Retrieved from <https://www.ncbi.nlm.nih.gov/pubmed/25057640> (National Research Council (US) Committee on Potential Impacts of Ambient Noise in the Ocean on Marine Mammals Review Book) doi: 10.17226/10564
- Nieukirk, S. (2015). *Understanding ocean acoustics*. National Oceanic and Atmospheric Administration. Retrieved from <https://oceanexplorer.noaa.gov/explorations/sound01/background/acoustics/acoustics.html>
- Nilsson, A. (1978). Reduction of structure-borne sound in simple ship structures: Results of model tests. *Journal of Sound and Vibration*, 61(1), 45-60.
- OSPAR. (n.d.). *Underwater noise*. Retrieved from <https://www.ospar.org/work-areas/eiha/noise>
- Pirotta, V., Grech, A., Jonsen, I. D., Laurance, W. F., & Harcourt, R. G. (2019). Consequences of global shipping traffic for marine giants. *Frontiers in Ecology and the Environment*, 17(1), 39-47. doi: 10.1002/fee.1987
- Port of Vancouver. (2017). An evaluation of vessel quieting design, technology and maintenance options.
- Ross, D. (1976). *Mechanics of underwater noise*. Pergamon Press, Inc.
- Strietman, W., Michels, R., & Leemans, E. (2018). Measures to reduce underwater noise and beach litter.
- The International Maritime Organisation. (2014). Noise from commercial shipping and its adverse impacts on marine life.
- Veirs, S., Veirs, V., Williams, R., Jasny, M., & Wood, J. (2018). A key to quieter seas: half of ship noise comes from 15a key to quieter seas: half of ship noise comes from 15fleet. doi: 10.7287/peerj.preprints.26525v1
- Vulkan Couplings. (2012). Resilient mounts: Technical data.
- Wales, S. C., & Heitmeyer, R. M. (2002). An ensemble source spectra model for merchant ship-radiated noise. *The Journal of the Acoustical Society of America*, 111(3), 1211-31. Retrieved from <https://www.ncbi.nlm.nih.gov/pubmed/11931298> doi: 10.1121/1.1427355

- Williams, R., Veirs, S., Veirs, V., Ashe, E., & Mastick, N. (2019). Approaches to reduce noise from ships operating in important killer whale habitats. *Mar Pollut Bull*, 139, 459-469. Retrieved from <https://www.ncbi.nlm.nih.gov/pubmed/29983160> (Williams, Rob Veirs, Scott Veirs, Val Ashe, Erin Mastick, Natalie eng Review England Mar Pollut Bull. 2019 Feb;139:459-469. doi: 10.1016/j.marpolbul.2018.05.015. Epub 2018 Jul 6.) doi: 10.1016/j.marpolbul.2018.05.015
- Wittekind, D., & Schuster, M. (2016). Propeller cavitation noise and background noise in the sea. *Ocean Engineering*, 120, 116-121. doi: 10.1016/j.oceaneng.2015.12.060
- Yanhe, S., Xuhong, M., Chengshun, L., & Zhigang, L. (2019). Vibration characteristic analysis and control of hospital ship.
- Zhang, B., Xiang, Y., He, P., & Zhang, G. J. (2019). Study on prediction methods and characteristics of ship underwater radiated noise within full frequency. *Ocean Engineering*, 174, 61-70. doi: 10.1016/j.oceaneng.2019.01.028
- Zienkiewicz, O., Taylor, R., & Zhu, J. (2005). *The finite element method: Its basis and fundamentals* (Sixth edition ed.). Elsevier Butterworth-Heinemann.



Damping Formulation of Ansys

The structural damping matrix for a full harmonic analysis is derived as follows (see [ANSYS \(2021\)](#) p. 683):

$$\begin{aligned} [C] = & \alpha[M] + \left(\beta + \frac{g}{\Omega}\right)[K] + \sum_{i=1}^{N_{ms}} \alpha_i^m [M_i] + \sum_{i=1}^{N_{ms}^{MD}} \sum_{k=1}^{N_{sa}} \alpha_p [M_k]_i \\ & + \sum_{j=1}^{N_m} \left(\beta_j^m + \frac{m_j}{\Omega} + \frac{g_j^E}{\Omega} \right) [K_j] + \sum_{j=1}^{N_{ms}^{MD}} \sum_{n=1}^{N_{sb}} \beta_q [K_n]_j \\ & + \sum_{k=1}^{N_c} [C_k] + \sum_{m=1}^{N_v} \frac{[K_m]}{\Omega} + \sum_{l=1}^{N_g} [G_l] + \frac{1}{\Omega} \sum_{k=1}^{N_c} [K_k^*] \end{aligned}$$

The fluid damping matrix is derived as follows (see [ANSYS \(2021\)](#) p. 244):

$$[C_F] = \bar{\rho}_0 \iiint_{\Omega_F} \frac{4\mu}{3\rho_0^2 c^2} [\nabla N]^T [\nabla N] dv = \text{acoustic fluid damping matrix}$$

B

Resilient Mount Ansys Settings

Details of "Longitudinal - Machinery To Multiple"

Graphics Properties	
Definition	
Material	None
Type	Longitudinal
Spring Behavior	Both
<input type="checkbox"/> Longitudinal Stiffness	30000000, N/m
<input type="checkbox"/> Longitudinal Damping	160000, N-s/m
Preload	None
Suppressed	No
Spring Length	1, m
Element APDL Name	
Scope	
Scope	Body-Body
Reference	
Scoping Method	Geometry Selection
Applied By	Remote Attachment
Scope	1 Face
Body	Machinery
Coordinate System	Global Coordinate System
Reference X Coordinate	1,875 m
Reference Y Coordinate	0, m
Reference Z Coordinate	9,5 m
Reference Location	Click to Change
Behavior	Rigid
Pinball Region	All
Mobile	
Scoping Method	Geometry Selection
Applied By	Remote Attachment
Scope	1 Face
Body	Multiple
Coordinate System	Global Coordinate System
Mobile X Coordinate	1,875 m
Mobile Y Coordinate	0, m
Mobile Z Coordinate	8,5 m
Mobile Location	Click to Change
Behavior	Deformable
Pinball Region	All

Figure B.1: Modelling Settings of the Resilient Mount Connection Element Within Ansys Mechanical.

C

Perfectly Matched Layers Discussion

This appendix shows extra information on the amount of PML layers and the corresponding far-field acoustic pressure response. The pressures are the response to a unit force.

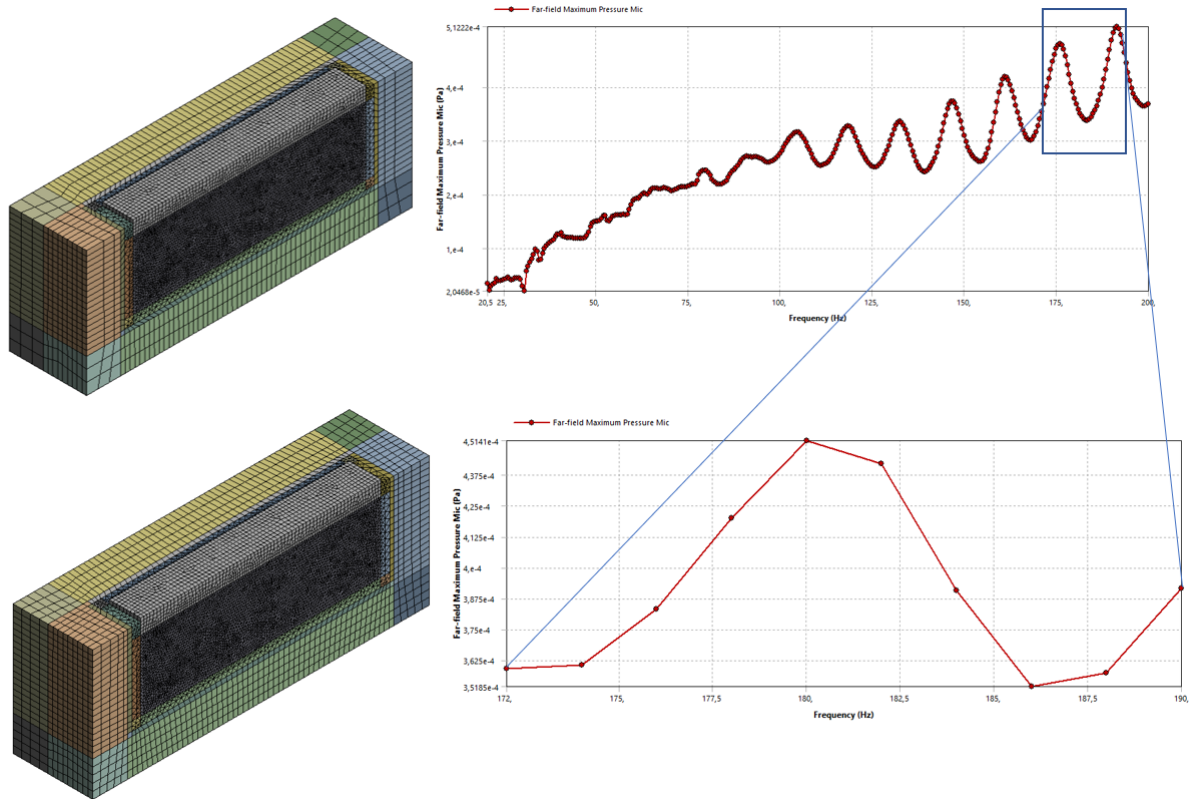


Figure C.1: Far-Field Acoustic Pressures for an Increased Amount of PML Layers.

D

Resilient Mount Parameter Study Additional Graphs

D.1. Normalised Source Level Graphs

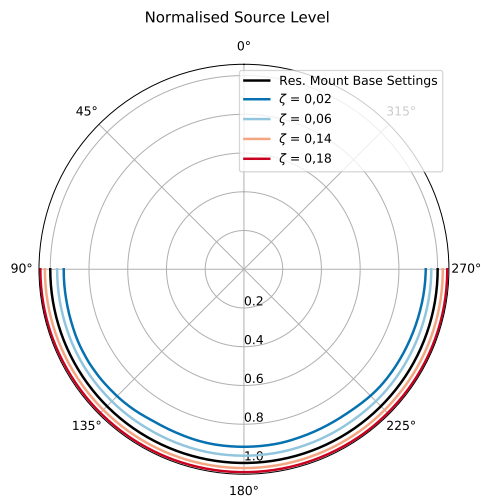


Figure D.1: Directional Source Level Pattern at 192 Hz for Different Damping Ratios Normalised to the Response with the Resilient Mount Base Settings.

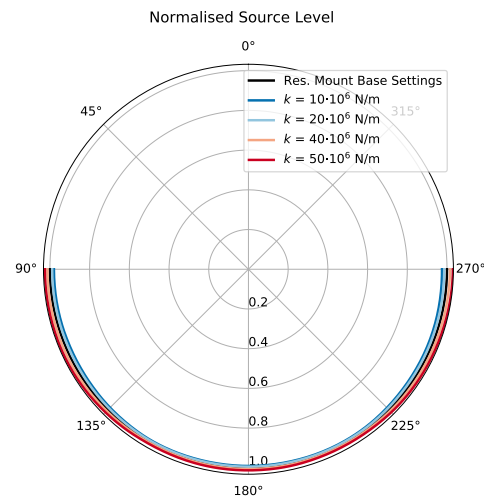


Figure D.2: Directional Source Level Pattern at 192 Hz for Different Stiffness Values Normalised to the Response with the Resilient Mount Base Settings.

D.2. Pressure Graphs

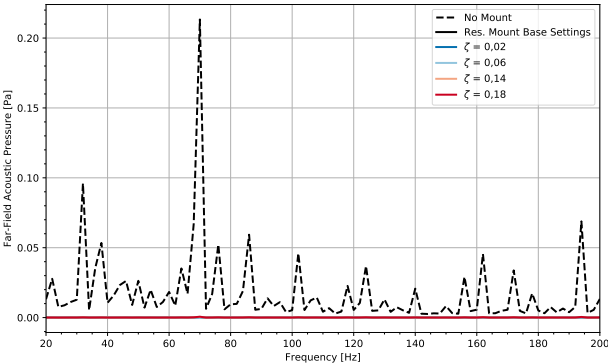


Figure D.3: Pressure Spectrum for Different Damping Ratios.

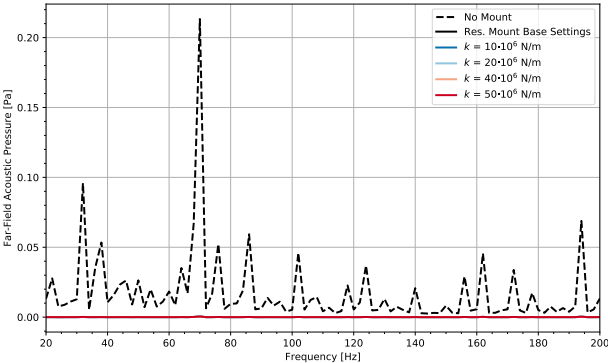


Figure D.4: Pressure Spectrum for Different Stiffness Values.

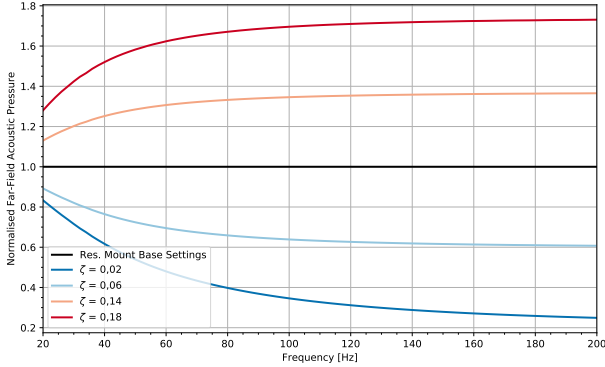


Figure D.5: Pressure Spectrum for Different Damping Ratios Normalised to the Response with the Resilient Mount Base Settings.

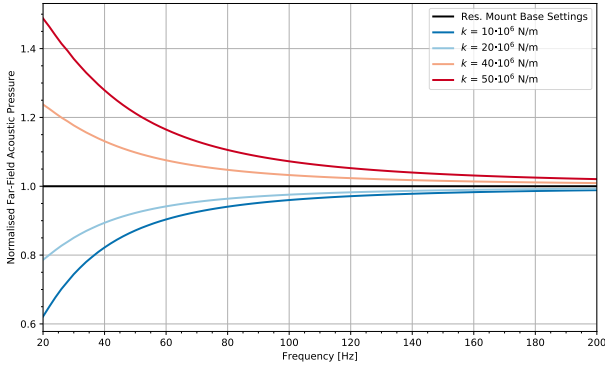


Figure D.6: Pressure Spectrum for Different Stiffness Values Normalised to the Response with the Resilient Mount Base Settings.

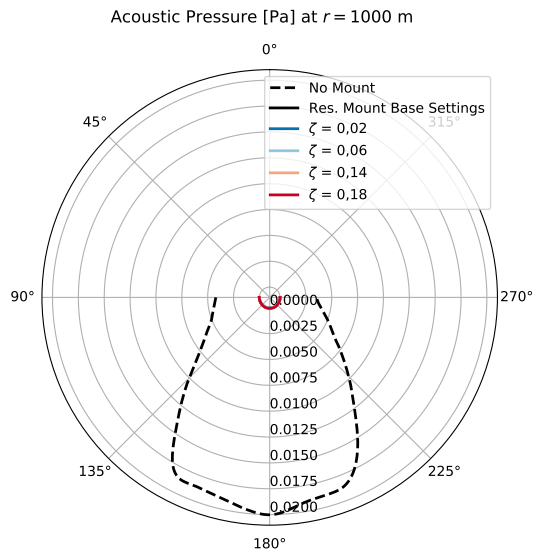


Figure D.7: Directional Pressure Pattern at 192 Hz for Different Damping Ratios.

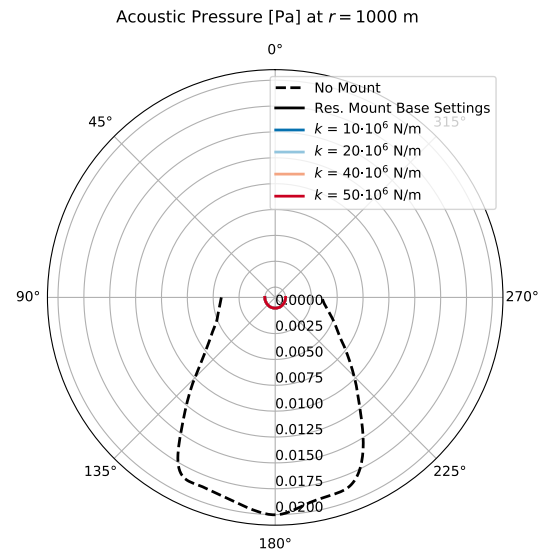


Figure D.8: Directional Pressure Pattern at 192 Hz for Different Stiffness Values.

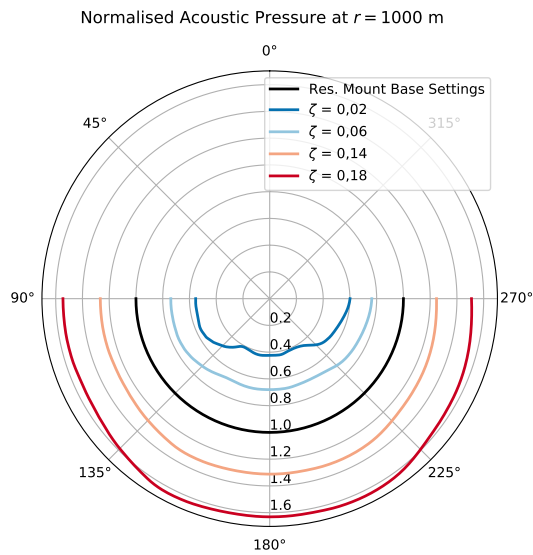


Figure D.9: Directional Pressure Pattern at 192 Hz for Different Damping Ratios Normalised to the Response with the Resilient Mount Base Settings.

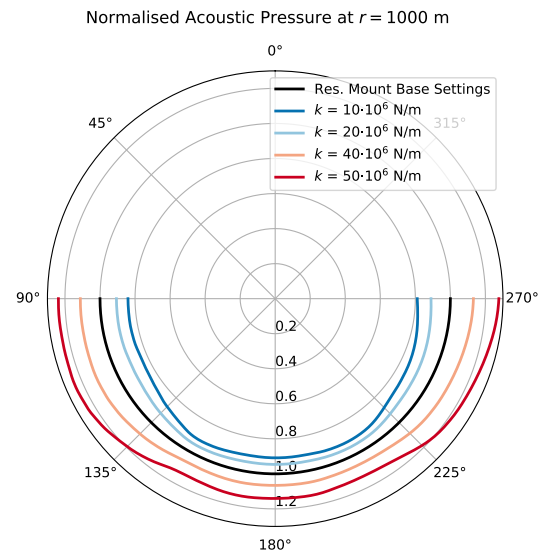
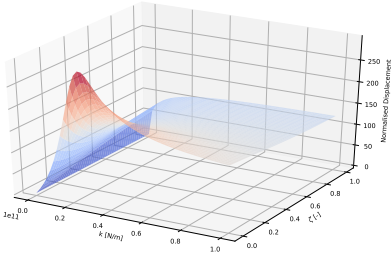
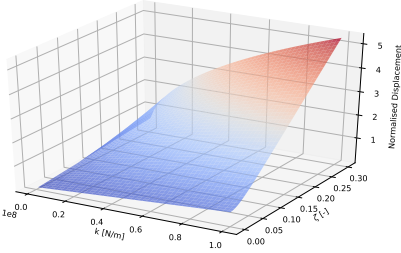


Figure D.10: Directional Pressure Pattern at 192 Hz for Different Stiffness Values Normalised to the Response with the Resilient Mount Base Settings.

D.3. 2-DOF Surface and Contour Plots Alternative Colours

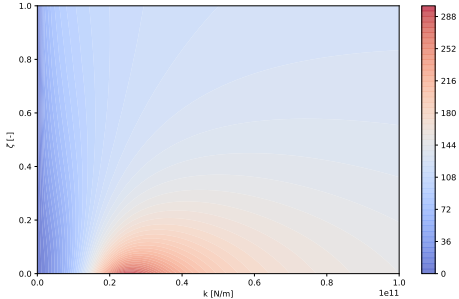


(a) In Full Range.

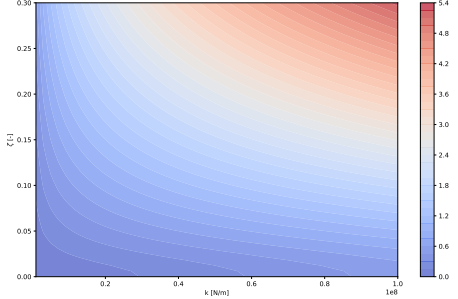


(b) Around the Resilient Mount Base Settings.

Figure D.11: Surface Plots of Displacement \tilde{U}_2 at 192 Hz for Combinations of stiffness Values and Damping Ratios Normalised to the Response with the Resilient Mount Base Settings.



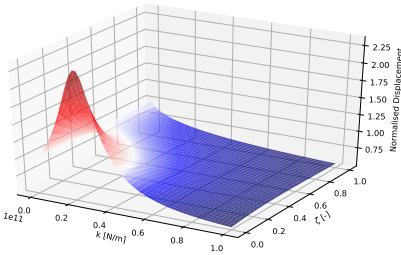
(a) In Full Range.



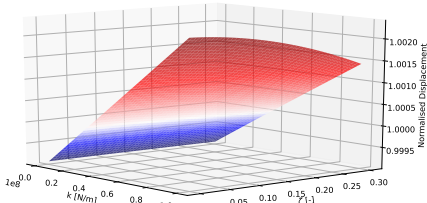
(b) Around the Resilient Mount Base Settings.

Figure D.12: Contour Plots of Displacement \tilde{U}_2 at 192 Hz for Combinations of stiffness Values and Damping Ratios Normalised to the Response with the Resilient Mount Base Settings.

D.4. Surface and Contour Plots Normalised \tilde{U}_1

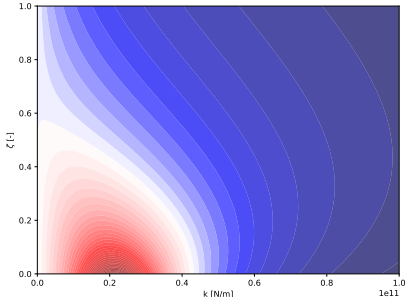


(a) In Full Range.

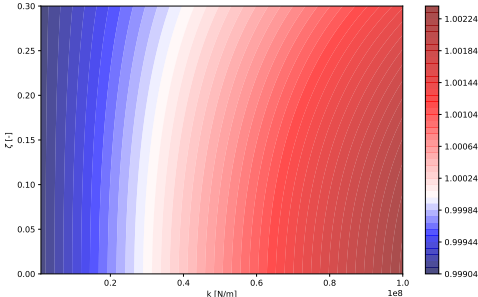


(b) Around the Resilient Mount Base Settings.

Figure D.13: Surface Plots of Displacement \tilde{U}_1 at 192 Hz for Combinations of stiffness Values and Damping Ratios Normalised to the Response with the Resilient Mount Base Settings.



(a) In Full Range.



(b) Around the Resilient Mount Base Settings.

Figure D.14: Contour Plots of Displacement \tilde{U}_1 at 192 Hz for Combinations of stiffness Values and Damping Ratios Normalised to the Response with the Resilient Mount Base Settings.

E

Transmissibility Intersection Point for a 2-DOF System

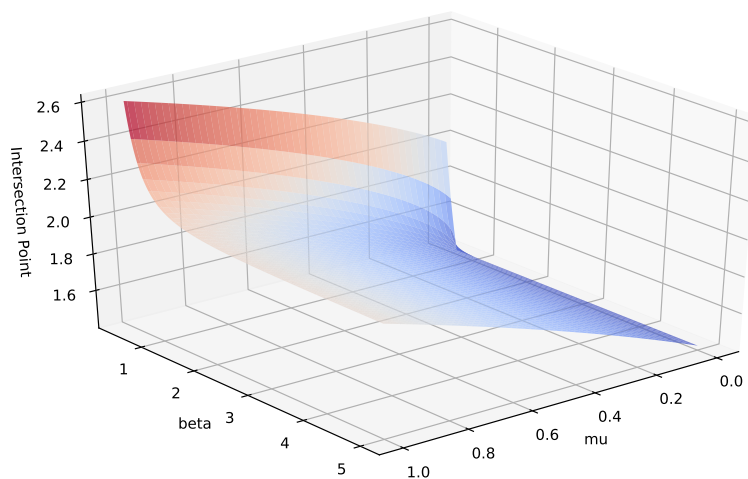


Figure E.1: Intersection Point for the Transmissibility of a 2-DOF System for Different Values of μ and β .